THE EVALUATION OF A WATERJET SYSTEM USING COMPUTATIONAL FLUID DYNAMICS VALIDATED BY WIND TUNNEL TESTS

DAVID MURRIN

NOTE TO USERS

Page(s) not included in the original manuscript and are unavailable from the author or university. The manuscript was scanned as received.

164

This reproduction is the best copy available.

UMI®

The Evaluation of a Waterjet System using Computational Fluid Dynamics Validated by Wind Tunnel Tests

by

©David Murrin, B. Eng.

A thesis submitted to the School of Graduate Studies

in partial fulfilment of the requirements for the degree of

Master of Engineering

Faculty of Engineering and Applied Science

Memorial University of Newfoundland

February 2002

St. John's, Newfoundland, Canada

Your file Votre référence
ISBN: 0-612-99099-0
Our file Notre référence
ISBN: 0-612-99099-0

Acknowledgements

I would like to thank my supervisors Dr. Neil Bose and Dr. Shin Chin for their time and valuable suggestions throughout the tenure of this degree program. I would also like to thank Memorial University of Newfoundland (MUN) for providing the experimental and numerical facilities required for this project and I am grateful for the financial support provided by the Institute for Marine Dynamics (IMD) and MUN. Furthermore, the technical assistance of Bernard Healy, Tom Pike, and Jim Gosse for the preparation of the model tests is gratefully acknowledged.

Finally I am indebted to my wife and family for their continued support, patience and understanding.

Abstract

Traditional methods of marine propulsion have been limited to screw-type propeller arrangements but in recent years efforts to improve vessel speed have led to the development of practical waterjet systems. As waterjet technology continues to grow, methods of testing and evaluating waterjet propulsion systems have emerged.

Conventional methods of testing propeller driven craft have been applied to waterjets and these have included self-propulsion tests using tow carriages or waterjet system tests in water tunnels. Implementation of these tests has been problematic due to the small size of models, the speed required during model testing of high speed craft at equivalent speed, and the difficulty in obtaining detailed flow information through the jet. This study investigates the applicability of larger scale testing of a waterjet system using a wind tunnel.

In addition to physical testing, computer simulations have emerged as a valid method for evaluating the behaviour of fluids and performance of equipment. Physical experimentation forms an integral part of any CFD simulation as the accuracy of simulation results is obtained through validation against experimental data. Once validated, however, the numerical code is capable of providing engineering quantities such as force, velocity and pressure, at a level of detail not possible through physical experimentation.

The focus of this research was to study the applicability of CFD analysis to waterjet testing and to evaluate the propulsion performance of a waterjet unit using CFD

simulation validated by experimental results. A full-scale waterjet was tested at the Memorial University of Newfoundland wind tunnel, and numerical analysis was achieved with CFX 5.6® CFD software. Once validated, the CFD simulation was used to predict the propulsion performance of the waterjet unit using the momentum flux method. This thesis presents a comparison of the CFD predictions and the wind tunnel tests.

Table of Contents

List of Figures

List of Tables

Appendices

1 Introduction

Traditional methods of marine propulsion have been limited to screw-type propeller arrangements but contemporary efforts to improve vessel speed have led to the development of practical waterjet systems. Such developments challenge the heretofore-accepted theory that waterjets are inherently less efficient than screw propellers and in recent years there has been a remarkable increase in the number of waterjet manufacturers and vehicles equipped with waterjet propulsion systems.

The history of waterjet technology dates back to the time of Archimedes, when he was credited with inventing a device used for pumping out flooded ships, the Archimedean screw (Allison, 1992). Technological limitations, coupled with a lack of understanding of the principles of propulsion before the 19th century, however, stunted waterjet development while paddle wheel and propeller technology flourished.

During the 1960's and 1970's, some high-speed hydrofoils were equipped with waterjet propulsion systems but the high cost of design, outfitting, and operation limited their applications to military endeavours. In the 1980's, however, lower fuel costs and increased highway congestion were catalysts in an effort towards viable transportation alternatives. The result was the development of waterjet technology capable of competing with traditional screw propellers. High-speed aluminium catamarans, for example, were relatively easy to design and build compared to other dynamically supported craft, and vessels propelled by waterjet systems became feasible surrogates to propeller craft, especially in the high-speed market. The pioneering work of Hamilton led to the

development of the modern waterjet unit and Figure 1-1 shows a typical aluminium catamaran using Hamilton waterjets:

Figure 1-1. Athena High-Speed Catamaran

Presently, thousands of waterjets are produced each year for the recreational market, to be used in water scooters and small fishing boats. At the commercial level high-speed passenger ferries equipped with multiple jets having installed powers of more than 70 MW are commonplace. The high-speed transportation of cargo, and containerized goods has yet to be realised, but in time it is likely that waterjet technology will dominate most high-speed marine applications.

Some advantages of waterjet propulsion are listed below:

- Elimination of appendages
- Improved manoeuvrability
- Improved braking especially at speed
- Reduced fuel consumption at high speeds

- Greatly reduced underwater noise
- Reduced draft (depending on hull type)

Waterjets and propellers propel boats differently and in the past tradition dictated the manner in which waterjet performance was evaluated. Various testing methods have been proposed to determine the performance characteristics of waterjets and the momentum flux method, recommended by the '96 ITTC has emerged as the industry standard.

Conventional methods of testing propeller driven craft were also applied to waterjets, without success, and self-propulsion tests using tow carriages have given way to large scale testing of waterjets using wind tunnels. Although Reynolds numbers are much smaller when using air as the working fluid, it has been shown that testing of waterjets using wind tunnels produces results that are applicable to real-world applications (Griffiths-Jones, 1994).

In addition to physical testing, computer simulations have emerged as a valid method for evaluating the behaviour of fluids and performance of equipment, thanks in part to advances in computing power in recent years. Numerical treatments are generally less costly than physical tests and produce practically unlimited level of detail in their results. Computational fluid dynamics (CFD) is based on the analysis of fluid systems by means of computer simulation and has been used for a wide range of industrial and non-industrial applications. Physical experimentation forms an integral part of any CFD simulation as the accuracy of simulation results is obtained through validation against experimental data. Once validated, however, the numerical code is capable of providing

engineering quantities such as force, velocity and pressure, at a level of detail not possible through physical experimentation. Used in conjunction with good experimental data, computer simulation represents an extremely powerful tool for engineering analysis.

The focus of this research was to study the applicability of CFD analysis to waterjet testing and to evaluate the propulsion performance of a waterjet unit using CFD simulation validated by experimental results. A full-scale waterjet was tested at the Memorial University of Newfoundland wind tunnel, and numerical analysis was achieved with CFX 5.1® CFD software. Once validated, the CFD simulation was used to predict the propulsion performance of the waterjet unit using the momentum flux method.

2 Literature Review

Renewed interest in waterjet propulsion over the last 20 years has led to a better understanding of the principles of waterjet propulsion, more efficient pumping units, and the evolution of the modern waterjet. These advances are the result of research into both model testing techniques and the manner in which waterjet performance is interpreted. Traditional testing methods have given way to specific tests tailored to the unique properties of waterjets and advances in numerical modelling techniques and high speed computing have made computer simulation more feasible. As the numerical modelling of waterjet systems continues to evolve, model testing plays an important role in their validation. The following chapter summarises the published research on experimental and numerical treatments of waterjet propulsion. More specifically, it highlights important work related to the testing of waterjets in wind tunnels, and their subsequent computer simulation and validation.

Griffith-Jones and Bowen (1992) discussed modelling of the flow through the intake of a waterjet propulsion unit and a planing hull. Using a wind tunnel, they observed flow separation from the intake roof of the waterjet unit. Acknowledging that the turbulence levels in the flow would be reduced, the impeller shaft was removed from the intake so that numerical simulation would be simpler. The sidewall of the wind tunnel was angled inwards to simulate the angle of incidence of a typical planning hull. Their results showed that there was a significant power loss due to non-uniformity and flow separation.

Widmark and Gustafsson (1997) performed 3-dimensional computational fluid dynamics (CFD) calculations on a complete waterjet unit with two different codes, SHIPFLOW and FIDAP. The pressure and velocity distribution throughout the waterjet unit was studied in order to determine the losses at the inlet and outlet. The rotational velocity component normally associated with rotor shafts was omitted in the simulation because the waterjet that was modelled was equipped with a shaft protection hub. Furthermore, guide vanes were not modelled at the outlet since a uniform volume force was used to model the impeller and did not account for the swirling of the rotor. Results indicated that a capture width 70% larger than the inlet width should replace the 30% recommendation of Kruppa et al. (1996) for momentum flux calculations.

Turnock and Hughes (1997) undertook the evaluation of a CFD code for investigating hull-waterjet flow interaction. A physical model was built from faired strips of plywood attached to a base plate by a series of ribs to define the outline shape. The front face was transparent to allow flow visualisation with wool tufts and pressure distribution was monitored by a number of static pressure taps along one half of the jet unit, at a number of radial and longitudinal sections. The model was attached to the side of the wind tunnel to simulate the flow to the waterjet unit. They determined mass flow through the duct exit as the product of the speed at the midpoint and the cross-sectional area, and the flow through the exit plane of the working section was obtained by mass continuity. For simplicity, a constant mass flow rate though the duct exit was defined for all the CFD models. It was acknowledged, however, that waterjet-impellers operating at constant speeds do not necessarily experience constant mass flow rate through the duct. The

simulation converged with residuals of $1x10^{-3}$ after 700 cycles and it was determined that a flat plate does not accurately model the pressure changes that occur as water enters the inlet. If a waterjet duct is to be designed for a specific application, they concluded, the influence of the surrounding hull must also be considered in addition to the flow through the duct. An important conclusion was that CFD work could be extremely beneficial at the design stage. The results of a CFD simulation can provide engineers with velocity profiles, pressure distributions and subsequent viscous force distributions in order to better understand the resistance and propulsion aspects of waterjets.

Verbeek and Bulten (1998) used the results of wind tunnel experiments to validate CFD results. It is well known that a curved pipe with uniform flow leads to non-uniform flow due to secondary effects, and that the velocity increase is caused by centrifugal forces that lead to a maximum velocity at the top of pipe duct. The opposite, they concluded, happens in waterjets due the boundary layer under the hull. The uniform velocity in the boundary layer results in the entrainment of high-speed water at the bottom of the duct, and low speed water at the top. Results showed that 7-9% of the total installed power was lost at the inlet due to this non-uniformity, and that more uniform velocity profiles result from increased turbulence in the flow.

Allison et al. (1998) investigated the parallel development of computational fluid dynamics (CFD) with the Reynolds Averaged Navier Stokes (RANS) equations. Results indicated that the blade forces and pressures yielded by numerical software compared well with those found from conventional methods. Simulation results, they concluded, can be used to: identify potential problem areas such as re-circulation and flow

distortions, provide fluid loading on solid parts, predict overall performance of devices, and corroborate the results obtained from other design methods.

Roberts and Walker (1998) studied the ingestion effects of a waterjet inlet and stated that current design practises could lead to the under prediction of thrust for flush waterjet intakes. The experiments were based on a 1:7.67 scale waterjet mounted to a closed circuit wind tunnel and equipped with a secondary fan exhausting to the atmosphere. The drive shaft was not modelled, but the shaft and fairing were expected to increase the outlet distortion and flow losses in a real intake. It was concluded that wind tunnel tests provide a convenient and economical means of obtaining the detailed flow measurements needed to understand the physics of intake flows and validate computational prediction methods. A major limitation of the test, however, was the inability of air measurements to provide information pertaining to cavitation.

Mununga, Huntsman, and Hothersall (1998) reported on the testing of a waterjet unit using a wind tunnel to investigate the effects of a splitter plate and screen grid. The non-uniform loading due to flow separation was investigated and revealed unbalanced loading on the impeller. They undertook the design of a splitter plate and screen grid to improve the quality of flow through the intake, and hence improve the performance of the waterjet unit. Results showed a dramatic improvement in flow uniformity using the splitter plate, and marginal improvement using intake screens

Many of the papers of the third RINA Waterjet Conference in 2001 investigated hull-propulsor interaction using RANS codes. Allison et al (2001) used the UNCLE code to understand the flow behaviour around a ship with and without waterjets. Results indicate

that, for waterjets, a large portion of the upstream flow is drawn into the inlet. The behaviour is much different from that observed with the bare hull, where streamline passed downstream rather benignly.

Seil (2001) validated simulation results with experimental data for the velocity distribution at the duct exit and found them to be in good qualitative and quantitative agreement. Using FLUENT® code with the k-e turbulence model, the effect of the shaft, shaft rotation and scale effect (Reynolds number) on the waterjet inlet flow was investigated. It was determined that shaft rotation had a significant effect on distorting the wake at the duct exit.

Hu and Zangeneh (2001) used different commercial CFD codes such as FLUENT, UNS, RAMPANT, and TASCflow to calculate waterjet impeller torque. The predicted torque values were compared with measurements and the prediction accuracy was seen to be very good. They concluded that the shaft greatly influences the flow field in the waterjet and should not be neglected in CFD calculations of the intake duct

3 Similitude Analysis

3.1 Similarity

When using physical models, care must be taken to ensure that results are transferred from model scale to full scale correctly. It is often the case that complete similarity between the two scales is not physically possible, and a system of laws that maintain similarity between the most significant elements of model scale and full scale is required. The following conditions must be satisfied in order for specific forces on the model and full-scale object to be similar:

- Geometric similarity
- Kinematic similarity
- Dynamic similarity

3.1.1 Geometric Similarity

Geometric similarity refers to maintaining correct length scale ratios between prototype and model. This is generally straightforward in terms of physical dimensions such as the length to breadth ratio, but can present some interesting challenges when dealing with difficult factors such as surface roughness. In ship model testing, for example, even if the model surface is an exact copy of the prototype surface, flow along the surface will not be similar due to the flow characteristics of water over large and small scales. In the case of a large-scale factor, model dimensions may be extremely small, and structural

limitations can make it difficult to maintain geometric similarity. Such is the case when working with model propellers, as the trailing edges of the blades have to be made relatively thicker than their full-scale counterparts, for practical reasons (Harvald, 1983).

Geometric similarity, then, cannot always be maintained between individual components of the model and prototype, and care must be taken to ensure that correction factors are in place, or the effect is minimal.

3.1.2 Kinematic Similarity

In order to maintain kinematic similarity, the ratios between velocities in the model must be equal to the ratios between corresponding velocities in the prototype, at corresponding positions. This will be discussed in more detail in Section 3.3, as it is relevant to the waterjet system, in particular.

3.1.3 Dynamic Similarity

Dynamic similarity requires that force-scale ratios are the same for model and prototype. In order to achieve this, force polygons (vectors) must be similar (i.e. the direction of the forces, and the ratio of the force scales must be the same). Achieving complete dynamic similarity is not always possible, and the experimenter is charged with the responsibility of selecting the forces that dominate, and those that are relevant to both the model and prototype. Further details are supplied in the section on waterjet dimensional analysis.

3.2 Indicial Approach & Matrix Methods

3.2.1 The Indicial Approach

Rayleigh's indicial method consists of determining the variables relevant to a system and writing them in terms of 'fundamental dimensions'. The choice of fundamental dimensions can be somewhat arbitrary, but it has been generally accepted that mass, length, and time, are suitable units for describing the behaviour of engineering systems. These dimensions are familiar to most people, and because they have physical relevance, it is easy to visualise one object being longer than another, for example. The functional relationship can then be written in terms of the mass [M], length [L], and time [T] dimensions, and the exponents of each dimension equated to ensure dimensional homogeneity (Sharp, 1983).

Solving for the constants in the exponent of each variable leads to a series of dimensionless groups, or π terms. The π terms form the basis of similitude theory, since two geometrically similar systems will be both kinematically and dynamically similar if π terms in one system are equal to those of the other. Buckingham developed a method of identifying the number of relevant π terms based on the number of variables and dimensions. His method states:

If an equation involving k variables is dimensionally homogenous, it can be reduced to a relationship among k-r independent dimensionless products, where r is the minimum number of reference dimensions required to describe the variables (Munson et al. 1998).

Determining a set of π terms is accomplished by first selecting from the original set of variables, a set of repeating variables equal to the number of reference dimensions. The repeating variables can then be combined with the remaining variables to form the necessary π terms. For a given system, of paramount importance is the way in which one variable behaves as a result of changes to the others. These variables are termed dependent variables, and it behoves one to limit their appearance to a single π term. It is important, then, to exclude the dependent variables from the list of repeating variables. A π term is formed by multiplying a non-repeating variable with the product of the repeating variables, each raised to an exponent that will make the combination dimensionless. Repeating the procedure for the remaining non-repeating variables forms subsequent π terms. Some common engineering units expressed in terms of the M, L, T system are shown in Table 3-1.

Table 3-1. Dimensions associated with engineering physical quantities

Physical Quantity	Symbol	Dimensions for MLT system
Mass	M	$[M]$
Length	L	$[L]$
Time	T	$[T]$
RPM	N	$[T]^{-1}$
Area	A	$[L]^{2}$
Mass Density	ρ	$[M][L]^{-3}$
Force	F	$[M][L][T]^{-2}$
Torque	Q	$[M][L]^{2}[T]^{-2}$
Dynamic Viscosity	μ	$[M][L]^{-1}[T]^{-1}$

3.2.2 Matrix Methods

The indicial equation inherent to the Rayleigh method can be solved using elementary matrix algebra. The equation may be written as a dimensional matrix with the influencing variables occupying columns of a matrix, and rows signifying the M, L, T system. The values at corresponding locations in the matrix are simply the exponent of the M, L, or T dimension, for the variable in question. The solution of a system of linear equations is possible by reducing the first three columns to the unit matrix and obtaining the rank of the matrix. The rank of the matrix specifies the number of independent equations that are necessary to describe the exponents of the variables in the system. Buckingham theory is then satisfied when the first three columns have been reduced to the unit matrix, since the total number of dimensionless quantities required is equal to the number of variables minus the rank of the dimensional matrix (Sharp, 1983).

Use of Echelon

Echelon in a matrix exists when the number of zero values in rows reading from left to right increases from top to bottom. Matrices exhibiting this characteristic can be manipulated by row and column operations, and the variables can be related to one another with great freedom. A set of repeating variables equal to the number of fundamental dimensions can be forced to the unit matrix, and the remaining dimensions can then be written in terms of the others. If the variables are written in the M, L, T system, for example, the unit matrix will be a three by three matrix made up of 3 repeating variables and the remaining columns provide the indices of the π terms.

The situation may arise, however, where it is not possible to write the repeating variables of choice in echelon form and one must rely on linear algebra. It has been shown that any matrix can partitioned into:

1) A unit matrix consisting of a set of repeating variables

2) A matrix made up of the remaining variables

Repeating the operation that transformed the repeating variables into the unit matrix forms the second matrix. Consider, for example, an eight by three matrix that has been partitioned into a three by three matrix (A), and a five by three matrix (B). In order to form the unit matrix, matrix A must be multiplied by it's inverse ($I = A^{-1}$), so $A = A^* I$. Matrix B, then must undergo the same operation ($D = I * B$), and the final matrix can be written as the combination of matrix A and D.

The matrix method is a very quick and powerful tool for manipulating the variables of interest into dimensionless form. When faced with a large number of independent variables, the matrix method can be used with simple computer programs to provide a very fast solution for the non-dimension relationship between variables. The simplicity of the approach also allows one to repeat the operations with different sets of repeating variables until the desired set of π terms is obtained. As with other methods, the final set of π terms can be the result of compounding the results of the matrix analysis in order to provide convenient solutions. The application of this method with respect to the analysis of waterjets is described in the next section.

3.3 Waterjet Dimensional Analysis

The variables necessary to describe the waterjet system are given in Table 3-2:

Table 3-2. Waterjet system variables

Parameter	Symbol	Fundamental Units
Shaft speed	N	$[T]^{-1}$
Characteristic length	L	[L]
Fluid density	ρ	$[M][L]^{-3}$
Velocity	V	$[L][T]^{-1}$
Dynamic viscosity	μ	$[M][L]^{-1}[T]^{-1}$
Gravitational acceleration	g	$[L][T]^{-2}$
Pressure	p	$[M][L]^{-1}[T]^{-2}$
Surface tension	φ	$[M][T]^{-2}$
Dependent Variables		
Thrust	T	$[M][L][T]^{-2}$
Power	P	$[M][L]^{2}[T]^{-3}$
Shaft torque	Q_s	$[M][L]^{2}[T]^{-2}$
Volumetric flow rate	Q	$[L]^{3}[T]^{-1}$

Thrust, torque, power, and volumetric flow rate are dependent variables and the behaviour of the waterjet system can be described by:

$$T \text{ or } Q_s \text{ or } P \text{ or } Q = \phi(N,L,\rho,V,\mu,g,p,\varphi) \qquad [3.1]$$

In order to begin the dimensional analysis, a matrix is made from the indices of these variables.

$$\begin{array}{c} \\ M \\ L \\ T \end{array} \begin{array}{c} \begin{array}{cccccccccccc} N & L & \rho & T & V & \mu & g & p & \varphi & P & Qs & Q \end{array} \\ \begin{bmatrix} 0 & 0 & 1 & 1 & 0 & 1 & 0 & 1 & 1 & 1 & 1 & 0 \\ 0 & 1 & -3 & 1 & 1 & -1 & 1 & -1 & 0 & 2 & 2 & 3 \\ -1 & 0 & 0 & -2 & -1 & -1 & -2 & -2 & -2 & -3 & -2 & -1 \end{bmatrix} \end{array}$$

The first three variables are chosen as repeating variables, and the sub-matrices are given by:

$$A := \begin{bmatrix} 0 & 0 & 1 \\ 0 & 1 & -3 \\ -1 & 0 & 0 \end{bmatrix}$$

and

$$B := \begin{bmatrix} 1 & 0 & 1 & 0 & 1 & 1 & 1 & 1 & 0 \\ 1 & 1 & -1 & 1 & -1 & 0 & 2 & 2 & 3 \\ -2 & -1 & -1 & -2 & -2 & -2 & -3 & -2 & -1 \end{bmatrix}$$

The inverse of the first matrix becomes:

$$A1 := \begin{bmatrix} 0 & 0 & -1 \\ 3 & 1 & 0 \\ 1 & 0 & 0 \end{bmatrix}$$

and both matrix A and matrix B are multiplied by the inverse of matrix A. Matrix A multiplied by it's inverse gives the identity matrix (A3):

$$A3 := \begin{bmatrix} 1 & 0 & 0 \\ 0 & 1 & 0 \\ 0 & 0 & 1 \end{bmatrix}$$

and the resultant for $A^{-1} * B$ is given by D1:

$$D1 := \begin{bmatrix} 2 & 1 & 1 & 2 & 2 & 2 & 3 & 2 & 1 \\ 4 & 1 & 2 & 1 & 2 & 3 & 5 & 5 & 3 \\ 1 & 0 & 1 & 0 & 1 & 1 & 1 & 1 & 0 \end{bmatrix}$$

Finally, the matrices can be augmented to form a single matrix:

$$\begin{array}{c} \\ N \\ L \\ \rho \end{array} \begin{array}{c} \begin{array}{ccccccccccc} N & L & \rho & T & V & \mu & g & p & \varphi & P & Qs & Q \end{array} \\ \begin{bmatrix} 1 & 0 & 0 & 2 & 1 & 1 & 2 & 2 & 2 & 3 & 2 & 1 \\ 0 & 1 & 0 & 4 & 1 & 2 & 1 & 2 & 3 & 5 & 5 & 3 \\ 0 & 0 & 1 & 1 & 0 & 1 & 0 & 1 & 1 & 1 & 1 & 0 \end{bmatrix} \end{array}$$

It is then clear that Buckingham's theory has been respected, and nine non-dimensional terms can now be determined from the resulting matrix. The system, then can be written as follows:

$$\phi = \left(\frac{T}{N^2 L^4 \rho}, \frac{V}{NL}, \frac{\mu}{NL^2 \rho}, \frac{g}{N^2 L}, \frac{p}{N^2 L^2 \rho}, \frac{\varphi}{N^2 L^2 \rho}, \frac{P}{N^3 L^5 \rho}, \frac{Q_s}{N^2 L^5 \rho}, \frac{Q}{NL^3} \right) = 0 \qquad [3.2]$$

The first term can be re-written such that the geometric parameter (L^4) is replaced by impeller diameter (D), and the resulting term is recognised as the thrust coefficient (K_T).

$$K_T = \left(\frac{T}{\rho N^2 D^4} \right) \qquad [3.3]$$

The second term can also be slightly modified to resemble traditional non-dimensional terms. Replacing the 'V' term with the advance velocity (V_A), and the geometric

parameter with the impeller diameter (D), the term is recognised as the advance coefficient (J).

$$J = \left(\frac{V_A}{ND}\right) \qquad [3.4]$$

Recognising that

$$[N] = \frac{[V]}{[L]} \qquad [3.5]$$

and that the dynamic viscosity (μ) is related to the kinematic viscosity (ν) according to:

$$\nu = \frac{\mu}{\rho} \qquad [3.6]$$

we can substitute for 'N' and 'μ' in the third term and arrive at the reciprocal of the Reynolds number:

$$\mathrm{Re}^{-1} = \frac{\mu}{\rho N L^2} = \frac{\nu}{\left(\frac{V}{L}\right)L^2} = \left(\frac{\nu}{VL}\right) \qquad [3.7]$$

Similarly, we can substitute for 'N' in the fourth term, invert and arrive at the reciprocal of the Froude number:

$$Fr^{-1} = \left(\frac{g}{N^2 L}\right) = \left(\frac{g}{\left(\frac{V}{L}\right)^2 L}\right) = \left(\frac{gL}{V^2}\right) = \left(\frac{V}{\sqrt{gL}}\right)^{-1} \quad [3.8]$$

Replacing the pressure term 'p' with the change in pressure 'Δp', the fifth term can be written as the cavitation number(σ):

$$\sigma = \left(\frac{\Delta p}{\rho N^2 L^2}\right) \quad [3.9]$$

Substituting for 'N' in the fifth term results in the Weber number (We)

$$We = \frac{\varphi}{\rho L^3 N^2} = \frac{\varphi}{\rho L^3 \left(\frac{V}{L}\right)^2} = \left(\frac{\varphi}{\rho V^2 L}\right) \quad [3.10]$$

The remaining three terms are recognised as the power coefficient (K_p), shaft torque coefficient (K_{Qs}), and the volume flow rate coefficient (K_Q).

$$K_P = \frac{P}{\rho N^3 D^5} \quad [3.11]$$

$$K_{Qs} = \frac{Q_S}{\rho N^2 D^5} \quad [3.12]$$

$$K_Q = \frac{Q}{ND^3} \quad [3.13]$$

3.4 Discussion of Non-Dimensional Terms

It is not often physically possible, or necessary, to satisfy all of the π terms in any particular system. In such cases, the most important terms are respected and other, less significant, terms can be neglected, provided certain assumptions can be made. The following is a discussion of the relevant non-dimensional terms for testing a waterjet system in a wind tunnel at full scale.

3.4.1 Advance Coefficient

Kinematic similarity is accomplished when the velocities at corresponding points of the model and prototype have the same direction, and hence the angle of attack of the impeller is similar between model and full scale. For this reason, the ratio of the speed with which the fluid flows into the impeller (i.e. the speed of advance), and the velocity of the impeller (circumferential velocity) must be the same for both the model and the prototype. The advance coefficient can be thought of as the ratio of the axial velocity of flow into the impeller, to the tangential velocity of flow relative to the impeller. Kinematic similarity, then, can be accomplished if the advance coefficient for the model and prototype are the same.

3.4.2 Reynolds Number

Flow regimes can generally be classified as either laminar, turbulent, or transitional. The significance of the Reynolds number is that it is very useful in determining flow regimes for specific fluids, at a given velocity. It can be thought of as the ratio of inertial forces to viscous forces, and is important in most problems involving fluid dynamics. Inspection of

the variables composing the Reynolds number shows that, in many cases, matching the Reynolds numbers in model and prototype is not possible. In such cases it is important to ensure that the flow regimes are similar. The high-speed flows that characterise waterjets exist in the turbulent regime and it is important to ensure that flow regimes in model waterjet systems also behave in a turbulent manner. According to Munson et al. (1998), scale error is negligible provided the Reynolds numbers for the flow in the model and prototype are greater than 5×10^5.

For the model waterjet system, flat plate boundary layer theory was applied at the wall of the wind tunnel. The inlet was located approximately 9.5 metres from the leading edge of the wind tunnel. Assuming that the distance from the forward perpendicular to the inlet of the prototype waterjet is at least 9.5 metres, the velocity in the wind tunnel is a limiting case. The kinematic viscosities of air and water are $1.46e^{-5}$ m^2/s, and $1.17e^{-6}$ m^2/s, respectively and it follows that any speed greater than 0.77 m/s provides sufficiently turbulent flow.

$$V \geq \left(\frac{\mathrm{Re} \cdot \nu_{air}}{L} \right) = \left(\frac{5e^5 \cdot 1.46x10^{-5} m^2/s}{9.5m} \right) = 0.77 m/s \qquad [3.14]$$

$$V \geq \left(\frac{\mathrm{Re} \cdot \nu_{w}}{L} \right) = \left(\frac{5e^5 \cdot 1.17x10^{-6} m^2/s}{9.5m} \right) = 0.062 m/s \qquad [3.15]$$

From this it may be concluded that the flow regime in the boundary layer of the tunnel wall is likely to be turbulent for both the model and prototype, provided the velocity is greater than 0.77 m/s. In addition to this, the velocity profile in the tubular section of the

waterjet may be examined by computing the Reynolds number for viscous flow in a pipe. It is important to ensure that the velocity profiles are similar because it is then possible to conclude that the boundary layers in the model and prototype will be similar. Using the sectional diameter (D = 0.35 m) as the reference dimension:

$$\mathrm{Re}_m = \left(\frac{VD}{\nu_{air}}\right) = \left(\frac{7.68e^{-1}m/s \cdot 0.35m}{1.46e^{-5}m^2/s}\right) = 1.85e^4 \qquad [3.16]$$

$$\mathrm{Re}_p = \left(\frac{VD}{\nu_w}\right) = \left(\frac{7.68e^{-1}m/s \cdot 0.35m}{1.17e^{-6}m^2/s}\right) = 2.30e^5 \qquad [3.17]$$

According to Munson et al. (1998), the flow in a pipe is turbulent provided that the Reynolds number for the flow is greater than 4000. It is therefore likely that the flow regime, and velocity profile for the model and prototype will be approximately similar for the assumed, minimum, velocity. The speed in the tubular section of the model waterjet was expected to be much larger than 0.77 m/s, and turbulence in both model and prototype was ensured.

3.4.3 Froude Number

Waterjet systems perform work on water by lifting it through an elevation and expelling it above the water surface. The Froude number can be thought of as the ratio of inertial forces to gravitational forces, and although it is important for testing of waterjets in wave tanks, or water tunnels, it has no real significance when testing in air. This is due to the fact that the model waterjet is not expelling the flow from one fluid into another. In

addition to this, the waterjet was attached to the wind tunnel at a ninety-degree angle, such that the hull was effectively on its side. There is no lifting component in the model. Froude scaling, therefore, was neglected.

3.4.4 Cavitation number

Cavitation is the process of formation of the vapour phase of a liquid when it is subject to reduced pressure at constant ambient temperature (Harvald, 1983). The occurrence of cavitation can be detrimental to the effectiveness of a propeller, as well as physically destructive. Upon formation, cavitation bubbles can erode propeller blades, parts of the jet ducts and stators, and cause a breakdown in flow and subsequent loss of thrust. The situation, therefore, should be avoided at all costs. Waterjets, fortunately, are less susceptible to the phenomena since the intake slows the water before delivering it to the impeller, and decreases the chances of cavitation (Allison, 1992). Furthermore, the "Final Report and Recommendations the 23 ITTC" submitted by the specialist committee on validation of waterjet test procedures (ITTC, 2002) assumes that any cavitation in the pump or intake during operation does not affect the powering characteristics of waterjets. The experimental set-up in the wind tunnel was not designed to measure cavitation, but pressure taps can be placed near the impeller to determine pressure variations at high speeds. Should detailed tests regarding the likelihood of cavitation be necessary, a cavitation tunnel should be used. In any event, the system was not set up to monitor, or consider the effects of cavitation, and the coefficient was therefore ignored.

3.4.5 Weber number

The Weber number is the ratio of the inertia force to the surface tension force. It is often important when considering the surface stresses from cavitation bubbles. Surface tension, however, is not a property of gases and has no significance when performing experiments in air. Similarity of the Weber number is neglected for the purpose of this analysis.

3.4.6 Mach Number

When dealing with air at high speeds, the assumption of incompressibility is not always appropriate. According to Munson et al. (1998), a fluid can be assumed to be incompressible if the Mach number is less than 0.3. The Mach number is the ratio of the inertia force to the compressibility force and is expressed as the ratio of the velocity of interest (V_i) with respect to the velocity of sound in air (c):

$$Ma = \frac{V_i}{c} \qquad [3.18]$$

The velocity of interest is made up of the impeller speed, and the axial velocity (V_a):

$$V_t = \omega r = \frac{2\pi N}{60} \qquad [3.19]$$

$$V_i = \left(V_t^2 + V_a^2\right)^{\frac{1}{2}} \qquad [3.20]$$

It follows that for any velocity less than 99 m/s, the assumption of incompressibility is valid. The maximum speed of the wind tunnel is 15 m/s and in order to approach the

bounds of incompressibility, a shaft speed greater than 5000 RPM would be necessary. This is well beyond the operating speed of most waterjet systems. Since the Mach number is invariably less than 0.3, we may conclude that the fluid is effectively incompressible, as is normally the case in low speed wind tunnels.

3.4.7 Power, Shaft Torque, Thrust, and Volume Flowrate Coefficients

In order to maintain dynamic similitude, the direction of the forces and the ratio of the force scales must be the same. The remaining coefficients, then, are extremely important in order for us to assess the performance of the propeller. With similitude assumed, it is possible to determine the power, shaft torque, thrust, and volume flowrate of the model and prototype. To summarise, the non-dimensional coefficients of importance are:

$$\text{Advance Coefficient: } J = \left(\frac{V_A}{ND} \right)$$

$$\text{Thrust Coefficient: } K_T = \left(\frac{T}{\rho N^2 D^4} \right)$$

$$\text{Shaft Torque Coefficient: } K_{Qs} = \frac{Q_S}{\rho N^2 D^5}$$

$$\text{Volume Flow Rate Coefficient: } K_Q = \frac{Q}{ND^3}$$

3.5 Scaling Laws

Scaling laws permit the magnitude of a variable in one scale to be calculated from its value in a different scale. The non-dimensional terms presented earlier provide a means of determining the full-scale values of several important variables for the waterjet system.

The ratio of a model variable to it's corresponding prototype variable is known as the scale for that variable. The length scale is defined as the ratio of a linear dimension in a prototype, to the corresponding dimension for the model, and is denoted by λ:

$$\lambda = \frac{L_p}{L_m} \qquad [3.21]$$

where the subscripts p and m represent the model and prototype, respectively.

Equating the advance coefficients for the model and prototype satisfies the condition of kinematic similitude:

$$J_m = \left(\frac{V_{Am}}{N_m D_m}\right) = \left(\frac{V_{Ap}}{N_p D_p}\right) = J_p \qquad [3.22]$$

Scaling the shaft speed, or advance velocity, is then accomplished through the following relationship:

$$\frac{V_p}{V_m} = \left(\frac{N_p}{N_m}\right)\left(\frac{D_p}{D_m}\right) = \left(\frac{N_p}{N_m}\right)(\lambda) \qquad [3.23]$$

For Power we have:

$$K_{pm} = \frac{P_m}{\rho_m N_m{}^3 D_m{}^5} = \frac{P_p}{\rho_p N_p{}^3 D_p{}^5} = K_{pp} \quad [3.24]$$

$$\frac{P_p}{P_m} = \left(\frac{\rho_p}{\rho_m}\right)\left(\frac{N_p}{N_m}\right)^3 (\lambda)^5 \quad [3.25]$$

where $\left(\frac{\rho_p}{\rho_m}\right) = \left(\frac{\rho_{water}}{\rho_{air}}\right) \approx 866$

Similarly for thrust:

$$K_{Tm} = \left(\frac{T_m}{\rho_m N_m D_m^4}\right) = \left(\frac{T_p}{\rho_p N_p D_p^4}\right) = K_{Tp} \quad [3.26]$$

$$\frac{T_p}{T_m} = \left(\frac{\rho_p}{\rho_m}\right)\left(\frac{N_p}{N_m}\right)(\lambda)^4 \quad [3.27]$$

Shaft torque is scaled according to:

$$K_{Qsm} = \frac{Q_{Sm}}{\rho_m N_m^2 D_m^5} = \frac{Q_{Sp}}{\rho_p N_p^2 D_p^5} = K_{Qsp} \quad [3.28]$$

$$\frac{Q_{Sp}}{Q_{Sm}} = \left(\frac{\rho_p}{\rho_m}\right)\left(\frac{N_p}{N_m}\right)^2 (\lambda)^5 \quad [3.29]$$

Finally, volumetric flowrate can be scaled according to:

$$K_{Qm} = \frac{Q_m}{N_m D_m{}^3} = \frac{Q_p}{N_p D_p{}^3} = K_{Qp} \quad [3.30]$$

$$\frac{Q_p}{Q_m} = \left(\frac{N_p}{N_m}\right)(\lambda)^3 \qquad [3.31]$$

In this study, the model was full scale and hence the scale factor (λ) is equal to unity. For a given advance velocity, then, the shaft speeds for the model and prototype were equal, since the impeller diameters were the same. The power, thrust, and shaft torque then scaled according to the ratio of the density of water to the density of air.

3.6 Summary

The testing of waterjets using a wind tunnel is a simple, and effective alternative to traditional testing methods at small scales. A serious limitation, however, is the inability of air measurements to provide information pertaining to cavitation.

The dimensional analysis, summarised in Table 3-3 revealed that if the advance coefficient for the model and prototype are equal and the scale factor is unity, then the velocity of air through the wind tunnel is equal to the speed of the full scale prototype travelling in water, at a given shaft speed. Based on this information, the thrust, shaft torque, and power are all scaled by the ratio of the density of air and the density of water.

Table 3-3. Dimensional analysis of waterjet system

Parameter	Ratio	Scale
Length	L_p/L_m	(λ)
Shaft speed	V_p/V_m	$(N_p/N_m)(\lambda)$
Power	P_p/P_m	$(\rho_p/\rho_m)(N_p/N_m)^3(\lambda)^5$
Thrust	T_p/T_m	$(\rho_p/\rho_m)(N_p/N_m)(\lambda)^5$
Shaft torque	Q_{sp}/Q_{sm}	$(\rho_p/\rho_m)(N_p/N_m)^2(\lambda)^5$
Volumetric flow rate	Q_p/Q_m	$(N_p/N_m)(\lambda)^3$

When a large number of variables must be considered, matrix methods are useful for determining the non-dimensional terms required to sufficiently describe the behaviour of the system. In order to determine the importance of each, the terms were manipulated as required and transformed into physically meaningful non-dimensional terms. A complete analysis of each term and its relevance on the system was undertaken such that similitude was satisfied for the most important aspects of the experimental endeavour.

4 The Momentum Flux Method

4.1 Introduction to the Momentum Flux Method

As waterjet technology continues to grow, methods of testing and evaluating waterjet propulsion systems have emerged. In the past, these efforts had been based on traditional methods for evaluating screw propellers, but recent work has shown that the unique characteristics of waterjet systems require unique testing methods. The waterjet is an integral part of a vessel's hull and as such, traditional concepts such as thrust deduction do not apply to waterjets in the same physical way as they do for conventional screw propellers (Dyne and Lindell, 1994). Moreover, the evaluation of some basic physical quantities such as thrust, for example, requires an indirect method of measurement based on flow rates. In response to this issue, the momentum flux method was developed, and is the focus of this chapter.

Elementary momentum theory can provide valuable insight concerning marine waterjet propulsion and the momentum-flux method can be used to evaluate the power, thrust, and efficiency characteristics of the waterjet. This method, described in the 21st International Towing Tank Conference (ITTC '96), is the result of an initiative brought forth by the ITTC Specialist Committee on Waterjets asking for comments on possible power prediction methods for waterjets. This method specifies that thrust be computed from the change in momentum flux throughout the waterjet system. The vessel is considered to be stationary in a moving flow, and all flow velocity measurements used in momentum and energy calculations are made relative to the vessel (Kruppa et al., 1996).

Momentum flux can be defined as a measure of the momentum in fluid passing through a unit area of a surface in a given unit of time. Similarly, the energy flux is a measure of the amount of energy in a quantity of fluid crossing a unit area of a surface in a given unit of time. The locations of momentum and energy flux measurements for a typical waterjet are shown in Figure 4-1, below.

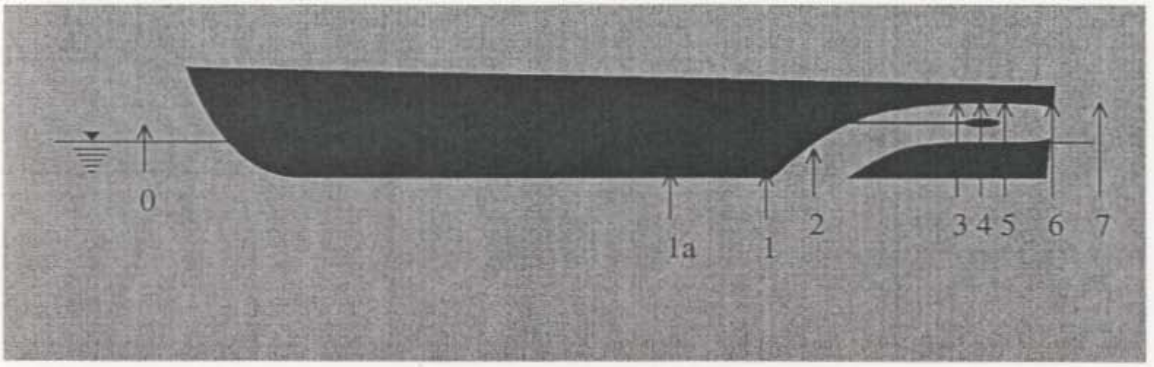

Station number	Location
0	Free Stream
1a	Inlet Velocity Profile
1	Inlet Point Of Tangency
2	Inlet Throat
3	Pump Face
4	Internal Pump Point
5	Pump Exit
6	Nozzle
7	Vena Contracta

Figure 4-1. Momentum Flux Method Station Definitions

4.2 Station 1

The fluid momentum at the intake is measured at Station 1 to account for the fluid forced through the jet units due to the forward motion of the vessel, without power. The velocity distribution of the flow is necessary for calculating the intake momentum flux.

Momentum and energy fluxes are determined by integration over a properly defined capture area with a measured or calculated velocity profile. With the velocity profile and flow rate known, the geometry of the capture area must be determined. The location of the inlet survey plane (Station 1) and the resulting effect of the proximity of the inlet on velocity measurements is a concern and a potential source of error in the momentum flux method. In addition to this, the shape and size of the capture area must be investigated.

In an effort to standardise testing practises and reduce potential bias error, the location of reference stations has undergone considerable refinement. A major result of this effort has been the development of Station 1a, located one inlet width forward of Station 1 (ITTC, 2002). The width of the inlet is defined as the maximum width between port and starboard transverse points of tangency and Station 1a is therefore substituted in place of Station 1 for all momentum flux calculations.

In theory, in order to determine the shape of the capture area, the location of streamlines entering the waterjet must be known. This is difficult in practice, since the streamlines separate near the intake, as shown in Figure 4-2. While some streamlines continue along

the hull, others enter the waterjet unit, resulting in a somewhat complicated capture area, or volume.

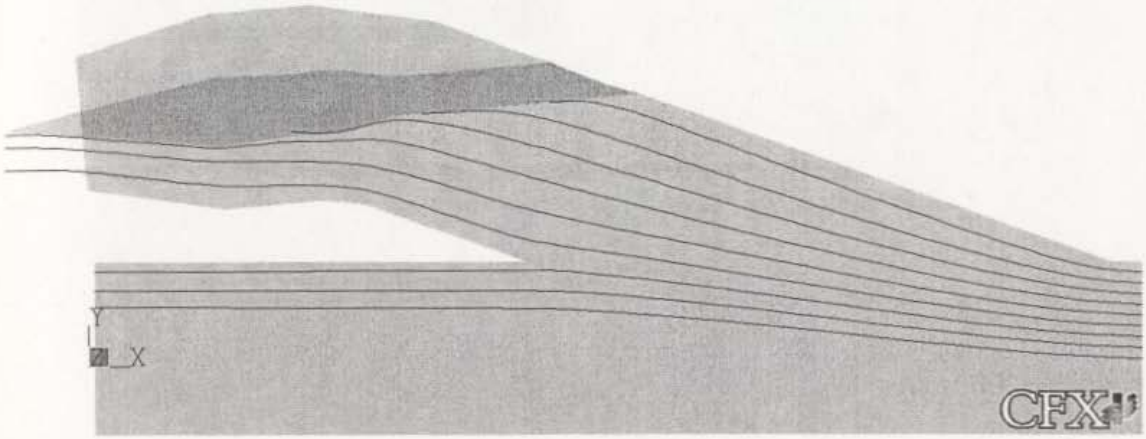

Figure 4-2. Waterjet Streamlines

Various studies have been undertaken to determine the influence of the shape of the capture area on power prediction and it has been concluded by the 21st ITTC Waterjet Committee (Kruppa et al., 1996) that both power and thrust estimates are insensitive to capture area and shape.

The recommendation of the 21st ITTC Waterjet Committee is to use a rectangular capture area with a width b_1, 30% wider than the inlet width The inlet height is then obtained by computing the height required to obtain the given flowrate, by continuity. Figure 4-3 and Figure 4-4, show the capture area at station 1a for a typical waterjet unit. The area begins at the hull surface, and as a result contains both a portion of the free stream, and the vertical height distribution associated with the boundary layer near the hull.

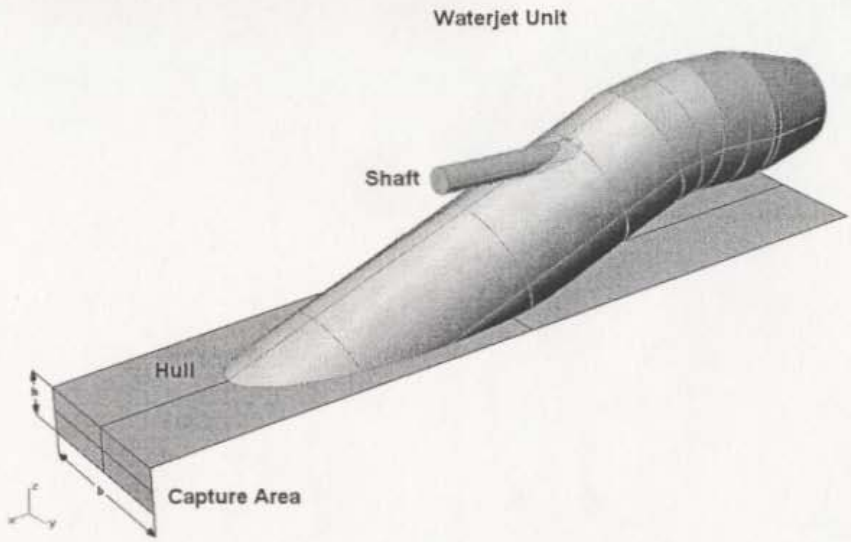

Figure 4-3. Capture Area for Typical Waterjet

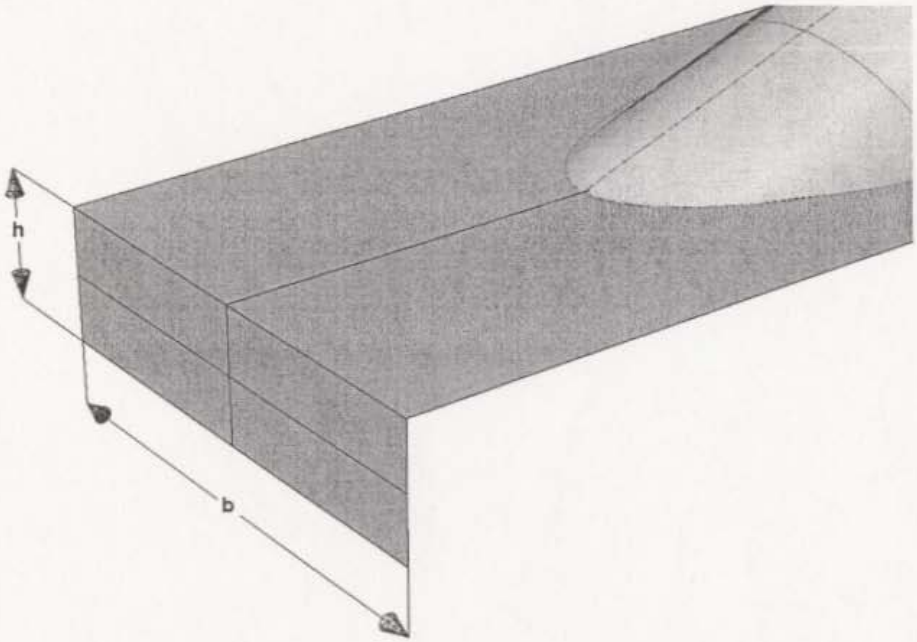

Figure 4-4. Capture Area Dimensions

Although the three-dimensional behaviour of the flow is recognised by the ITTC Committee, the flow is assumed to be constant across the width of the inlet, due to a lack of knowledge and expertise in this area. In order to obtain a better understanding of this, the ITTC recommends a sensitivity study be used to determine the effect of various intake shapes.

Concerns have also been raised in regard to the state of the intake opening in determining the velocity profile. Ideally the effective wake ingested by the intake, i.e. the flow field including the suction effects on the flow about the hull, should be measured. The effective wake is difficult to measure and it is therefore suggested by the 23rd ITTC Specialist Committee on the Validation of Waterjet Test Procedures that the boundary layer velocity profile should be measured with closed intake openings (ITTC, 2002).

In order to calculate the size of the intake area h_1 and A_1 are determined implicitly from

$$Q_j = \int_{A_1} u_{1x}(z) \cdot dA_1 \qquad [4.1]$$

where,

Q_j – volume flowrate of the waterjet

A_1 – intake area at station 1a

$u_{1x}(z)$ – velocity profile at station 1a

The assumption of two-dimensional flow yields the following simplification

$$b_1 = 1.3(w_{inlet}) \quad [4.2]$$

$$Q_j = b_1 \cdot \int_0^{h_1} u_{1x}(z) \cdot dz \quad [4.3]$$

where,

w_{inlet} – width of inlet

b_1 – maximum width of the capture area

h_1 – height of the capture area

The momentum and energy flux for Station 1a are functions of the intake velocity profile, and therefore sensitive to the limitations described above. Further, frictional forces along the hull reduce the total head inside the boundary layer and the local energy velocity accounts for this by considering both kinetic and potential energy (Kruppa et. al., 1996):

$$\frac{V_E}{V} = \sqrt{\left(\frac{u}{V}\right)^2 + C_P} \quad [4.4]$$

where,

V_E – local energy velocity

V – ship speed

u – component of velocity in the direction of motion

C_P – static pressure coefficient given by the static pressure at Station 1a (p_1) and the static pressure in the undisturbed flow (p_o):

$$C_P = \frac{p_1 - p_o}{\frac{1}{2} \cdot \rho \cdot V^2} \qquad [4.5]$$

The momentum flux at Station 1a is given by:

$$M_1 = \rho \cdot \int V_{E1} \cdot dQ_J \qquad [4.6]$$

where,

$$dQ_J = u_{jx} \cdot dA_j \qquad [4.7]$$

The energy flux at Station 1a is given by:

$$E_1 = \frac{1}{2} \rho \int_{Q_1} V_{E1}^2 \cdot dQ_J \qquad [4.8]$$

4.3 Intermediate Stations

In general, the momentum and energy flux can be determined at each of the locations between Station 1a and Station 7 to account for the losses along the waterjet unit. An accurate description of the velocity profiles at the intermediate stations can be difficult, especially near the impeller, or when small model scales are involved. It has been suggested that numerical simulations used in conjunction with large or full-scale model tests may be used to develop a greater appreciation of the dynamics of the waterjet system (Thornhill, 1999).

The energy flux at the intermediate stations is determined by integrating the local energy velocity at station 'j', and is given by:

$$E_j = \frac{1}{2} \cdot \rho \cdot \int_{Q_j} V_{Ej}^2 \cdot dQ_j \qquad [4.9]$$

The energy flux for the undisturbed flow ahead of the vehicle, Station 0, is:

$$E_0 = Q_j \cdot \frac{1}{2} \cdot \rho \cdot V^2 \qquad [4.10]$$

4.4 Vena Contracta

The cross sectional area of the waterjet is decreased at the nozzle in order to maximise the thrust. Streamlines from the outlet nozzle contract after the orifice to a minimum value when they all become parallel, at this point, the velocity and pressure are uniform across the jet. This convergence is called the *vena contracta*, from the Latin 'contracted vein'. If the exit is not a perfectly smooth contour, the diameter of the jet will be less than the diameter of the hole (Munson et al., 1998) and it is necessary to know the amount of contraction to calculate the momentum flux. At the vena contracta, the static pressure coefficient is zero and the energy associated with the fluid is kinematic.

If the flow rate through the waterjet is known, the momentum flux can be determined as follows:

$$M_7 = \rho \cdot \int_{Q_J} u_{7x} \cdot dQ_J + \int_{A_7} (p_7 - p_0) \cdot dA_7 \qquad [4.11]$$

The pressure reduction ($p_7 - p_0$) caused by tangential velocities of the jet ($u_{7\phi}$), is found from:

$$p_7 - p_0 = -\rho \cdot \int_{r}^{R_J} \frac{u_{7\phi}^2}{r} dr \qquad [4.12]$$

where,

A_7 – cross sectional area of the jet

R_J – radius of the jet

The Energy Flux at Station 7 is calculated from:

$$E_7 = \frac{1}{2} \cdot \rho \cdot \int_{Q_J} V_{E_7}^2 \cdot dQ_J \qquad [4.13]$$

The local energy velocity at Station 7, V_{E7}, accounts for the tangential and rotational components of the jet flow:

$$V_{E7} = \sqrt{u_{7x}^2 + u_{7\phi}^2 + \frac{2}{\rho} \cdot (p_7 - p_0)} \qquad [4.14]$$

4.5 Propulsion Performance Calculations

The values for the momentum energy flux throughout the waterjet system can be used to determine the propulsion performance characteristics of the waterjet.

Change of Momentum Flux

The change of momentum, ΔM, can be written as:

$$\Delta M = M_7 \cdot \cos\alpha - M_1 \qquad [4.15]$$

where,

α - angle between the centreline of the jet and the horizontal plane.

According to the Kruppa et al. (1996), the change of momentum is equal to the sum of the forces on the pump and the internal ducting, plus the change of hull resistance due to the action of the waterjet. This is also equal to the effective model resistance minus the tow-rope force, and the effective full scale resistance is computed from:

$$R_S = \frac{\rho_S}{\rho_M} \cdot \Delta M \cdot \lambda^3 \qquad [4.16]$$

where,

λ - scale factor

ρ_m – fluid density at model scale

ρ_S – fluid density at full scale

Effective Jet System Power

The effective jet system power is computed from the increase in energy between Station 1a and Station 7:

$$P_{JSE} = E_7 - E_1 \qquad [4.17]$$

Elevation Power

The power necessary to lift the water above the undisturbed water surface to a height h_J is computed from:

$$P_{EL} = \rho \cdot g \cdot Q_J \cdot h_J \qquad [4.18]$$

Internal Losses

The loss coefficients for the intake, ζ_{13}, and diffusor, ζ_{57}, are computed from:

$$\zeta_{13} = \frac{E_1 - E_3}{E_0} \qquad [4.19]$$

and

$$\zeta_{57} = \frac{E_5 - E_7}{E_7} \qquad [4.20]$$

In most situations, the velocity distribution at Station 3 will be non-uniform with large variation, and difficult to obtain. In general, it is difficult to measure the velocity distribution at any position inside the waterjet system during self–propulsion tests, and one may conclude that internal loss coefficients may be obtained through separate test rigs with large scale factors, or an accurate numerical model (Thornhill 1999).

The power needed to overcome the inlet and outlet losses can then be determined from:

$$P_{IL} = \zeta_{13} \cdot E_0 + \zeta_{57} \cdot E_7 \qquad [4.21]$$

Effective Pump Power

The effective pump power is the sum of the power contributions described previously:

$$P_{PE} = P_{JSE} + P_{EL} + P_{IL} \qquad [4.22]$$

If the increase of mean total head across the pump is expressed as:

$$H_{35} = \frac{1}{\rho \cdot g \cdot Q_J} \cdot [E_7 \cdot (1 + \zeta_{57}) - E_1 + E_0 \cdot \zeta_{13}] + h_J \qquad [4.23]$$

The effective pump power can also be expressed as:

$$P_{PE} = \rho \cdot g \cdot Q_J \cdot H_{35} \qquad [4.24]$$

Model Shaft Power

If the inflow non-uniformities are accounted for by the pump installation efficiency, η_{inst}, and the pump efficiency, η_P, is known, the power needed to propel the model can be expressed as:

$$P_{DM} = \frac{P_{PE}}{\eta_P \cdot \eta_{inst}} \qquad [4.25]$$

The model shaft power can also be determined from torque measurements. If the P_{DM} is not equal to:

$$2 \cdot \pi \cdot Q \cdot n \qquad [4.26]$$

then the internal loss coefficients or efficiency values should be reconsidered.

4.6 Predicted Full Scale Power

In order to determine the full-scale power of the waterjet system, the volume flow rate, size of intake area, and energy velocities at Station 1 and Station 7 must be known. Scale effects of the boundary layer profile do not permit a direct conversion of these quantities, and it is necessary to follow the procedure outline by Kruppa et al. (1996).

- The full-scale boundary layer thickness and velocity profile are predicted according to boundary layer theory and the hull roughness is considered. The static pressure coefficient is considered to be the same for the model and prototype.
- Momentum theorem is used to compute the values of Q_J, M_1, h_1, and M_7 using the full-scale velocity profile and maintaining the change in momentum flux:

$$\Delta M_S = R_S = \frac{\rho_S}{\rho_M} \cdot \Delta M_M \cdot \lambda^3 \qquad [4.27]$$

- Full-scale values of E_1 and E_7, ζ_{13S}, ζ_{57S}, η_{PS}, and η_{instS} are estimated

If a large, or full-scale model is used to determine these quantities, the results can be converted with some confidence (Thornhill, 1999).

The full-scale effective pump power can then be determined as described in sections 0 through 0. The pump shaft power is then:

$$P_{DS} = \frac{P_{PES}}{\eta_{PS} \cdot \eta_{instS}} \qquad [4.28]$$

4.7 Summary

The momentum flux method, initially proposed in the "Final Report and Recommendations to the 21st ITTC: Waterjets Group" (Kruppa et al., 1996), has been regarded as a step in the right direction as far as waterjet testing is concerned. The method has many advantages over conventional testing methods when applied to

waterjets, and has undergone significant refinements, particularly those of the 23rd ITTC (2002).

The method relies heavily on an accurate description of the flow rate. This can be accomplished with a reliable flow meter, but scale model waterjets do not often allow space for such a device, to say nothing of the settling length required prior to the meter inlet. In addition to this, assumptions of the flow behaviour necessary to simplify the analysis at key locations of the waterjet system, coupled with the estimation of model efficiencies leaves room for improvement in the method. Large-scale model testing and/or numerical simulation may improve confidence in full-scale predictions.

The work discussed in this thesis has been undertaken at full scale, and the momentum flux calculations benefit from numerical analysis. The numerical data allows integration over thousands of data points which would prove near impossible to measure experimentally.

5 Instrumentation

5.1 Hot-Wire Anemometry

The origins of practical hot-wire anemometry can be attributed the work of Ziegler (1934). He developed a constant temperature anemometer to measure flow fluctuations using a feedback amplifier that maintained constant temperature across a heated wire. Hot wire anemometry makes use of the thermal loss of heated resistance sensors in order to determine velocity fluctuations. A sensor is placed in a gaseous flow, and the convective heat transfer from a heated wire is measured. The magnitude of the convection is influenced by changes in temperature, pressure, and velocity and the sensor will immediately detect any change in the fluid condition that affects the heat transfer from the heated element. If only the velocity of the flow changes, or the influence of other changing parameters is eliminated by suitable circuitry, then the instantaneous heat loss of the sensor is a direct measurement of the fluid velocity at that point in time.

Hot wire anemometry can be divided into the following flow regimes:

- Subsonic incompressible flow
- Subsonic compressible, transonic, and low supersonic flows
- High supersonic and hypersonic flows

These flow regimes can be further separated into continuum flow, slip flow, and free molecular flow. For the purposes of this discussion, only subsonic incompressible continuum flow will be considered.

In subsonic incompressible flow, the heat transfer from a wire is a function of mass flow, total temperature, and wire temperature. For constant density, the mass flow variations depend only on velocity fluctuations. In most cases, the mean free path of the particles is much less than the diameter of the wire sensor, and the continuum model is valid; conventional heat transfer methods therefore apply.

Neglecting conduction and radiation, the heat balance for an electrically heated wire is given by (Stainback et al., 1997):

Heat Stored = Electrical Power In – Aerodynamic Heat Transfer Out

$$\frac{dc_w}{dt}T_w = P - Q \qquad [5.1]$$

$$\frac{dc_w}{dt}T_w = I^2 R_w - \pi L d_w h(T_w - T_{adw}) \qquad [5.2]$$

where:

c_w – specific heat of wire

T_w – temperature of wire

T_{adw} – adiabatic wall temperature

I – current

R_w - resistance of wire

L – characteristic length

d_w – diameter of wire

h – coefficient of heat transfer

Setting the heat storage term to zero results in the following:

$$I^2 R_w = \pi L d_w h(T_w - T_{adw}) \qquad [5.3]$$

There are several circuits that may be used to measure the thermal loss across a sensor. Using relatively simple compensation circuitry, the Constant Temperature Anemometer (CTA) is capable of measuring very rapid velocity fluctuations. The instrument supplies a sensor heating current that varies with the fluid velocity to maintain constant sensor resistance and constant sensor temperature.

In it's simplest form, the CTA consists of a Wheatstone bridge circuit and a servo amplifier.

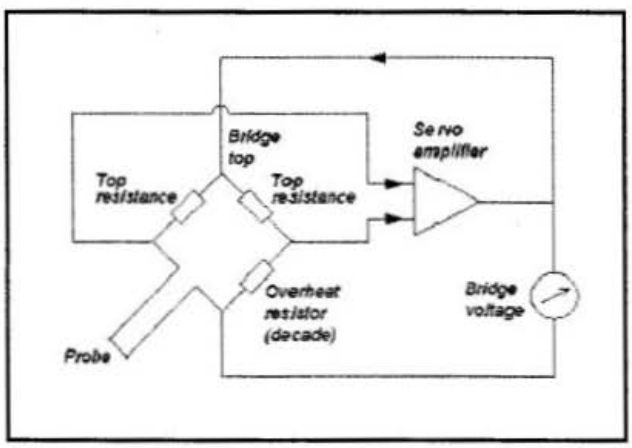

Figure 5-1. Wheatstone Bridge

The probe and two top resistances occupy the active bridge arm, while the passive bridge arm comprises the other top resistance, the comparison resistor, and various

compensating networks. When the bridge is balanced, there is no voltage difference across the end points of the bridge diagonal. A change in flow acting on the probe will cause the sensor to grow cooler, or hotter, depending on the nature of the flow. The change in resistance that follows, results in a voltage difference at the horizontal diagonal of the bridge, which is fed to the inputs of the servo amplifier. The servo amplifier then supplies an output voltage to the bridge unit such that the original temperature of the sensor is restored.

5.1.1 Advantages and Disadvantages of Hot-wire Anemometry

For the measurement of low and moderate turbulent flows (less than 25% turbulence intensity), the constant temperature anemometer has several advantages:

1. Cost – compared with Laser Doppler Anemometers (LDA), the CTA is relatively inexpensive
2. Frequency Response – Used in conjunction with a constant temperature anemometer, a standard hot-wire probe has a flat response from 0 to 50 khz (except at very low velocities). It is therefore relatively easy to obtain measurements up to several hundred kilohertz. Conversely, the LDA is normally restricted to frequencies less than thirty kilohertz.
3. Size – a typical hot wire sensor has a diameter less than fifty micrometers, and length less than 2 mm. This is convenient for experimental work, since care must be taken to ensure that the flow is not adversely affected close to the sensor.

4. Velocity Measurement – hot-wire probes with one, two, or three sensors can measure one, two, or three components of the velocity vector at a specific point, over a range of velocities from very low to high (compressible) speeds.
5. Signal to Noise Ratio – a resolution of 1 in 10000 is easily obtained in hot wire anemometry. This is far superior to the 1 in 100 resolution typical of LDA
6. Signal Analysis – the output of hot-wire anemometers is a constant analog signal, so analysis can be undertaken in both the time and frequency domains.

Limitations of Hot-wire Anemometry

Hot-wire anemometry is not without shortcomings. The following is a list of several areas in which researchers should pay careful attention (Bruun, 1996):

1. High-turbulence Intensity – Hot wire anemometers are restricted to low and moderate turbulence intensity flows. There are two sources of error associated with turbulence:
    - Errors can result from neglecting higher order terms in the series expansion for effective velocity.
    - Due to it's rotational symmetry, the wire element is insensitive to reversal of the flow direction which may occur in turbulent intensity flows
2. Probe Disturbance – the presence of the probe will alter the local flow field. For a well-designed probe, the errors will often be small and the disturbances will be

incorporated into the calibration procedure. For disturbance-sensitive phenomena such as flow separation, LDA is a more suitable alternative.

3. Liquid Flow – accumulation of fouling material on the sensor is often a concern when using hot-wire anemometers in liquid media. In most cases, a hot-film sensor is used.

4. Probe Breakage – hot-wire probes are delicate and most probes only last several months, depending on their usage. The probes can burn out or be damaged by fine particles in high-speed flows.

5. Hostile Environments – hot wire anemometry is not suitable for usage in hostile environments (e.g. Combustion), as the probe may break.

6. Heat Loss to Supports – There can be significant heat loss from the wire due to conduction to the relatively cold supports of hot-wire probes. The result is a temperature distribution along the wire that causes a variation of heat transfer.

7. Flow Direction – Single wire anemometers are incapable of determining the direction of flow. Multiple wire anemometers are therefore recommended if the directionality of flow is of concern.

5.1.2 Calibration and Experimental Set-up

In order to measure the velocity of air in contact with the anemometer, proper calibration is essential. This is achieved by following detailed calibration procedures provided with the constant temperature anemometer system.

The CTA system requires two supply voltages: one between +16 and +36 volts and another between –10 and –13 V DC. The positive supply voltage is required by the system to provide current to the hot-wire probe.

Velocity measurements were carried out using a DANTEC 55R11 single wire boundary layer type probe connected to a DANTEC 55M01 standard bridge. The sensor is a platinum-plated tungsten wire with particulars described in Table 5-1 (Dantec, nd):

Table 5-1. Anemometer Particulars

DANTEC 1	
Probe type	55R11
Sensor Resistance at 20° C	5.0 Ω
Leads Resistance	0.5 Ω
Effective length	1.25 mm

The velocity for the hot-wire calibration was measured using a 8360-M-GB VelociCal® Plus TSI air velocity meter. The analog output from the anemometer was sampled directly into a personal computer using an A/D converter and data acquisition software. Data was sampled at a frequency of 35 Hz for 60 seconds and were time averaged to obtain mean values for each point. For each calibration curve, ten data points were used. In order to obtain a functional relationship between the hot-wire signal (Volts) and the air velocity (m/s), a third order polynomial is recommended (Jørgensen, 2002), and can be expressed as:

$$U(E) = c_0 + c_1 E + c_2 E^2 + c_3 E^3 \qquad [5.4]$$

where U is the velocity recorded by the velocity meter, E is the anemometer output, and the constants c_0, c_1, c_2, and c_3 are obtained by a least squared fit of the data.

5.2 Wind Tunnel

Model tests were performed in an open circuit, low speed wind tunnel, located at Memorial University. The test section, measuring more than 20m in length, and having a cross section of 0.91m x 0.91m allows for the investigation of relatively large boundary layers. This alleviates some of the spatial resolution problems associated with hot-wire anemometry described in section 5.1.1.

A centrifugal blower, equipped with motorised variable angle inlet vanes and powered by a 19kW motor, is used to force wind through the tunnel and adjust the wind velocity in the test section. The air first passes through a screened diffuser, then through three single precision screens located in a large settling chamber, and is finally accelerated into the test section using 5:1 contraction.

The maximum free stream velocity that can be achieved is approximately 15m/s and the free stream turbulence intensity is no larger than 0.5% at all velocities (Sutardi 2002).

5.3 Induction Motor and Inverter

A 1.5hp three-phase motor was used in conjunction with a Yaskawa J7 general-purpose inverter to turn the shaft of the waterjet system. Initially a Kempf & Remmers propeller motor was to be used, but it could not provide sufficient power to drive the installed

impeller, which was much larger than the small-scale propellers typical of self-propulsion tests. The motor is standard laboratory equipment from Memorial University and the inverter was purchased separately in order to provide dedicated service to the waterjet system. Chosen for its reliability and low cost, the J7 inverter is capable of controlling motors with power ratings up to 2 hp.

5.4 Dynamometer

Dynamometers are used to determine the load applied to a system by an external load (motor). The Kempf & Remmers propeller dynamometers used in this study have a reputation for reliability and accuracy second to none. These instruments are the workhorses of modern hydrodynamic laboratories and have been designed for low weight and low friction. Many are currently in use world-wide and are suitable for use within model ships (unsealed designs) and on Towing Carriages and pressurised Cavitation Tunnels (waterproof designs). The unsealed designs are suitable for this study because there is no requirement for a watertight environment.

The measurements of thrust and torque provided by the dynamometer are suitable for validating the power predictions of the momentum flux method, outlined in Chapter 4.

The following data summarises the dynamometer technical specifications (Kempf & Remmers, n.d.):

Table 5-2. Dynamometer Technical Data

Kempf & Remmers R 25/8 Dynamometer	
Rated Torque	10 Nm
Rated Thrust	250 N
Overload in torque permitted for a short moment	25%
Overload in thrust permitted for a short moment	25%
Maximum speed (rpm) with propeller shaft	2000 rpm
Torque measuring system	Full bridge strain gauge (240 Ohm)
Thrust measuring system	Full bridge strain gauge (120 Ohm)
Current supply	d.c. or a.c.
Recommended feed-in voltage for torque measurement	4 - 8 V
Recommended feed-in voltage for thrust measurement	2 - 6 V
Maximum feed-in voltage for thrust measurement	20 V
Maximum feed-in voltage for torque measurement	10 V
Sensitivity at rated torque and thrust (mV output voltage)/(V feed-in voltage)	1.6
Total length	405 mm
Net weight	3 kg

The transducers used for torque and thrust measurements are temperature compensated and equipped with full measuring bridges of the strain gauge type (Schneider, 1984). In addition, the thrust is measured at a transducer that is not influenced by the torque, and does not rotate. Similarly, torque is measured at a rotating transducer and is not affected by thrust.

The analog signals from the dynamometer are transmitted to the data acquisition system via an Omega OM3 series signal conditioner.

5.5 Data Acquisition

The task of data acquisition (DAQ) hardware is to collect incoming analog input signals and convert them to digital signals for further processing, storage, and display. Enhanced with data acquisition hardware, a personal computer is the perfect vehicle for this activity. Thrust, torque, and velocity measurements transmitted from the various

instruments in terms of voltages can be read into computer memory through plug-in DAQ boards that contain analog-to-digital converters. A variety of software packages, such as LabVIEW® and DAQVIEW® are available to support commercially available data acquisition boards

For the purpose of this study a National Instruments PCI-6024E DAQ board was used in conjunction with LabVIEW software to acquire data. The PCI-6024E board delivers 12-bit resolution on up to 16 single ended analog inputs, and has been designed for superior integration with LabVIEW.

The following figure illustrates the instrumentation connections:

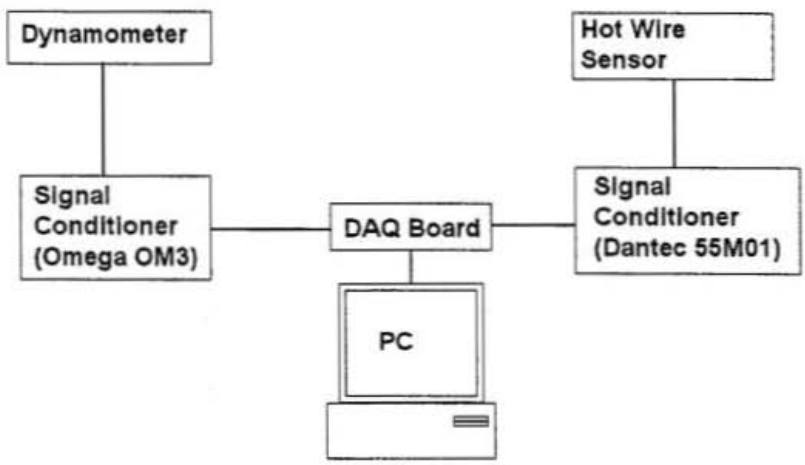

Figure 5-2. Data Acquisition and Instrumentation

5.6 User Interface

In order to monitor the data being acquired through the course of any particular test, and to trigger the recording of data, a graphical user interface (GUI) was created using LabVIEW programming tools. An example of this is shown in Figure 5-3, where torque, thrust, and wind velocity are being monitored. It should be noted that the rpm channel was linked to the original Kempf and Remmers propeller motor, and was not used in the experiment's final assembly.

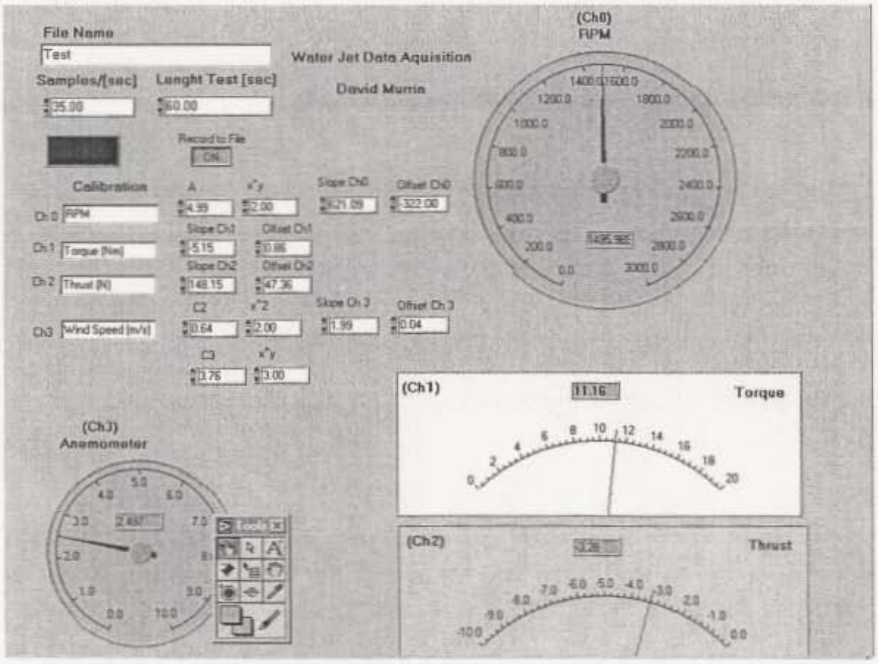

Figure 5-3. Data Acquisition GUI

The data collected was stored in EXCEL® spreadsheets and imported into Matlab® for statistical and graphical analysis. Details on the particular manipulation and interpretation of data are provided in the chapter on model testing (Chapter 6).

A similar graphical user interface was created for the calibration of instruments. Using the set-up described in Figure 5-2, the calibration program allows the user to collect a series of data points sufficient to relate instrument response to real-world data such as torque, thrust, and velocity.

The ensuing chapter describes the testing of a waterjet system using the instrumentation described.

6 Model Testing

6.1 Introduction

Waterjet propulsion makes use of Newton's Third Law of Motion – 'every action has an equal and opposite reaction', such that thrust is generated when water is forced in a rearward direction. The discharge of a high velocity jet stream creates a force in the opposite direction that is transferred through the jet and into the hull body, thus propelling it forward. Accelerating a mass of water creates a thrust that is proportional to the change in momentum between the water entering and leaving the waterjet system. (Allison, 1992)

Water enters the jet unit through the intake and a shaft-driven propeller and stator increase the pressure of the flow (Figure 6-1). The high-pressure flow is discharged at the nozzle and exits as a high velocity jet stream. Steering is accomplished by changing the direction of the flow exiting the nozzle of the jet. The force of the stream in one direction moves the stern of the boat in the opposite direction, putting the vessel into a turn. The vessel can be kept on station, or reversed, by deflecting the exiting jet stream forward and down to varying degrees.

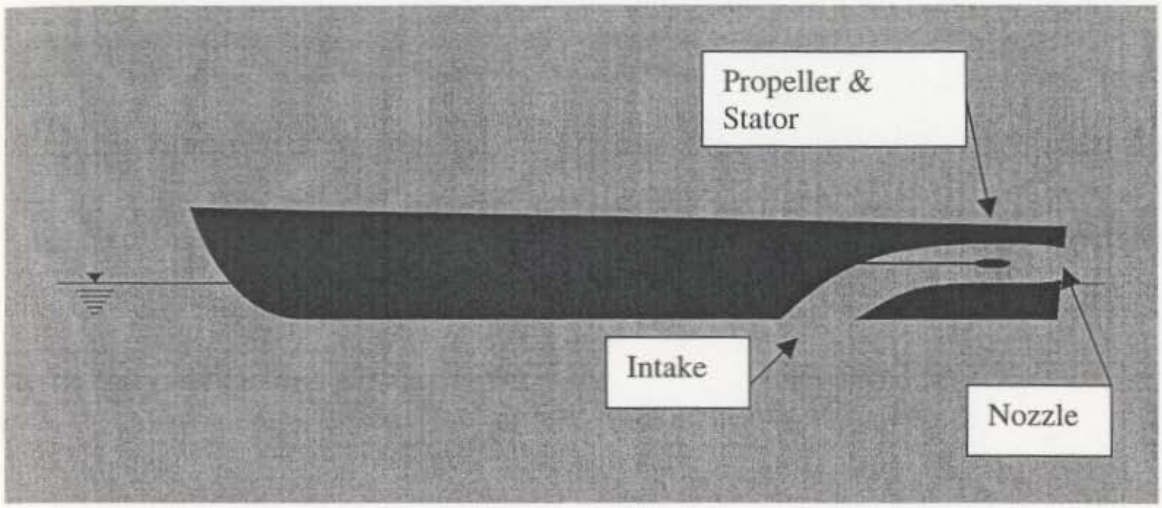

Figure 6-1. Waterjet Definitions

As noted in the discussion of the Momentum Flux Method (Chapter 4), waterjet testing methods have been constantly evolving in recent years. This is due, in part, to the unique differences between traditional methods of propulsion and waterjet propulsion.

Due to the high speeds normally inherent to waterjet propelled craft, scaling is often a concern with traditional testing methods, since the models are often limited to a small size. Velocity measurements at the inlet are critical for accurate evaluation of thrust and power, and the speed limitations of most tow carriages restrict the diameter of the inlet tremendously, by virtue of similitude and scaling. This becomes problematic when flow measurements are required, since the physical dimensions of a single velocity probe can disturb the flow in this area. Geometric similarity, then, is also difficult to maintain for small-scale models due to structural, and spatial limitations.

It has been proposed that large-scale testing of waterjets may be accomplished using a wind tunnel. The wind tunnel is used to simulate the flow around the boundary layer

under a ship's hull and an accurate representation of the inlet duct joins the wall of the wind tunnel to the waterjet system. The flow through the wind tunnel is analogous to vessel speed and a full-scale waterjet model can be attached to the outside wall of the wind tunnel.

The waterjet system can be tested at a series of wind and impeller speeds.In these tests, using hot-wire anemometry, velocity measurements were taken at multiple locations throughout the waterjet assembly to provide an accurate description of the system's flow characteristics. Figure 6-2 provides an illustration of a waterjet being tested using the wind tunnel. This set-up shows the waterjet system on its side, that is, the side of the wind tunnel behaves similar to the underside of a ship's hull.

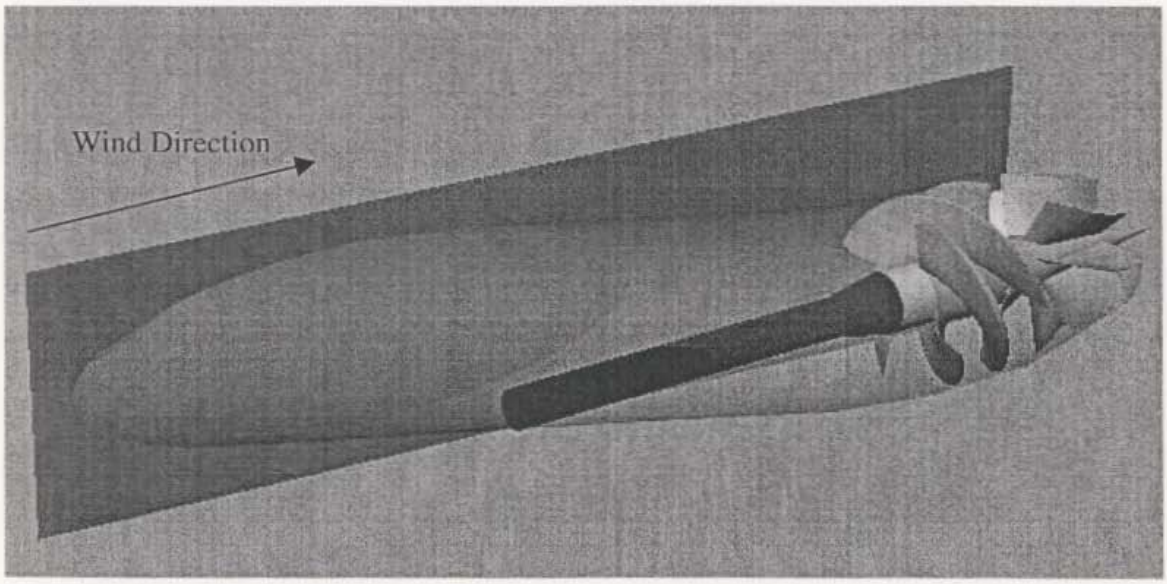

Figure 6-2. Typical Set-up for Testing a Waterjet System using a Wind Tunnel

Some advantages of testing waterjets in a wind tunnel compared to testing in a water tunnel or tow tank are:

- Discharge to laboratory is not harmful
- Model need not be watertight, so the construction of a waterjet model is much simpler
- Ease of access to measuring sections

The following chapter describes experiments performed on a full-scale waterjet model operating in a wind tunnel.

6.2 The Model

6.2.1 Background

In order to address the problems associated with conventional waterjet testing, Etienne Duplain and Hugo Royer, undergraduate engineering students at Memorial University of Newfoundland (MUN), proposed that a waterjet model be tested at Memorial University. At the suggestion of Dr. Neil Bose, a professor of ocean engineering and naval architecture at MUN, it was decided that the waterjet would be tested in wind tunnel located at Memorial University of Newfoundland. With the assistance of technical staff, a waterjet model was constructed based on a commercially available waterjet built by Alpha Power Jet, Quebec. This waterjet is typically installed on fishing boats or passenger craft. The 15m Explorathor fishing vessel built by Recherches et Travaux Maritimes, for example, is equipped with two of these waterjets and is capable of carrying about 5000 kg of load at 26 knots. Construction drawings for the waterjet unit are provided in Appendix A.

The base plate and duct brackets were built from plywood, and the duct, pump section, and nozzle walls were made from Lexan ® transparent plastic sheets. This was possible because the original design incorporated developable sections. A lathe was used to form the 5/8-inch aluminium shaft and wooden bearing support and nozzle cone. Due to time limitations, the impeller was made from developed flat 1/8-inch aluminium sheets and bent to give a rough representation of the shape of the commercial impeller.

The model that resulted was innovative, but some modifications were required in order to perform any meaningful tests. Some of the problems associated with the original model included:

1. Inadequate impeller
2. Insufficient stiffness of the base plate
3. Warped shaft
4. Fluid velocity measurement scheme was incomplete
5. Inadequate motor

6.2.2 Improving the Impeller

The original impeller was made from developed blade shapes and cut out in flat aluminium sheets (Duplain et al., 2002). As such, there was no thickness distribution to the impeller blades and the hydrodynamic lift and drag forces on each blade of the impeller were inaccurate. A new impeller was therefore required that accurately represented the shape and behaviour of the impeller used in the commercial waterjet.

Based on the 2-dimensional impeller diagrams provided in Appendix A, an impeller was modelled using Rhinoceros® computer aided drafting software and is shown in Figure 6-3:

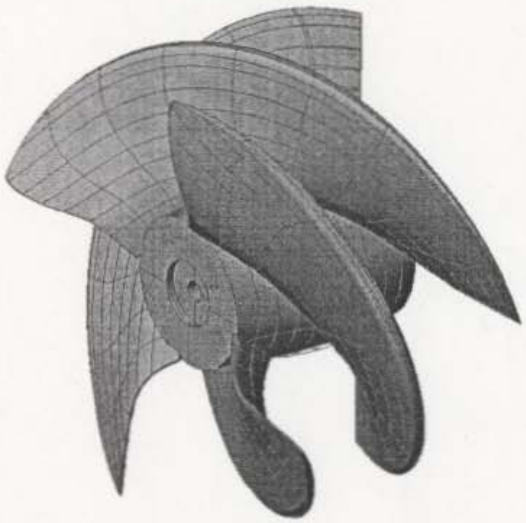

Figure 6-3. Computer Generated Impeller Model

In order to translate the computer model into a physical impeller, some further modification was required. In theory the trailing edges of each blade can be designed to a very fine point using computer software. Tolerance restrictions and strength requirements, however, limit physical models and the thickness at the trailing edges of the computer model was therefore increased to accommodate these constraints.

Rapid Prototyping (RP)

Rapid prototyping is one technology that enables the production of real objects from computer aided design (CAD) data. It is the process by which an object is built from a series of stacked cross sections developed by a 3-dimensional computer model. The

advantage of RP technology is that it allows for almost total geometrical freedom in building parts that would have previously required many machining operations, or proven impossible to build.

There are four principal rapid prototyping systems in use today

1. Stereolithography (SLA)
2. Selective Laser Sintering (SLS)
3. Fused Deposition Modeling (FDM)
4. Laminated Object Manufacture (LOM)

The first three of these techniques use plastic resins and the last uses glued paper. The Rapid Prototyping Centre, located in the Engineering building at Memorial University is equipped with a LOM system and a small SLS. There is no requirement for watertight integrity for the model impeller of this study and the forces experienced during testing in air were expected to be much less that those for the prototype in water. For these reasons, the LOM was a suitable system for the production of the model impeller.

Laminated Object Manufacture – LOM

A simple diagram of a LOM system is shown in Figure 6-4. Layers are built by pulling a sheet of pre-glued paper across a base plate and fixing it in place using a heated roller that activates the glue.

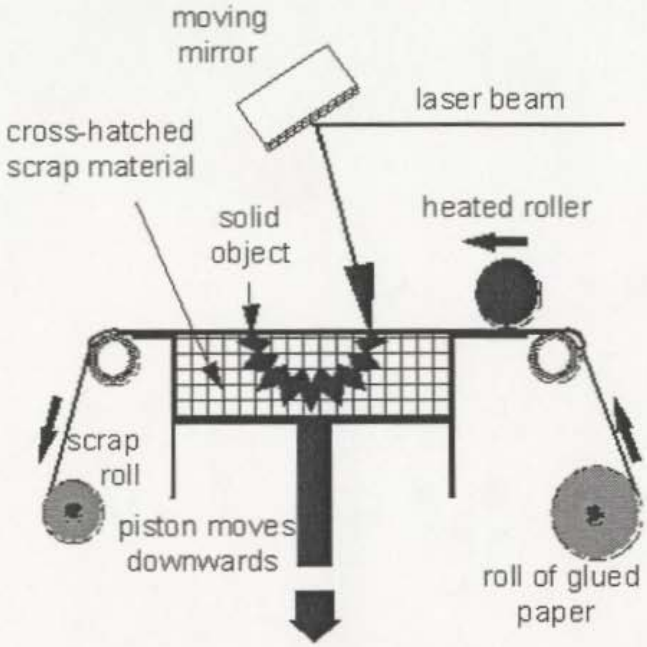

Figure 6-4. Laminated Object Manufacture System

The outline of each cross section is cut out of the paper using a laser with sufficient intensity to cut through a single sheet. The base plate (piston) descends and the process repeats until all of the cross sections have been cut. At the end of the build session, excess material is removed to free the object. The built parts look like wood when finished, but absorb moisture quickly and must be post processed immediately with an epoxy that was specially designed for LOM technology. Although it suffers from the 'stair stepping effect' inherent to building objects in layers with a finite thickness, the accuracy of LOM models is surprisingly good (Shellabear, 1998). Reeves and Cobb (1996) tested the dimensional accuracy of LOM technology on a specially designed test part and on the average, reported a 0.4% deviation from the computer aided drafting CAD model. The stair stepping effect also results in a poorer surface finish than other RP

methods, but objects built using the laminated object manufacture system are often quite robust and can be hand finished and varnished to improve structural integrity. Because the raw material, paper, is cheap, the LOM is particularly suitable for large models.

Stereolithography (STL), or .stl, files are the standard input for LOM systems. It is a list of the triangular surfaces that describe a computer-generated solid model. STL specifications require that all adjacent triangles share two common vertices, and contain completely closed (watertight) polygon mesh objects (McNeel 2002). The model impeller file was checked for watertightness, and modified as required, until a suitable STL file could be exported. The model impeller was then fabricated using the Memorial University LOM system and sealed to provide increased strength and durability.

An advantage of using rapid prototyping technology is that rotating parts do not require a great deal of balancing. The accuracy of the LOM mitigated the need for dimensional balancing as each of the blades were made exactly the same, and contained the same amount of material. Static balancing of the impeller was accomplished using stepwise refinement of the position of small weights attached to the inside of the impeller hub. These weights were moved until impeller movement was independent of blade position, and there was no tendency for the part to fall when resting in a vertical position.

6.2.3 Improving the System Stiffness

As illustrated in the fabrication drawings provided in Appendix A, very little structural support was initially designed for the waterjet system. Even with a balanced impeller, the vibrations induced by the rotating motor, and the air flowing through the wind tunnel

produced visible oscillation of the waterjet system. These oscillations were reduced a great deal by stiffening the base plate, and securing the wall of the wind tunnel. In addition to this, a warped shaft, likely the result of previous impeller imbalance increased the excitations. The problem of shaft warping was easily remedied by having another one made while solving the other problems required some modification to the original system.

In order to access objects in the wind tunnel, some of the side panels making up the walls of the wind tunnel were free to swing on hinges. It was observed during preliminary testing that the wall to which the waterjet unit was attached was experiencing considerable movement. The movement was attributed to insufficient securing of the panel to the wind tunnel when the hinges were in the closed position. As shown in Figure 6-5, two large pieces of 2x4 timber were used to join the wind tunnel wall and the swinging panel, which effectively closed the wall and prevented it from moving about it's hinges .

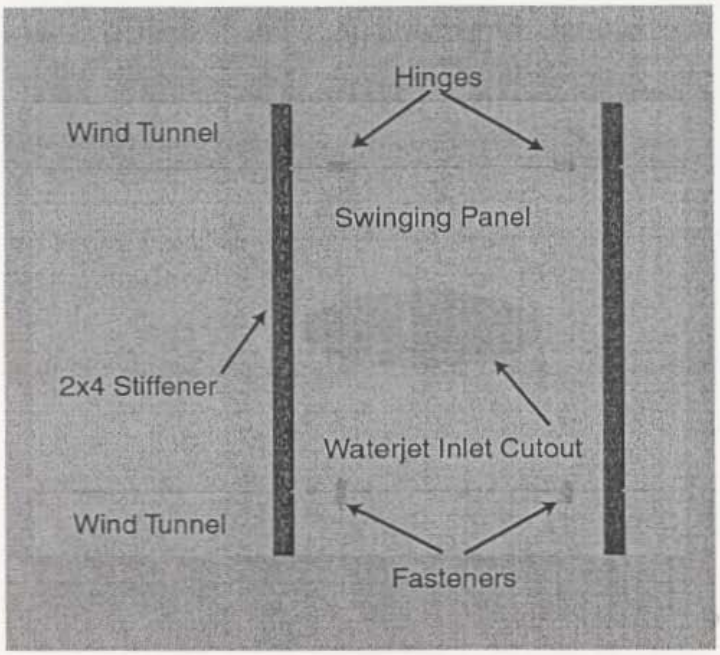

Figure 6-5. Closing the Wall of the Wind Tunnel

Figure 6-6 shows the original arrangement of the waterjet system. The duct section is formed from wooden brackets along the length of the waterjet system and attached to the side of the wind tunnel (wind tunnel wall). A motor drives the impeller and shaft, and forces were measured using a dynamometer. In the interest of clarity, only one of the duct brackets is shown. The original base plate configuration consisted of the dynamometer and motor support, along with the support bracket.

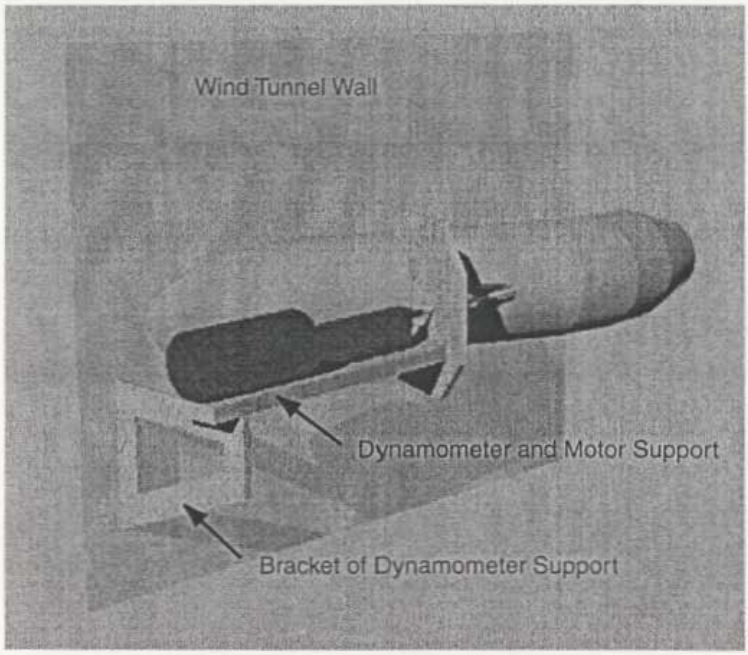

Figure 6-6. Original Baseplate and Bracket

This arrangement was not sufficient to control the oscillations of the system, and wooden support beams that extended all the way to the floor were required. The improved configuration is shown in Figure 6-7.

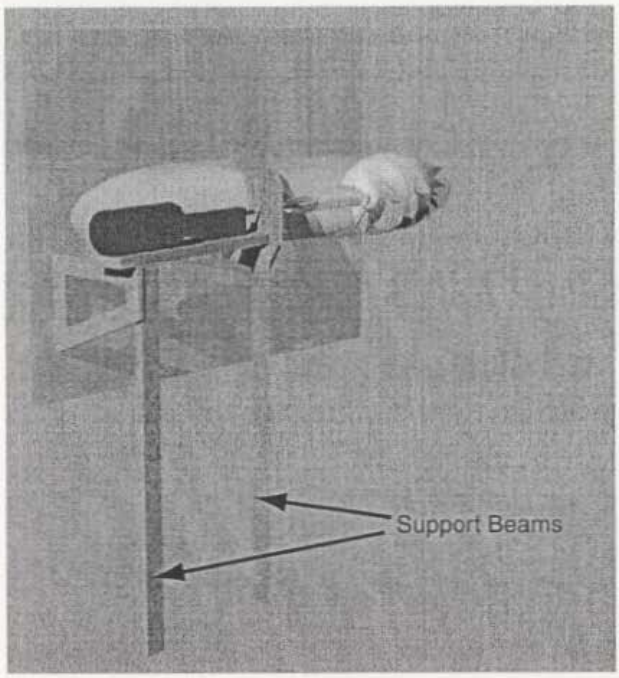

Figure 6-7. Stiffened Waterjet System

The modifications described in this section went a long way in improving the overall stiffness of the waterjet system. The balanced impeller, and enhanced structural support at the motor eliminated the oscillations previously observed, and drastically reduced the noise during regular operation.

6.2.4 Improving the Velocity Measurement Scheme

The time and financial constraints imposed on undergraduate students prevented a full analysis of the waterjet system (Duplain et al., 2002). In previous experiments, pressure measurements were taken at the inlet and outlet (vena contracta) using Pitot tubes, and converted to wind velocity. It was determined that in order to accurately describe the waterjet system at a given shaft speed, velocity measurements would be required at

several more locations. Hot-wire anemometry (Chapter 5) was chosen as the method for measuring wind velocity, and an entirely new method for measuring the wind velocity at various locations throughout the wind tunnel was necessary.

In order to obtain a complete description of the waterjet system behaviour, data was required at each of the stations specified in the momentum flux method (Chapter 4). To determine the behaviour at each station, a large number of sample points were required throughout its cross section. It was also necessary to insert the hot wire probe directly into the air stream, with as little disturbance to the velocity as possible. It was decided that a number of templates, identical in diameter to the individual station cross sections, would be installed directly below each station. The template consisted of a series of equally spaced holes corresponding to locations within the duct section and a mounting bracket was installed on the template that was constrained to vertical motion. The hot wire probe was then mounted to the bracket, and inserted through a small hole at the bottom of each station. Figure 6-8 shows the mounting bracket and Figure 6-9 shows the velocity template installed at station 2 of the waterjet system. Similar templates were used to measure velocity at each of the stations located inside the waterjet (i.e. stations 2 through 6).

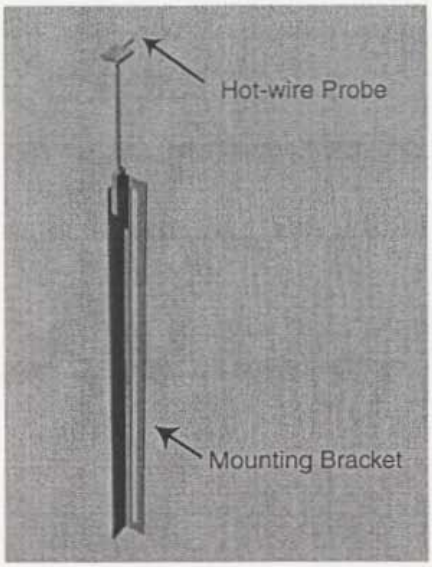

Figure 6-8. Mounting Bracket

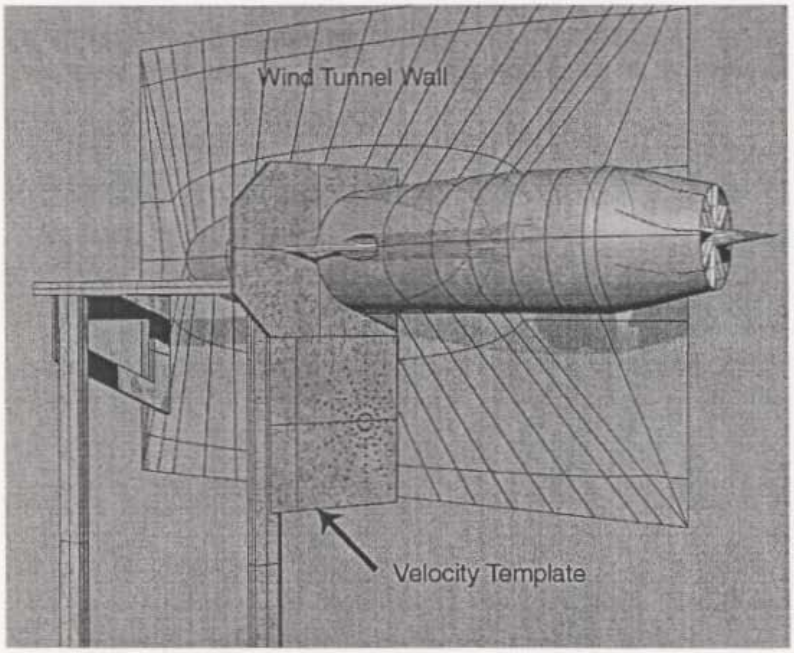

Figure 6-9. Velocity Template

In order to measure the velocity of air exiting the waterjet a separate part was required, and a stand was designed onto which the velocity template and mounting bracket could be installed. The part was free-standing and suitable for recording data at both the nozzle exit (station 6), and the assumed vena contracta (station 7). The position of the vena contracta was approximated by locating the position of maximum velocity of the jet stream. Figure 6-10 shows the template support equipped with the velocity template and mounting bracket. Velocity measurements were made by adjusting the position of the velocity probe with the mounting bracket:

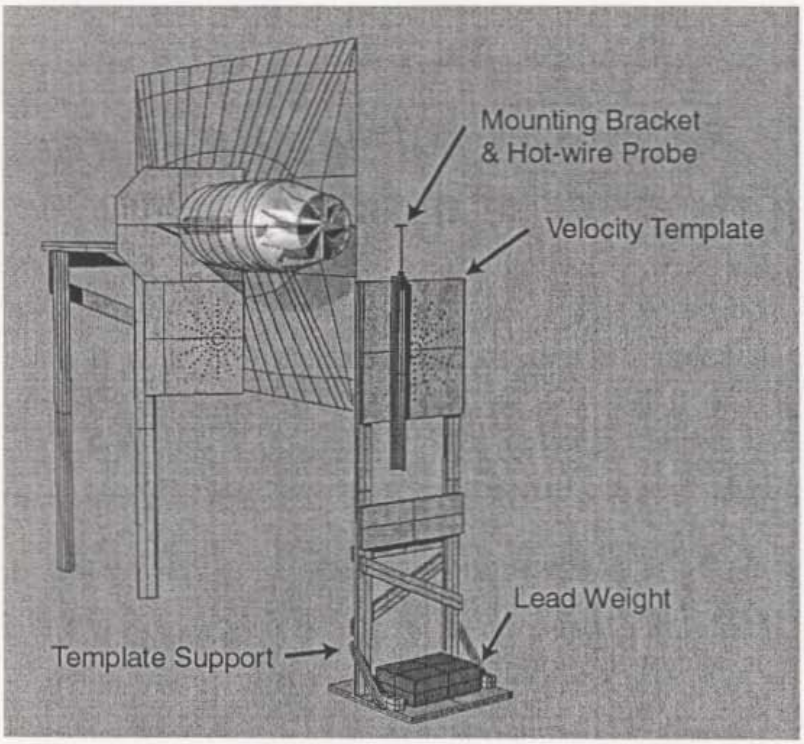

Figure 6-10. Template Support

The template support was positioned at the waterjet centerline, and parallel to the cross section at which data was being recorded. Figure 6-11 shows a top view of the template

support at the assumed vena contracta. The stand was moved closer to the waterjet system for measurements at the nozzle exit.

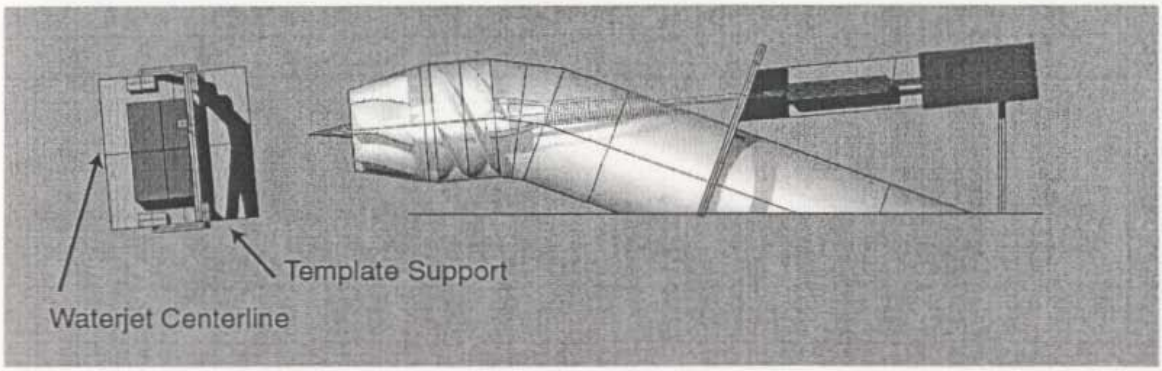

Figure 6-11. Top View of Template Support

Finally, the fluid behaviour at the wall of the wind tunnel was required in order to understand the flow characteristics at the waterjet inlet. Accurate velocity measurements were necessary at the undisturbed region at the far end of the wind tunnel (Station 0) and at the inlet (Station 1a). To accomplish this, a small bracket was designed to mount to the wall of the wind tunnel and a hot-wire support was built from a 5 mm aluminium cylinder. The cylinder was free to move in one direction and was scored every 5 millimetres so that velocity measurements across the wind tunnel could then be taken at very small increments. Figure 6-12 shows the bracket, cylinder and hot-wire probe assembly.

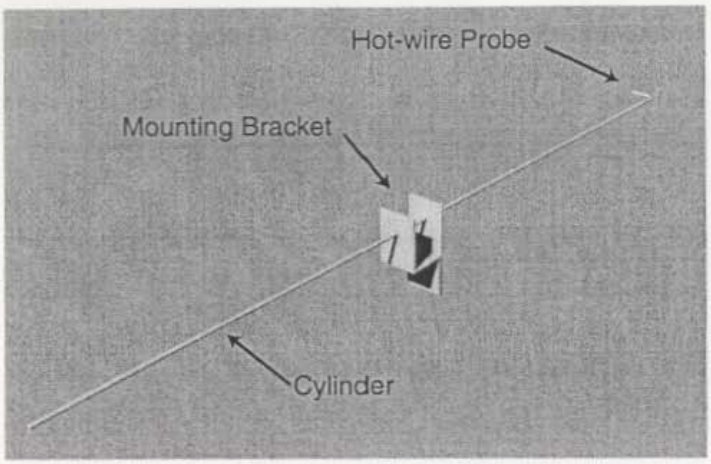

Figure 6-12. Wind Tunnel Bracket Assembly

An overall view of the test apparatus is shown in Figure 6-13. It should be noted that only one hot-wire probe was used for the tests and that the portable template support stand and wind tunnel bracket assembly were removed for tests inside the waterjet unit.

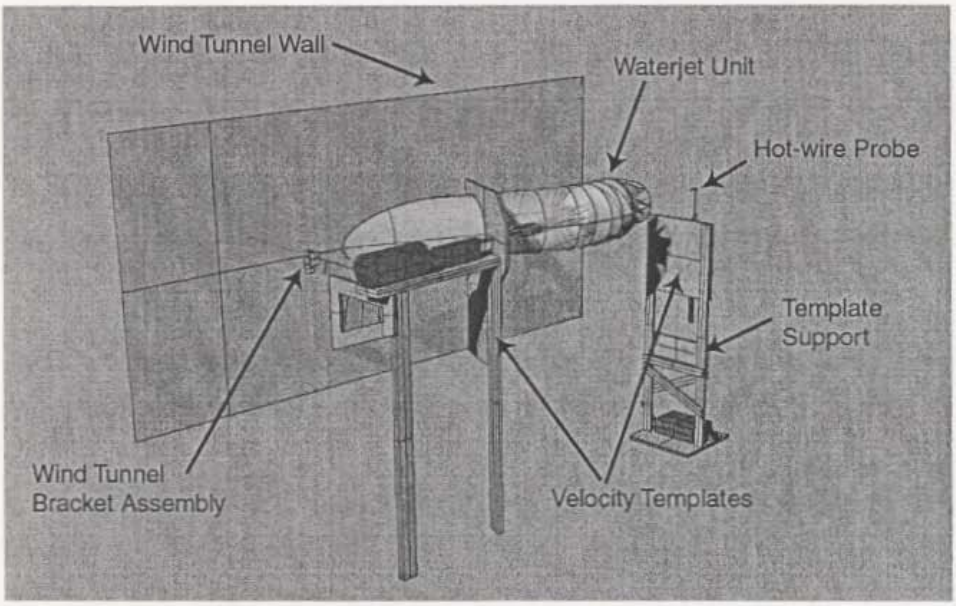

Figure 6-13. Testing Apparatus

6.3 Model Tests

6.3.1 Data Acquisition

Before formal testing could be done, a series of preliminary runs were necessary to determine suitable shaft speeds, and sampling frequencies. In order to fully understand the structural limitations of the model impeller, a series of destructive tests would have been required. These tests are both time-consuming and expensive. It was decided, then, that preliminary testing of the impeller should begin at low shaft speeds, and gradually increase to a safe operating level using engineering judgement.

Preliminary testing showed that at speeds greater than 1000 RPM, the impeller experienced increased vibration and noise. The behaviour of the part was unpredictable at such speeds and it was determined that the highest shaft speed that should be attempted was 1000 revolutions per minute.

The data obtained for time averaged analysis must be non-correlated. This can be achieved when the time between samples is at least two times larger than the integral time scale of the velocity fluctuations (Jørgensen, 2002). The following statistical parameters are required for the work of this study:

Mean velocity (U_{mean}):

$$U_{mean} = \frac{1}{N}\sum_{1}^{N} U_i \qquad [6.1]$$

where N is the number of samples and U_i represents the individual data points.

Standard deviation of velocity (U_{rms}):

$$U_{rms} = \left(\frac{1}{N-1} \sum (U_i - U_{mean})^2 \right)^{0.5} \quad [6.2]$$

Turbulence intensity (Tu):

$$Tu = \frac{U_{rms}}{U_{mean}} \quad [6.3]$$

In addition, the auto-correlation function is used to define the integral time scale, which is necessary to calculate the time interval between statistically uncorrelated data:

Auto-correlation function ($R_x(\tau)$):

$$R_x(\tau) = \lim_{T \to \infty} \frac{1}{T} \int_0^T x(t) \cdot x(t+\tau) \cdot dt \quad [6.4]$$

where T is the integral time scale and x(t) is a long time series sampled according to the Nyquist criteria.

Auto-correlation coefficien ($\rho_x(\tau)$):

$$\rho_x(\tau) = \frac{R_x(\tau)}{R_x(0)} \quad [6.5]$$

Integral time scale (T_I):

$$T_I = \int_0^\infty \rho_x(\tau) \cdot dt \quad [6.6]$$

The procedure for time averaged analysis using hot-wire anemometers is outlined below (Dantec 2002)

1. Estimate:

   Velocity, U [m/s]

   Turbulence intensity, Tu [%]

   Integral time-scale, T_I [s]

2. Select the desired uncertainty and confidence level:

   Uncertainty, u [%], in U_{mean}

   Confidence level (1-a) [%]

3. Calculate the sampling rate, *SR*:

$$SR \leq \frac{1}{2T_I}$$

4. Calculate the number of samples, *N*:

$$N = \left(\frac{1}{u} \cdot \left(\frac{z_a}{2}\right) \cdot Tu\right)^2$$, where $\frac{z_a}{2}$ is the variable related to the confidence level (1-a) of the Gaussian probability density function (Table 6-1):

Table 6-1. Confidence Levels for Gaussian Probability Density Function

$z_a/2$	(1-a)%
1.65	90
1.96	95
2.33	98

Velocity measurements were taken at a number of locations throughout the waterjet system and statistical analysis was performed. Preliminary data revealed an average turbulence intensity of 8.5% at stations 2,3,6, and 7 with inceased values near the wall of the waterjet, where the velocity appraoched zero. In addition to this, turbulence intensity at the impeller were much higher. Based on the auto-correlation function, the average integral time scale of the data collected was 9.25s, with maximum and minimum integral time scales 10.02 s and 7.26 s, respectively. It is recommended that the time between samples be at least twice this value, or at least 20s. The sampling rate was calculated to be:

$$SR \leq \frac{1}{2(10.02)} = 0.050$$

Typical uncertainty estimates for velocity data using hot-wire anemometry are around 3% and the maximum turbulence intensity that provides meaningful results is around 20% (Jørgensen, 2002). These values, along with a confidence level of 98 %, reveal a suitable number of samples to be:

$$N = \left(\frac{1}{3} \cdot (2.33) \cdot 20\right)^2 = 241$$

Based on these findings, it was decided that data would be sampled 35 times per second, for 10 seconds such that:

$$SR = \frac{1}{35} = 0.029$$

$$N = \frac{35 samples}{1s} \times 10s = 350 \text{ samples}$$

It is recognised that the sampling rate is low compared with the impeller rotation frequency (16 rps) and that data was only sampled twice per impeller revolution. The sampled data was therefore sensitive to pulsating effects in the impeller.

6.3.2 Test Matrix

Using the setup shown in Figure 6-13, velocity measurements were recorded at a shaft speed of 1000rpm and windtunnel velocity of 5 m/s. Recall from the section on the momentum flux method (Chapter 4) the following station locations:

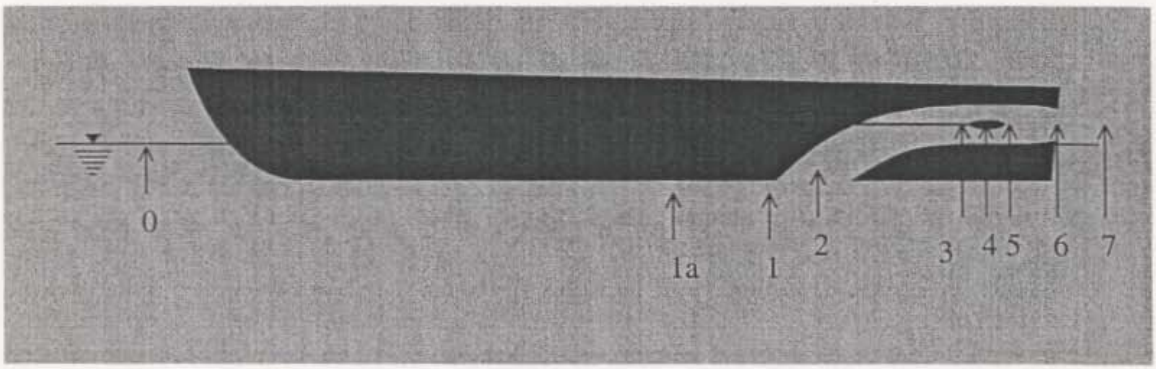

Station number	Location
0	Free Stream
1a	Inlet Velocity Profile
1	Inlet Point Of Tangency
2	Inlet Throat
3	Pump Face
4	Internal Pump Point
5	Pump Exit
6	Nozzle
7	Vena Contracta

Figure 6-14. Station Locations

The collected data was stored in Microsoft Excel ® spreadsheets and analysed using a Matlab® routine designed by the author. The routine, located in Appendix B was designed with a graphical user interface (GUI) that allowed the user to view the 1 dimensional data as velocity profiles and the 2 dimensional data as velocity contours.The exprimental data used in the Matlab routines is provided in Appendix C

Station 0

Station 0 was located at the end of the wind tunnel, far from the waterjet inlet. If the wall of the wind tunnel is modelled as a flat plate, then the following formula, known as the 1/7 power law, is a good approximation for experimentally observed turbulent flows (Acheson, 1998):

$$\frac{u}{U} = \left(\frac{y}{\delta}\right)^{\frac{1}{7}} \qquad [6.7]$$

where y is the distance from the plate (wall) and δ is the boundary layer thickness. The free stream velocity profile was measured using the windtunnel bracket described in Figure 6-12. Figure 6-15 shows a comparison of the measured velocities, labelled as 'Raw Data', and the theoretical approximation given by [6.7]. The free-stream velocity profile measured at station 0 is in close agreement with the theoretical approximation except at y=0, where $\partial u/\partial y = \infty$, and the equation is not valid.

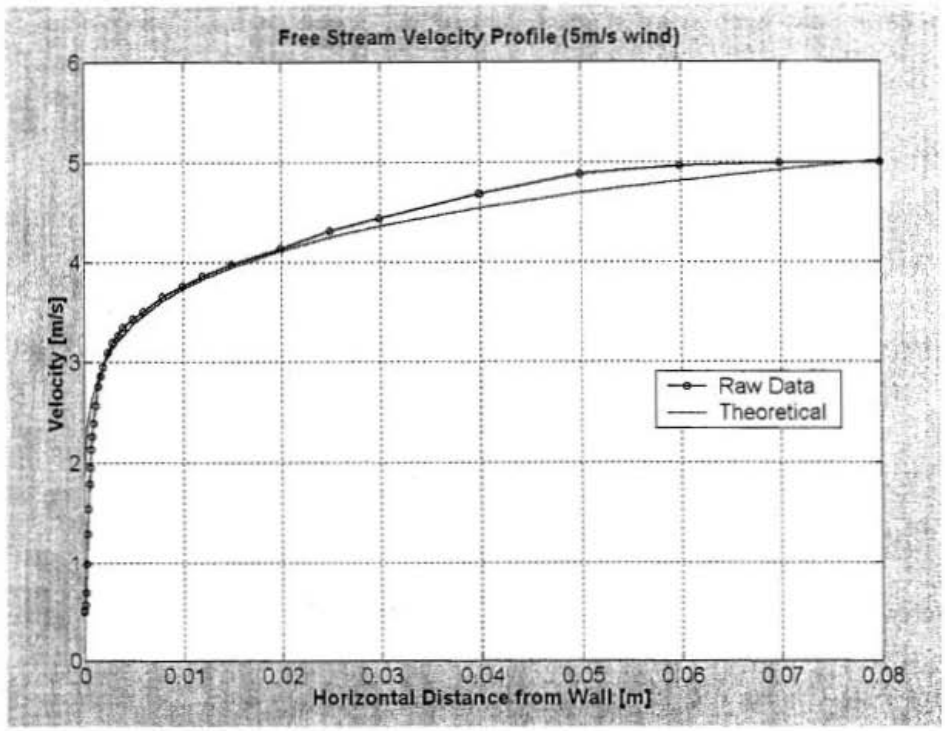

Figure 6-15. Free Stream Velocity Profile

Station 1a

The nature of the flow approaching the waterjet inlet was measured at station 1a. This station is important in the determination of the energy and momentum fluxes as it is from the change in fluxes between station 1a and station 7 that waterjet performance is evaluated. As noted previously, data at station 1a was recorded with the inlet closed (Chapter 4). The velocity profile at station 1a, given in Figure 6-16, shows that there is less agreement between the theoretical and experimental data at this station compared to the free stream. The discrepancy can be attributed to inconsistencies along the wall of the wind tunnel as the flow progressed. As fluid flowed from the free stream to station 1a, the

wall material changed from plywood to plastic and back to plywood. The transition from one surface to another caused disturbances in the flow that most likely resulted in small eddy currents near the wall, and subsequently higher velocities. The theoretical approximation is therefore less applicable at station 1a.

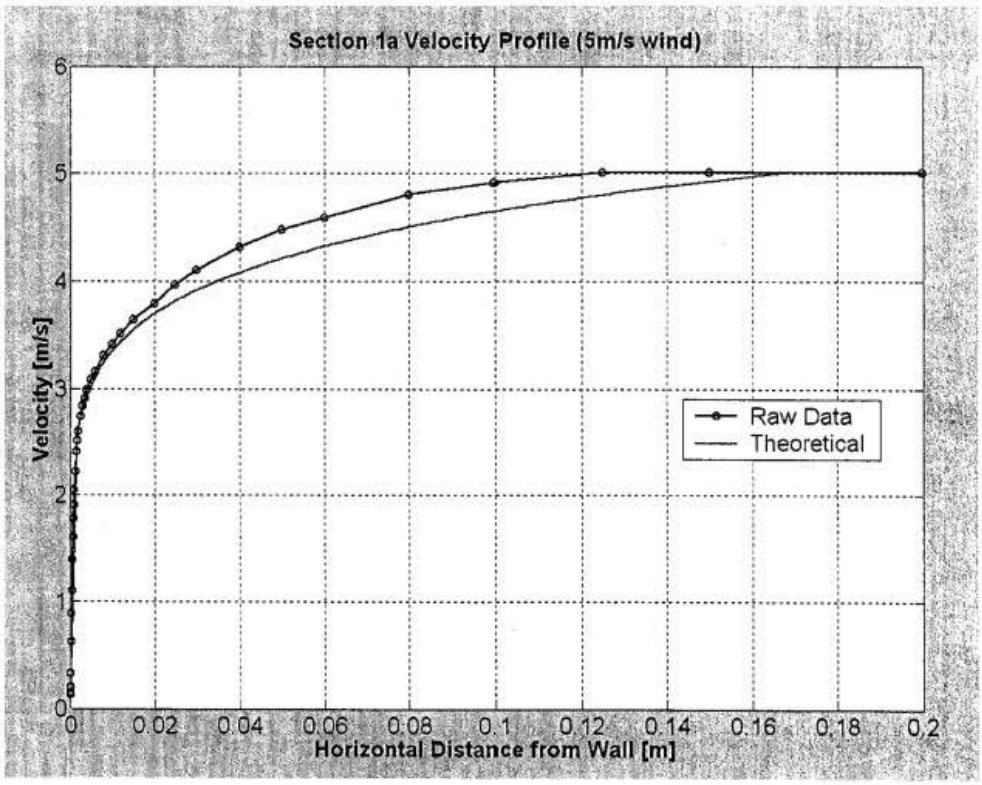

Figure 6-16. Station 1a Velocity Profile

Velocity Contours

The following figures illustrate the flow behaviour through the waterjet. The contours are shown with the waterjet rotated ninety degrees anticlockwise, that is, with the waterjet on

its side and the inlet facing the wall of the wind tunnel, as it was during the experiment. Figure 6-17 illustrates the orientation of the contour plots:

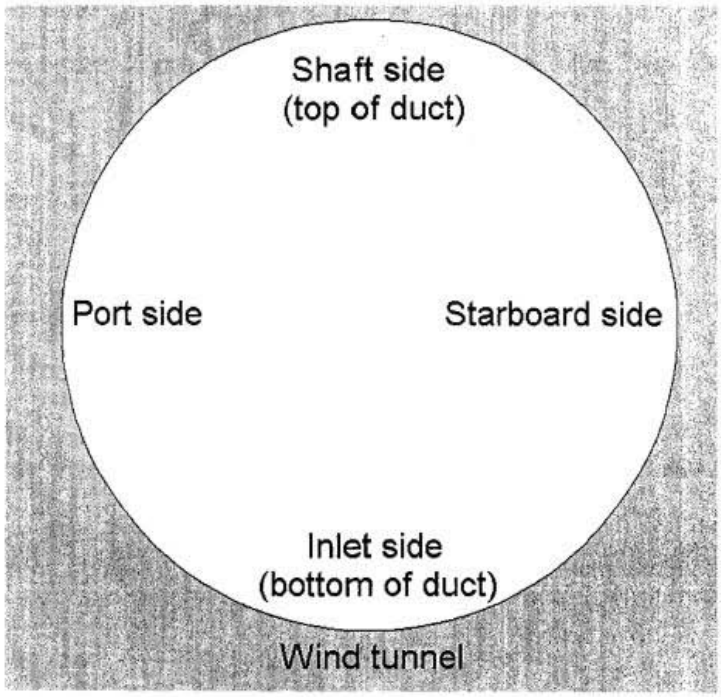

Figure 6-17. Contour plot orientation

Station 2 is located at the inlet throat and the contour plot, Figure 6-18, shows a high velocity concentration at the inlet side of the cross section (bottom). According to Verbeek et al. (1998), this is due to the boundary layer under the hull of the waterjet (wind tunnel wall). Their research showed that the uniform velocity in this boundary layer resulted in the entrainment of high-speed fluid at the bottom of the duct inlet, and low speed fluid at the top of the duct. The region of maximum velocity is slightly off-centre due to the swirling action of the impeller. At the top the cross section there is a

region of very low velocity. This is due to the presence of the shaft penetrating the cross section.

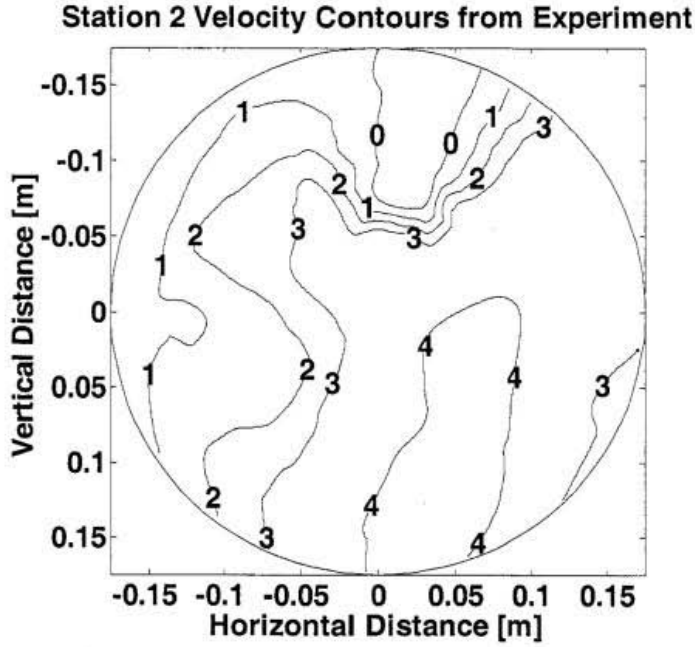

Figure 6-18. Station 2 Velocity Contour

Station 3 and station 5 are located at the pump face and pump exit, respectively. The influence of the impeller in these areas made it difficult to interpret the flow behaviour with a great deal of accuracy. This may be a consequence of the relationship between the sampling frequency and the frequency of the impeller, discussed previously. In order to obtain a more confident interpretation of the flow in this area more study is required. Such an investigation, however, is not the focus of this study and the statistical information provided by the cross-sections was assumed sufficient. This is one possible limitation of the physical model that could benefit from numerical investigation and the numerical simulation that forms the second part of this study provides a level of detail

sufficient for integration across these stations. The velocity contours for station 3 and station 5 are shown in Figure 6-19 and Figure 6-20, respectively.

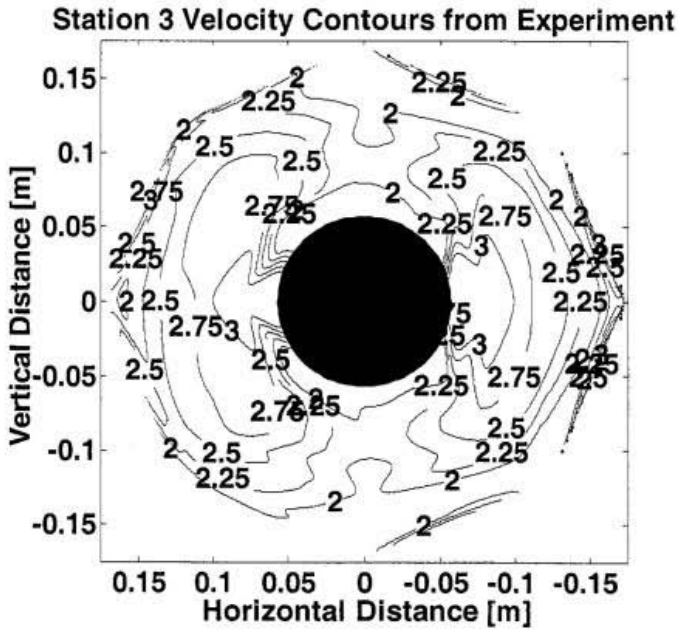

Figure 6-19. Station 3 Velocity Contour

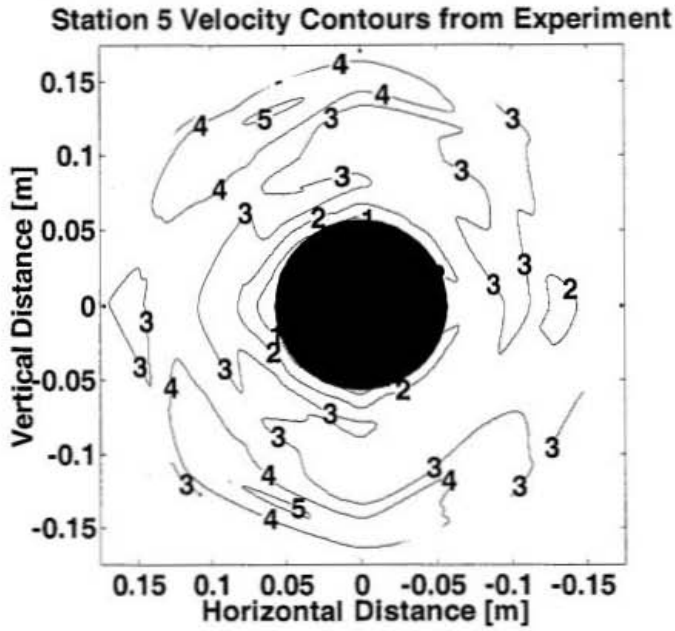

Figure 6-20. Station 5 Velocity Contour

Station 6 is located at the nozzle. As shown in Figure 6-21, the maximum velocity is much higher than at previous locations, since the diameter of the cross section is less than the diameter throughout most of the waterjet. Data was recorded outside the boundary of the nozzle purely for academic interest, as it was necessary to show that the flow was highly concentrated beyond the pump section.

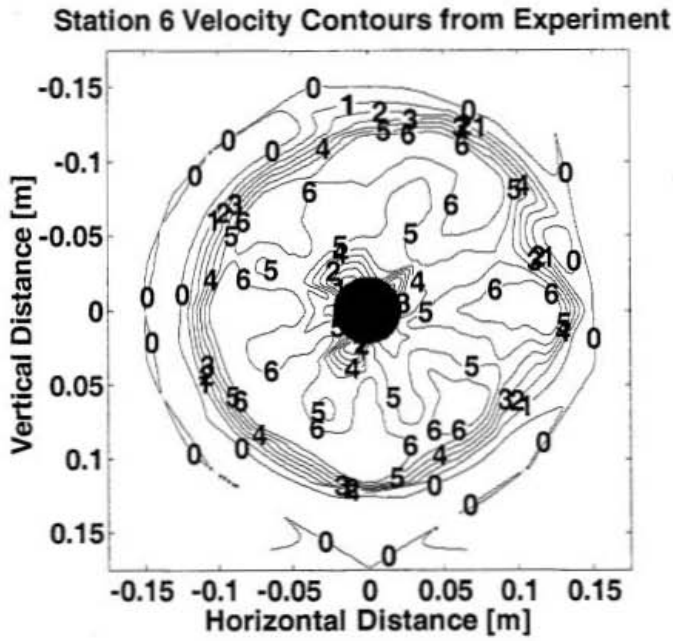

Figure 6-21. Station 6 Velocity Contour

Station 7 is located at the assumed vena contracta and shown in Figure 6-22. Although the diameter of the cross section was assumed to be less than that of station 6, data was recorded at many points in order to ensure that all of the necessary information was obtained. The exact limits of the cross section were calculated after the flowrate through the waterjet system was determined and the location of the vena contracta was acquired by CFD analysis. The information obtained at this station, however, was very valuable in the validation of the CFD simulation described in Chapter 8.

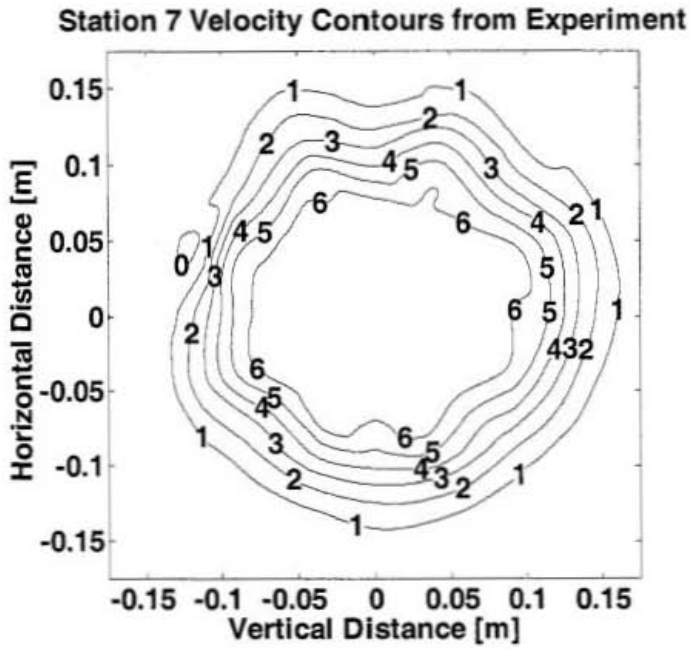

Figure 6-22. Station 7 Velocity Contour

The velocity data for stations 2,3,5 and 6 were averaged and divided by their respective cross sectional areas in order to obtain the volume flowrate through the waterjet system. The data, shown in Table 6-2, was then used to validate the numerical simulation described in the following chapter. As mentioned in Chapter 5, single wire CTA anemometers are limited to velocity measurements one direction. The inability of these probes to measure velocity direction contributes to the uncertainty in flow measurement and variation in flowrate throughout the waterjet. The effect is most significant in areas of high turbulence, such as near the impeller.

Table 6-2 . Volume Flowrate Through Waterjet

Station	Average Velocity [m/s]	Area [m^2]	Volume Flowrate [m^3/s]
2	2.93E+00	1.01E-01	2.97E-01
3	2.18E+00	1.01E-01	2.21E-01
5	2.75E+00	9.57E-02	2.63E-01
6	4.64E+00	4.70E-02	2.18E-01
Average Volume Flowrate			2.50E-01

6.4 Uncertainty of Hot-wire Measurements

The current ISO uncertainty model combines the uncertainty contributions from individual input variables into a total uncertainty at a given confidence level (Choi et al., 2003). The uncertainty of the results from CTA hot-wire measurements are therefore a combination of the uncertainties of the individually acquired voltages converted into velocity and the uncertainty of the statistical analysis of the velocity series (Jørgensen, 2002). The following section presents uncertainty considerations published by Dantec, a manufacturer of constant temperature anemometers.

The relative standard uncertainty is given by:

$$u(y_i) = \frac{1}{y_i} \cdot S \cdot \left(\frac{\Delta x_i}{k_i} \right) \qquad [6.8]$$

where,

x_i – input variable

y_i – output variable

S – sensitivity factor $\left(\frac{\partial y_i}{\partial x_i}\right)$

K_i – coverage factor related to the distributions of the input variance (Gaussian, rectangular, etc.)

Since most engineering applications are assumed to have Gaussian error distribution. The 95% confidence level normally required can be achieved through multiplication of the standard uncertainty with a coverage factor of 2, so that the total relative expanded uncertainty becomes:

$$U(tot)) = 2 \cdot \sqrt{\Sigma u(y_i)^2} \qquad [6.9]$$

The uncertainty associated with a velocity sample is a combination of the uncertainties of each component of the CTA system:

6.4.1 Anemometer

For commercially available anemometers, the uncertainty due to drift , noise and repeatability are negligible and do not contribute to the overall uncertainty in any significant manner, in comparison to other error sources. In addition, as long as the

frequencies associated with the flow are less than 50% of the cut off frequency, the frequencies of the flow do not contribute to the uncertainty. With respect to the present study, the sampling frequencies were chosen to accommodate this restriction and minimise the uncertainty.

At the impeller, however, the blade pass frequency is closer to the cut-off frequency, and the uncertainty of measurements near the pump is substantially larger.

6.4.2 Calibration and Conversion

Calibration generally comprises a major source of the uncertainty in a physical experiment. The uncertainty due to calibration equipment can be expressed as:

$$U(U_{cal}) = \frac{1}{100} \cdot STDV(U_{calibrator}(\%)) \qquad [6.10]$$

The uncertainty associated with the digital anemometer used for calibration is approximately 0.6% (Sutardi, 2002).

Linearisation uncertainty is related to curve fitting errors and is calculated from the standard deviation of the curve fitting errors in the calibration points $STDV(\Delta U_{lin})$:

$$U(U_{in}) = \frac{1}{100} \cdot STDV(\Delta U_{lin}(\%)) \qquad [6.11]$$

The standard uncertainty related to data acquisition is given by:

$$U(U_{res}) = \frac{1}{\sqrt{3}} \cdot \frac{1}{U} \cdot \frac{E_{AD}}{2^n} \cdot \frac{\partial U}{\partial E} \quad [6.12]$$

where E_{AD} is the input range of the data acquisition board, n is it's resolution in bits, U is the velocity and the final term is the slope of the inverse calibration curve.

6.4.3 Experimental Conditions

The alignment of the probe before and after calibration is referred to as the position uncertainty. The relative standard uncertainty associated with probe position is expressed as:

$$U(U_{pos}) = \frac{1}{\sqrt{3}} \cdot (1 - \cos\theta) \quad [6.13]$$

Probe position can normally be assumed to be $\Delta\theta = 1^{\circ}$.

The temperature variations that arise between calibration and experimentation give rise to systematic errors that, if not corrected, may contribute to uncertainty. The relative standard uncertainty is:

$$U(U_{temp}) = \frac{1}{\sqrt{3}} \cdot \frac{1}{U} \cdot \frac{1}{T_w - T_0} \cdot \left(\frac{A}{B} \cdot U^{-0.5} + 1 \right)^{0.5} \quad [6.14]$$

where

T_w – is the sensor temperature

T_0 – is the ambient reference temperature

ΔT – is the difference between the ambient reference temperature and the temperature

during calibration.

A,B – are constants that result from the power law calibration function

In addition, the velocity is representative of the mass flux, and any variations in density along with temperature will contribute to the uncertainty. In air, this gives the following:

$$U(U_{\rho,T}) = \frac{1}{\sqrt{3}} \cdot \Delta_{\rho,T} = \frac{1}{\sqrt{3}} \cdot \frac{\Delta T}{273} \qquad [6.15]$$

Ambient pressure fluctuations influence the density of the fluid medium, and hence the velocity that is calculated. The uncertainty is expressed as:

$$U(U_{\rho,P}) = \frac{1}{\sqrt{3}} \cdot \left(\frac{P_0}{P_0 + \Delta P} \right) \qquad [6.16]$$

Changes in humidity also contribute to uncertainty, as they alter gas composition. This uncertainty can be expressed as:

$$U(U_{hum}) = \frac{1}{\sqrt{3}} \cdot \frac{1}{U} \frac{\partial U}{\partial P_{wv}} \cdot \Delta P_{wv} \qquad [6.17]$$

In general, the influence of heat transfer per 1kPa change in water vapour pressure, P_{wv} is very small and can often be neglected.

The following table summarises the uncertainty associated with velocity samples obtained for the experiments of this study:

Table 6-3. Uncertainty for Hot-wire Anemometer

Source of uncertainty	Input variants	Input Value or typical value	Relative standard uncertainty
Calibrator	Δ_{ucal}	0.60%	0.006
Linearisation	Δ_{ufit}	0.50%	0.005
A/D resolution	E_{AD}	10 volts	0.0013
	n	12 bit	
Probe positioning	θ	1	0
Temperature variations1	ΔT	1 °C	0.008
Temperature variations2	ΔT	1 °C	0.002
Ambient pressure	ΔP	10 kPa	0.006
Humidity	ΔP_{wv}	1 kPa	0
Relative expanded uncertainty			3%

Additional uncertainties in the experiment include the uncertainty associated with the instrument used to measure shaft speed and the positioning of the hot-wire template. Great care was taken to ensure that the holes in the hot-wire template were positioned to directly coincide with co-ordinates within the station cross section. Some error, however, is inherent to the system, and is assumed to be on the order of 0.05 mm.

An additional uncertainty arises from the directional limitations of the hot-wire probe. The probe was assumed to be aligned with the axial flow, but through the course of testing the flow may or may not have been directed perpendicular to the sensor. This uncertainty was assumed to be 1%.

Furthermore, it was observed during preliminary testing that after considerable time (about an hour), the mean velocity of the air accelerated through the wind tunnel varied on the average of 0.3 m/s. The situation remained even after considerable warm-up time was given to the wind tunnel. A consequence of this was that the wind tunnel velocity had to be continually monitored during testing and required occasional adjusting. This

appears to be a problem with the wind tunnel fan and a mechanical uncertainty, therefore exists that may or may not be systematic. While an effort was made to ensure that the velocity of the air in the wind tunnel was kept at 5 m/s, a delay between the observed velocity fluctuation and a subsequent adjustment of the wind tunnel fan was inevitable. The mean velocity throughout the duration of each test was no doubt 5 m/s but further observation of the wind tunnel is required in order to understand the observed behaviour. The uncertainty in the mean wind tunnel velocity, however, was assumed to realised by the uncertainty in the calibration curve (linearisation), as a considerable amount of time was required for calibration before and after testing. Based on the uncertainty analysis, an overall uncertainty of 5% was assumed for the waterjet system.

The turbulence intensity throughout the system was similar to that observed during preliminary testing and an average turbulence intensity of 8% was calculated. The sampling rate and number of samples collected were therefore adequate for testing of the waterjet system.

The most important result that can be obtained from the experiment is the volumetric (or mass) flowrate. The parameter was used in conjunction with various point data to validate the numerical simulation discussed in the following section.

6.5 Summary

Various modifications to the original test platform were necessary in order to obtain a suitable testing apparatus. Improvements to the system stiffness resulted in much less

system vibration and noise, and an impeller built using rapid prototyping technology provided a more accurate representation of commercially available prototypes.

Wind velocity data was recorded at seven locations using a sampling rate of 35 samples per second and turbulence intensity was found be within the acceptable limits. The uncertainty associated with the velocity samples was determined according to ISO standards and was found to be on the order of 3%. When the additional factors that contributed to the uncertainty of the test were considered, a conservative estimate of 5% was appropriate for the overall experimental uncertainty.

The velocity profiles and contour plots of the data show that the system behaves as it is intended, with a concentrated jet stream at the nozzle exit and vena contracta. While the data collected is sufficient to assess the performance characteristics using the momentum flux method, a greater level of detail is possible through numerical simulation.

The numerical simulation, discussed in the following chapter was validated by the experimental observations and provides the researcher with an extremely useful tool for determining waterjet performance characteristics.

7 Introduction to Computational Fluid Dynamics

7.1 Introduction

Computational Fluid Dynamics (CFD) is concerned with obtaining numerical solutions to fluid flow problems using computer simulation. The techniques are multidisciplinary, and have been incorporated into the design of jet engines, internal combustion engines and drag characteristics of ships, to name a few.

More economical software and high performance computing hardware have led to recent advances in CFD analysis. These advances make CFD an attractive alternative to experimental-based analysis for several reasons:

- The cost of evaluating new designs is substantially lower
- It is possible to study systems where controlled experiments are difficult or impossible to perform
- The detail of results is practically unlimited

At present, the scarcity of qualified personnel, rather than the availability of suitable software and hardware limit the advancement of CFD analysis (Anderson, 1995).

7.2 The Elements of CFD code

CFD code is structured around numerical integration algorithms and all CFD codes are made up of three main elements: (1) a pre-processor, (2) a solver and, (3) a post-processor (Mason, 1998.)

7.2.1 The Pre-processor

The flow problem is input into the CFD code, transformed into suitable form, and passed onto the solver. This stage involves identifying the problem, defining the computational domain, and generating the grid. Nodes defined inside each cell determine the solution of the flow problem in terms of pressure, temperature, etc., and the number of cells inside a grid governs the accuracy of the solution. Grids are finer in areas of wide variation and coarser where little changes occur. The tuning of this grid is often the most time-consuming aspect of CFD analysis.

7.2.2 Solver

The model is set up in the solver and the solution is computed by numerical solution techniques such as finite element, finite volume, or spectral methods. The solution is then monitored until convergence is achieved through pre-defined criteria. The details of each solution technique are provided in section 7.4.

7.2.3 Post Processor

The post-processing field of computational fluid dynamics has benefited greatly from advances in computer graphics. Versatile data visualisation tools are common in most CFD packages and offer the user a variety of options for displaying solutions to CFD problems. These include streamlines, contour plots, particle tracking, 3D surface plots, and animation, to name a few. The overall flow pattern can be investigated in the post processor to see if key features of the system have been adequately resolved and if grid independence has been achieved (Fluent, 2001).

7.3 Grid Definition and Meshing

Mesh generation is the process by which a solution domain is discretized into a number of smaller, non-overlapping, geometrically simple elements. As over 50% of the time spent in industry on a CFD project is devoted to grid generation (Roache, 1998), the techniques used to define and refine the grid (or mesh) are constantly under improvement.

In general, since the solution to a flow problem is defined at nodes inside each cell (element), the larger the number of cells in a grid, the greater the solution accuracy. An overly fine mesh, however, can weigh heavily on computer resources and take an extremely long time to converge. The cost of a solution in terms of its necessary computer hardware and computational time is therefore a function of grid size, and a balance must exist between sufficiently accurate solutions and available computer resources. Meshes generally fall into two categories: structured and unstructured.

Structured meshes are ordered meshes made from a systematic system of node and element numbering related to the generation of the grid (Thornhill 2002). A benefit of structured meshes is that the connectivity does not need to be stored, and the computer memory requirements are reduced. Unfortunately, this type of mesh does not adapt well to complex geometries. While techniques have been developed whereby the domain is subdivided into a set of smaller, topographically simple sub-domains (multiblocking), the solver fails to efficiently resolve the interfaces between them. For complicated geometry,

then, structured meshes require separate structured grids that are mapped to the sub-domains, which increases computer resource requirements.

Unstructured meshes are an extreme case of the multiblock approach, where the blocks have become so small that they no longer require a local mesh. Elements, then, can be ordered in any fashion as long as they conform to the boundaries of the domain. Their connectivity, however, must be stored, along with details on the nodes that neighbour them. The advantage of unstructured meshes is that they can be used for complicated geometry and used in combination with any element type. This is known as hybrid meshing, and may be used to optimize a mesh through refinement in areas of large variation, and coarsening in areas of little change.

The software chosen for the simulation of this study was CFX 5.6®. The program has been used extensively in the analysis of jet flows, turbo machinery, and hull and wake analysis (CFX Update, 2002). CFX-5 solves the full system of hydrodynamic equations simultaneously with its coupled multigrid solver and has proven to be a reliable, robust, and fast engineering tool.

CFX is capable of performing analyses on a variety of three-dimensional element shapes including prismatic, pyramidal, and hexahedral. Three meshing modes are available:

1. Advanced Front and Inflation
2. Patran Volume Meshing
3. Paving and IsoMeshing

The Advanced Front and Inflation (AFI) method produces a triangular surface mesh using either Delaunay or Advancing Front surface meshing (CFX- Pre, 2003). The volume mesh generated contains tetrahedral elements, along with prismatic and pyramidal elements if inflation is used. Inflation produces a computationally efficient mesh near the boundaries through a series of prismatic volume elements grown from pyramidal elements at the surface. This is useful for resolving the mesh near the wall boundary, where velocity gradients are large normal to the surface and small parallel to it. The AFI mesher works by manipulating a previously defined three-dimensional region where the 'front' of triangular elements generated by the surface mesher are transformed into a volume mesh. This is the default meshing mode in CFX, and is generally adequate for most engineering problems.

Patran Volume meshing produces many different element types from a triangular or quadrilateral surface mesh. With this method, a separate, neutral file is created and exported into CFX.

Paving and IsoMeshing produces a triangular surface mesh from unstructured or structured surface meshes. It is not recommended since the capabilities of the AFI mode exceed the capabilities of this mode (CFX – Pre, 2003).

The two aspects that characterise a successful CFD simulation are convergence of the iterative process and grid independence. Convergence considerations are discussed in (7.5), and this section will conclude with a discussion of grid independence. Good initial grid design is the result of careful analysis and insight into the expected properties of the flow. In order to eliminate errors associated with the grid coarseness, a grid dependence

study must be performed. This is a process of successive refinement of the grid until certain key results do not change (Veersteeg & Malalasekera, 1995), and is an integral part of all high quality CFD studies.

7.4 Solution Methods

Finite difference method

Finite difference is the oldest numerical method to obtain approximate solutions to differential equations. The unknowns of a problem (ϕ) are described by point samples at the node points of a grid of co-ordinate lines. Truncated Taylor series expansions are used to generate finite difference approximations of derivatives of ϕ. Disadvantages of the method are that it requires a Cartesian grid, and that discretization errors can lead to violation of conservation laws (Thornhill 2003).

Finite Element method

The finite element method was first developed in the 1950s for analysing aircraft structures. Simple piecewise functions on elements are used to describe the local variations of the unknowns. The piecewise approximations are substituted into the governing equations and the residuals are minimised by multiplying them by a weighting factor, and integrating. A set of algebraic equations for the unknown coefficients of the approximating functions is then obtained.

Spectral Methods

The unknowns are approximated by truncated Fourier series polynomials. These approximations are not local as in the finite element approach, and are valid throughout the computational domain. Algebraic equations for the Fourier series are provided by a weighting residuals concept similar to that of the finite element method.

The Finite Volume Method

The most well established and thoroughly validated technique; finite volume methods were developed in order to overcome the drawbacks of the finite difference method. The numerical algorithm consists of formal integration of the conservation of mass laws over all of the finite control volumes of the solution domain and discretizing them such that velocity, pressure and temperature can be calculated (LeVeque, 2002). The terms in the integrated equation that represent flow processes such as convection, diffusion, and sources, are replaced by a variety of approximations similar to those used in the finite difference method. The integral equations can then be converted into a system of algebraic equations that can be solved by the iterative method.

Control volume integration distinguishes the finite volume method from all others, and the basic quantities of mass and momentum are conserved at the discrete level. This is the main advantage of the finite volume method. For conservation of a general flow variable (ϕ) within a finite control volume, a balance must exist between the processes that tend to increase or decrease it. In words (Atkins, 2003):

Rate of change of ϕ in the control volumw with respect to time	=	Net flux of ϕ from convection into control volume	+	Net flux of ϕ from diffusion into control volume	+	net rate of creation of ϕ inside control volume

Convection refers to transport due to fluid flow, diffusion refers to transport due to variations of ϕ from point to point, and source terms are associated with the creation or destruction of ϕ.

An iterative approach is required to solve the non-linear behaviour demonstrated by the transport equations and the most popular solution procedures are the TDMA line-by-line solver of the algebraic equations, coupled with the SIMPLE algorithm to ensure correct linkage between pressure and velocity (Thornhill, 2002).

7.5 Problem solving using CFD

Typical decisions that have to be made by the CFD user include whether to model the problem in two or three dimensions, exclude the effects of ambient temperature or pressure variations on the density of air or to solve the turbulent flow equations.

Three concepts useful in determining the success or failure of a mathematical algorithm are convergence, consistency, and stability.

- Convergence is the property of a method to approach the exact solution as grid spacing, control volume size or element size is reduced to zero.
- Consistency is the ability of a numerical system to demonstrate equivalency with the original governing equations, as grid spacing tends to zero.
- Stability is associated with the damping of errors as the numerical method proceeds. If the technique is not stable, then wild oscillations or even divergence can result.

Establishing convergence by reducing the mesh spacing to zero is extremely difficult and time consuming so alternative methods have been developed to arrive at the same conclusion. These are known as robust methods and are highlighted by the concepts of conservativeness, boundedness, and transportiveness (Veersteeg & Malalasekera, 1995).

- Conservativeness ensures fluid property ϕ is locally conserved on each control volume. This, in turn, ensures global conservation for the entire domain.
- Boundedness is similar to stability and requires that a linear problem (without sources) be bounded by the maximum and minimum values of a flow variable. Although flow problems are non-linear, it is nonetheless important to study the behaviour of closely related linear problems.
- Transportiveness accounts for the directionality of influencing (in terms of the relative strength of diffusion vs. convection). Diffusive phenomena indicate that a change in one property (temperature, for example) affects the property in equal measure in all directions. Convective phenomena indicate that the influencing exists exclusively in the flow direction, such that a point will only experience effects due to changes at upstream locations.

Robust methods have been incorporated into all finite volume schemes and have been widely shown to lead to successful CFD simulations. It should be stressed that good CFD simulation is the result of a strong grid, and informed decisions regarding the expected properties of the flow. It is a powerful problem-solving tool that can be validated through experimentation.

CFX is a general purpose CFD code that uses the finite volume method exclusively. Within the solver, however, there are many parameters that may be specified depending on the problem specifics and flow conditions. The following sections describe the details of the CFX solver, and optimization techniques that may be employed to arrive at a converged CFD solution.

7.5.1 Numerical Discretization of the Finite Volume Method

The general transport equation can be written in the following form:

$$\frac{\partial(\rho\varphi)}{\partial t} + div(\rho\varphi\vec{u}) = div(\Gamma grad\varphi) + S_{\varphi} \qquad [7.1]$$

The left side is described by the rate of change term and the convective term. The diffusive term (Γ=diffusion coefficient) and the source term are described by the right side of the equation. Integration of the transport equation over a three-dimensional control volume is the key step of the finite volume method:

$$\int_{CV} \frac{\partial(\rho\varphi)}{\partial t} dV + \int_{CV} div(\rho\varphi\vec{u}) dV = \int_{CV} div(\Gamma grad\varphi) dV + \int_{CV} S_{\varphi} dV \qquad [7.2]$$

The Gauss divergence theorem is used to transform volume integrals into surface integrals (Acheson, 1998):

$$\int_{V} \nabla \cdot (\vec{a}) dV = \int_{A} (\vec{a}) \cdot n dA \qquad [7.3]$$

The theorem is used to re-write the convective and diffusive terms as integrals over the entire bounding surface. Note that $n \cdot a$ is the component of vector a in the direction of

the vector n normal to the surface element da

$$\frac{d}{dt}\int_{CV}\rho\varphi dV+\int_{A}n\cdot(\rho\varphi\vec{u})dA=\int_{A}n\cdot(\Gamma grad\varphi)dA+\int_{CV}S_{\varphi}dV \qquad [7.4]$$

The volume integrals represent source or accumulation terms, while the surface integrals represent the integration of flux terms. In all but a few special cases, these equations cannot be analysed analytically, and must be replaced by algebraic approximations and solved using a numerical method.

7.5.2 Segregated and Coupled Solvers

Once the equations are discretized, techniques must be identified for solving them. Segregated methods solve the discretized equations individually, check for convergence, and iterate stepwise through all of the equations until convergence is achieved (Thornhill, 2002). The momentum equations are first solved using an assumed pressure, and an equation for the corrected pressure is obtained. This procedure, known as the 'guess and correct method' leads to a large number of iterations, and relaxation parameters must be carefully selected for each of the variables in the equation.

Coupled methods, on the other hand, solve the dynamic equations as a single system and uses a fully implicit discretization of the equations at any given time step (CFX Solver Theory, 2002). For steady-state problems, the time step parameter can be used to accelerate the solution and reduce the number of iterations required before convergence is achieved.

CFX uses a coupled solver by default, because it is faster than the traditional segregated solver and less iteration is required to achieve convergence. In addition, a coupled treatment of the discretized equations is more robust, efficient, and simple, than a segregated approach. The method is equally applicable to structured and unstructured meshes, while a potential drawback of the coupled solver is that more storage is needed for all of the unknown coefficients.

Advection Schemes

Convection and diffusion play an important role in CFD simulation. It is important to account for the fact that diffusion spreads its influence in all directions, while convection is segregated to the direction of flow. The main difficulty with discretizing the convection terms is in the calculation of the transported value (ϕ) at the control volume faces and the convection flux across its boundaries (Patankar, 1995). An important feature of a discretization scheme, therefore, is its ability to account for convection and diffusion at each control volume. The advection term is discretized in CFX according to the following function:

$$\phi_{ip} = \phi_{up} + \beta \nabla \phi \cdot \Delta \vec{r} \qquad [7.5]$$

where,

ϕ_{ip} -value of the ϕ at the integration point of interest

ϕ_{up} - value of the upwind node

$\nabla\phi$ - gradient of ϕ

$\vec{r}$ - vector from the upwind node to *ip*

β - choices for β give rise to different advection schemes

Several discretization schemes have been developed and include:

- Central differencing – the value of a node is found from the average value of the nodes surrounding it. The method is second-order accurate, but can suffer from decoupling issues and produce solutions that oscillate about an exact solution. The method is generally only valid for Large Eddy Simulations (LES).
- 1st order upwind differencing – the convected value of a node is taken to be equal to the value at the upstream node (flow direction is considered). The method is numerically stable and does not introduce the same oscillation problems inherent to the central differencing scheme. A major drawback of this method is that erroneous results are produced when the grid is not aligned with the flow. The scheme causes the transported properties to smear, and is referred to as false diffusion. The method is not recommended to obtain final results.
- Numerical Advection Correction Scheme (Specify Blend) – the diffusive properties of the upwind differencing scheme are reduced by introducing a numerical advection correction, which is essentially an anti-diffusive flux added to the upwind scheme (CFX Solver Theory, 2002). The method is less numerically stable than the upwind differencing scheme, and may introduce some

oscillation about the exact solution. The method is suitable for obtaining final results, but is less robust than the high resolution scheme.

- High Resolution Scheme – based on the work of Bath and Jesperson (1989), the method calculates β close to second order accuracy without violating boundedness principles. The blend factor is varied throughout the domain based on the local solution field in order to enforce the boundedness criteria. The method reduces first order near-discontinuities and variation in the free stream and is recommended for obtaining final solutions.

7.5.3 Pressure-Velocity Coupling

The treatment of pressure by the equations used in the finite volume method needs special consideration. The transport equations for each velocity component in a flow (the momentum equations) contain pressure gradient terms that cannot be expressed in terms of velocity. If the pressure gradient is known, the process of solving the discretized equations is similar to the schemes already described. In general, however, the pressure field is not known beforehand, and it is something to be determined as part of the solution.

In compressible flows, the continuity and energy equations can be used as transport equations for density, and temperature, respectively, and pressure can be determined from the equation of state $p = p(\rho,T)$. For incompressible flows, however, the density is constant and not linked to the pressure and there is a coupling between the pressure and velocity. The result is that a pressure equation must be derived as a constraint on the

solutions of the Navier-Stokes equation to satisfy continuity. If the correct pressure field is applied in the momentum equations, the resulting velocity field should satisfy continuity (Anderson, 1995).

Several algorithms have been developed to overcome this problem:

- SIMPLE – Semi-Implicit Method for Pressure Limited Equations. This is a guess and correct procedure, where solution fields are generated from the momentum and continuity equations and iterated until there is convergence of the velocity and pressure fields. The method is suitable for correcting velocities, but not adequate for determining pressure.
- SIMPLER – Simple Revised. Similar to the SIMPLE method, but a discretized equation for pressure is used instead of a pressure correction. Originally developed to overcome the shortcomings of SIMPLE, the method has proven to increase solver performance.
- SIMPLEC – SIMPLE Consistent. Follows the same steps as the SIMPLE method, but the less important terms are omitted from the velocity correction.
- PISO – Pressure Implicity with Splitting of Operators. Uses a single predictor step and two corrector steps per iteration. The method may be regarded as an extension of SIMPLE with a further corrector step to enhance it.

When pressure and velocity are stored at the same location in a grid they are said to be collocated. Collocated grids give rise to a decoupling of odd-pressure nodes from the

even pressure nodes. This 'checker-board' pattern leads to indeterminate oscillations of the pressure field. Two common solutions to this problem are:

1. Store the pressure and velocity at different locations using a staggered grid
2. Use a collocated grid but modify the traditional interpolation formula

The SIMPLE algorithm and its derivatives employ a staggered grid to overcome this problem. The staggered grid arrangement stores velocity components halfway between the pressure nodes and results in a different set of control volumes. The advantages of this technique are :(1) pressure is stored at the points required to compute force, and no interpolation is required and (2) velocity components are stored at the points required to establish mass conservation. The disadvantages of the technique are: (1) added geometric complexity and (2) velocity nodes may cease to exist halfway between pressure nodes in non-cartesian meshes.

A collocated grid may also be used in conjunction with Rhie and Chow interpolation (Rhie and Chow, 1982). The idea is to interpolate the relationship between the cell-centre velocity and pressure nodes at either side of it, rather than interpolating the velocity components directly. The Rhie-Chow method, then, is equivalent to adding a pressure-diffusion term. For non-cartesian meshes, methods similar to this are the norm, and most general-purpose CFD codes use the collocated arrangement.

CFX uses a single cell, unstaggered, collocated grid to overcome the problems related to pressure and velocity coupling. The method is similar to that used by Rhie and Chow,

with some modifications to improve robustness of the discretization when the pressure varies rapidly.

7.5.4 Multigrid Methods

A set of discretized equations does not always necessarily lead to a converged solution. As the size of the mesh increases, or element aspect ratios become larger, the performance of many iterative solution techniques decreases (Shaw, 1992). For a given mesh size, these techniques are only efficient at reducing errors which have a wavelength on the order of the mesh spacing. For this reason, longer wavelength errors take an extremely long time to dissipate.

The convergence behaviour of traditional matrix solvers can be improved using multigrid methods. The process involves performing iterations on progressively coarser, virtual, meshes and adapting the results to the original fine mesh. Longer wavelength errors, then, appear as shorter wavelength errors relative to the mesh spacing. The algebraic multigrid technique permits the meshing of problem geometry without using different mesh spacings. This is accomplished by summing the fine mesh equations to form a system of discrete equations for a coarse mesh. CFX uses an implementation of the algebraic multigrid technique called Additive Correction, where the conserved quantities over a finite control volume are described by the discrete equations.

7.6 Boundary Conditions

The equations of fluid flow in a CFD problem are closed (numerically) by the specification of boundary conditions. CFD packages offer a variety of possible boundary

conditions to suit a particular application and in order to correctly define the flow simulation, boundary conditions must be applied to the regions at the outer extremity of the computational domain. The boundary conditions relevant to this discussion are:

- Inlet
- Outlet
- Opening
- Wall
- Interface

The inlet boundary condition is used where flow is directed into the domain. It can be specified in terms of mass and momentum, turbulence intensity, heat transfer and thermal radiation. The velocity at the inlet can be defined by its normal speed, mass flow rate, static pressure, total pressure, or individual velocity components.

Where it is known that flow is directed out of the domain, an outlet boundary condition is used. The bounding static pressure, velocity or mass flow can be specified at an outlet, but all other variables are part of the solution.

An opening boundary is used when there may be possible inflow and outflow at a single location. The condition is useful when some of the boundary condition details are known, but the flow is not restricted in or out of the domain.

Solid impermeable boundaries to the flow are identified by wall boundary conditions. They are the default setting in CFX for fluid-world and solid-world regions that have not

been otherwise specified. For viscous flows, the no-slip condition is automatically imposed at a wall.

Fluid-Fluid Interface – domain interfaces are used to connect meshes together or allow a change in the reference frame between mesh regions. Meshes for complex regions can then be generated in modular components and connected together. The method is useful for reducing the effort spent in mesh generation, as it is much simpler to generate a series of domains and connect them later, than it is to generate a single mesh for the entire domain.

The importance of well-posed boundary conditions cannot be overemphasized, as it is this area that causes most simulations to fail or converge (Shaw, 1992). Over or under-specification of a problem can result in solutions that fail to converge or are otherwise physically impossible. If the conditions specified in the CFD simulation can be physically recreated in a laboratory setting, the boundary conditions are generally well posed. Furthermore, certain configurations may be physically valid, but do not produce converged solutions because they fail to impose a strong constraint on the system. In CFX, the most robust configuration of boundary conditions consists of velocity or mass flow at an inlet, static pressure at an outlet and the inlet total pressure is an implicit result of the prediction. Conversely, because the total inlet pressure and mass flow are both an implicit result of the prediction, a static pressure condition at the inlet, and static pressure at the outlet would be very unreliable.

7.7 Turbulence

At values below the so-called critical Reynolds number, Re_{crit}, flow is smooth and adjacent layers of fluid flow past one another in a somewhat orderly manner. This is known as laminar flow (Munson et al., 1998). At Reynolds numbers greater than Re_{crit}, the flow behaviour is random and chaotic, and deserving of the name turbulent flow.

A full description of turbulent flows at realistic Reynolds numbers would require an extremely dense mesh and computing power many orders of magnitude greater high than is available in the foreseeable future (CFX Solver Theory, 2002). To account for the effects of turbulence in a practical manner, turbulence models have been developed that estimate the turbulent flow characteristics without resorting to prohibitively fine mesh densities. Reynolds (1895) proposed that for large time scales, turbulent flow could be decomposed into mean and fluctuating components. The unsteady Navier-Stokes equations, then, can be modified by the introduction of steady and fluctuating components for velocity and pressure. The Reynolds-Averaged Navier Stokes (RANS) equations that result form the basis for many practical engineering calculations involving turbulence.

The Navier Stokes equation for linear momentum is given by:

$$\frac{\partial u_i}{\partial t} + u_j \frac{\partial u_i}{\partial x_j} = -\frac{\partial p}{\partial x_i} + \nu \nabla^2 u_i \qquad [7.6]$$

The velocity is written in terms of an average component, $\overline{u}_i$, and a time varying

component u_i':

$$u_i = \overline{u}_i + u_i' \qquad [7.7]$$

Similarly for pressure,

$$p = \overline{p} + p' \qquad [7.8]$$

Substituting the decomposed variables into the Navier Stokes equations produces the familiar RANS equation

$$\frac{\partial \overline{u}_i}{\partial t} + \overline{u}_j \frac{\partial \overline{u}_i}{\partial x_i} = -\frac{\partial \overline{p}}{\partial x_i} + \nu \nabla^2 \overline{u}_i - \frac{\partial \tau_{ij}}{\partial x_j} \qquad [7.9]$$

where,

$\tau_{ij} = \overline{u_i' u_j'}$ is the Reynolds stress tensor

The averaging procedure introduces additional unknown terms in the Navier-Stokes equations, which can be seen as supplementary stresses in the fluid. In order to achieve closure of the equations, where the number of equations is sufficient to satisfy the unknowns, the Reynolds stresses must be modelled by additional equations. The equations used to close the system define the type of turbulence model used (Wilcox 2000).

Turbulent flow models are not intended to provide details on turbulent structures. Rather, there are used to estimate average values such as velocity, pressure, and turbulence intensity. The ability of a turbulence model to accomplish this task accurately depends on the model being used.

One approach for obtaining closure of the RANS equation is to assume that the Reynolds stress behaves like a Newtonian fluid viscous stress. As such, it is written as follows:

$$\tau_{ij} \equiv \mu_T \frac{\partial u_i}{\partial x_j} \qquad [7.10]$$

where,

μ_T – eddy (turbulent) viscosity

Eddy viscosity models are the most common means of handling turbulence in fluid simulations. With this method, the unknown eddy viscosity term is replace by a single function, or several functions of velocity and pressure. Dimensional analysis shows that the eddy viscosity is related to the ratio of the turbulent length scale divided by the turbulent time scale. Eddy viscosity models are classified according to the complexity with which the scales are modeled. Some of the turbulence models available in CFX are:

Zero Equation model

With this model, both the length and time scale are expressed as algebraic functions where the constants come from physical experiments. This model is simple to use and produces approximate results very quickly, but is only suitable as an initial guess for more advanced models. The method should not be used to obtain final results.

k-ε Model (Second Equation)

The k-ε model uses the transport equations for turbulent kinetic energy (k) and turbulent dissipation (ε) to define the eddy viscosity. This model has been implemented into most

general-purpose CFD codes and is the most common turbulence model used. It has proven to be stable and numerically robust and is suitable for obtaining final solutions for general fluid flows. The model is not recommended, however, for flows with boundary layer separation, sudden changes in mean strain rate, or rotating fluids (CFX Solver Modelling, 2002).

RNG k-ε Model

Created as an alternative to the standard k-ε model, it is more applicable to a wider range of flows including rapidly straining and swirling flows (Thornhill 2002). In general, it offers little improvement to the standard model.

Reynolds Stress Model (RSM)

The Reynolds Stress model uses the transport equations for the Reynolds stresses, together with an equation for the dissipation rate to achieve closure of the RANS equation. The model is more appropriate for rotating flows, or those with sudden changes in strain, but in most cases the results are no better than those produced with the simpler models.

Shear Stress Transport Model (SST)

When an adverse pressure gradient is present, the standard two-equation model fails to predict the onset of flow separation correctly. Under certain applications, such as flow separation over a wing, more advanced modelling techniques are required. In these circumstances, or when high accuracy boundary layer simulations are required the Shear Stress Transport (SST) model may be appropriate.

Large Eddy Simulation (LES)

In situations where the usual approach to predicting turbulent flows is not adequate, or when details on the structure of turbulent flows are required, Large Eddy Simulation or Direct Numerical Simulation (DNS) may be appropriate. The LES approach filters very fine time and length scales in order to solve time dependent equations and requires a fine grid and small time steps. The DNS approach solves the time-dependent equations with no approximations and resolves all relevant scales. These approaches, however, are very time consuming and not recommended for wall-bounded flows due to the high-resolution requirements and computing times. At present, true predictions of turbulent flows can only be accomplished for a few simple cases, and require days and possibly weeks to converge using 8 to 16 processors (CFX Solver Modelling, 2002).

7.8 The Application of CFD

Computational Fluid Dynamics is the process of replacing the differential equations that govern fluid flow with a set of algebraic equations that can be solved with the aid of a computer to get an approximate solution. The accuracy of the final results can only be validated by comparison with experimental work, of similar scope, and may involve a matrix of point flow measurements with hot-wire or laser Doppler anemometry. With a level of detail that was not possible prior to the onset of numerical simulation, the CFD user must be cognoscente of the limitations and relevant applications of computational fluid dynamics. CFD is intended as a tool for improved understanding of the behaviour of

a fluid system, and in it's present state, serves to supplement experimental work. Hastings (1985) took a rightly cautionary approach to numerical simulation:

> "The purpose of computing is insight not numbers" (1985)

When sufficient data is available to endorse the numerical simulation, CFD analysis may be used to further the level of detail in an experiment, or measure aspects of an experiment that are restricted by physical barriers or limitations.

An example of such a problem is the analysis of the flow through a waterjet. Near the inlet, for example, it is difficult in many cases to accurately measure the velocity profile of fluid entering the waterjet using hot-wire anemometry or laser Doppler anemometry. An accurate CFD simulation of the flow through this section could provide the necessary information. Also, point measurements at sections throughout the waterjet system are useful, but in order to obtain a complete description of the behaviour, an exhaustive number of samples are necessary. A CFD simulation that has been validated by a reasonable number of point measurements can then be used to provide insight at a much finer resolution. Integration of measured quantities, for example, would benefit from thousands of point measurements that would prove impossible to measure and collect using conventional methods.

The current research focuses on such a problem. Experimental data is presented for a waterjet unit attached to a wind tunnel, and CFD simulation is used to provide insight into the behaviour of the system. The following chapters describe the experimental work,

the development of a numerical simulation, and the analysis of the results that follow using the momentum flux method proposed by Kruppa (1996).

8 Numerical Simulation

The information obtained from physical testing of the waterjet system formed the foundation of the numerical simulations. The following chapter describes the development of the numerical model, a description of the simulation parameters, and finally, the application of the results using the momentum flux method.

8.1 A Mathematical Description of the Waterjet - The Boundary-Value Problem

In order to illustrate the complexity of the numerical simulation, the following is a mathematical description of the waterjet system. Great strides in CFD have made it possible for researchers to analyse such systems in a manner that would have proven impossible less than a decade earlier. Consider an impeller rotating with constant speed, n, within an asymmetrical cylindrical duct. The jet speed at the inlet V_i is assumed uniform, and can be determined according to the ratio of the total flux into the duct Q_i and the area of the inlet A_i.

$$V_i = \frac{Q_i}{A_i} \qquad [8.1]$$

The jet speed at the outlet is also assumed uniform, and is defined by the ratio of the jet flux and the area of the outlet, A_j.

$$V_j = \frac{V_i A_i}{A_j} \qquad [8.2]$$

8.1.1 Governing Equations

The Navier-Stokes equations provide a complete mathematical description of the flow of incompressible Newtonian fluids. They are an expression of the conservation of momentum coupled with the conservation of mass, or continuity [8.4]:

$$\rho \frac{D\vec{u}}{Dt} = -\nabla p + \rho \vec{g} + \mu \nabla^2 \vec{u} \qquad [8.3]$$

$$\nabla \cdot \vec{u} = 0 \qquad [8.4]$$

where,

ρ - fluid density

p – pressure

μ – dynamic viscosity

t – time

$\vec{g}$ – acceleration due to gravity

$\vec{u}$ – fluid velocity

These equations, except for a few simple cases, have no analytical solutions. It is often possible, however, to obtain analytical solutions to the equations that result from some useful assumptions. If the fluid is assumed inviscid (μ=0), the Navier Stokes equations are reduced to the Euler equations:

$$\rho \frac{D\vec{u}}{Dt} = -\nabla p + \rho \vec{g} \qquad [8.5]$$

For flows involving a very thin boundary layer, the forces acting on the fluid can be determined using [8.5] and the continuity equation. Although the Euler equations are considerably simpler than the full Navier-Stokes equations, they are still not amenable to a general analytical solution that allows one to obtain the pressure and velocity of all points in the flow field. The main source of the difficulty lies in determining solutions to the non-linear velocity terms that arise from the material derivative of velocity. The analysis of inviscid flow problems can be further simplified by assuming that the flow is irrotational. This is a valid approximation for real flows except in the boundary layer and near wakes (where viscous forces dominate).

An irrotational flow field is one for which the vorticity, ω, is zero (Acheson, 1998). The vorticity acts as a measure of the local rotation of fluid elements and is defined as a vector that is twice the rotation vector:

$$\omega = \nabla \times \vec{u} \qquad [8.6]$$

For irrotational flows, then, equation [8.6], along with the continuity equation [8.4], are all that must be satisfied:

$$\nabla \times \vec{u} = 0 \qquad [8.7]$$

$$\nabla \cdot \vec{u} = 0 \qquad [8.8]$$

Equation [8.7] is then expanded to show the following relationships:

$$\frac{\partial v}{\partial x} = \frac{\partial u}{\partial y} \qquad [8.9]$$

$$\frac{\partial w}{\partial y} = \frac{\partial v}{\partial z} \qquad [8.10]$$

$$\frac{\partial u}{\partial z} = \frac{\partial w}{\partial x} \qquad [8.11]$$

The velocity components for irrotational flows can be expressed in terms of a scalar function $\phi(x,y,z,t)$ such that:

$$u = \frac{\partial \phi}{\partial x}$$
$$v = \frac{\partial \phi}{\partial y} \qquad [8.12]$$
$$w = \frac{\partial \phi}{\partial z}$$

Direct substitution of these expressions into the velocity components in equation [8.9], [8.10], and [8.11] verify that the velocity field defined by [8.12] is irrotational. Equation [8.12] can then be written as the gradient of the scalar functionϕ:

$$\vec{u} = \nabla \phi \qquad [8.13]$$

Substituting [8.13] into the conservation of mass equation, [8.4], reveals the Laplace equation:

$$\nabla^2 \phi = 0 \qquad [8.14]$$

Inviscid, incompressible, and irrotational flows are commonly referred to as potential flows, and are governed by Laplace's equation.

It can often be assumed that the impeller and stators are operating in an inviscid, irrotational, and incompressible fluid, and viscous effects on the impeller and stator blades (and the trailing vortex sheets) are confined within an infinitesimally thin boundary layer. The Laplace equation, therefore often applies.

A Cartesian coordinate system was chosen for the impeller shown in Figure 8-1. The x-axis, defined positive upstream, coincides with the shaft centreline, while the y-axis is

positive upwards, and the z-axis completes the coordinate system according to the right-hand rule. In addition to the Cartesian system, a cylindrical coordinate system was defined by the radius r and positive counter-clockwise angle θ, looking downstream.

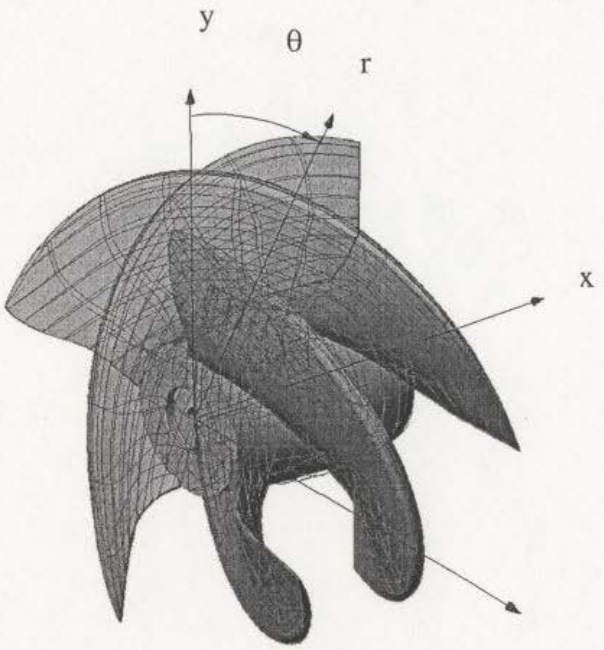

Figure 8-1. Impeller Coordinate System

8.1.2 Boundary Conditions

To complete the mathematical description of the waterjet system, the boundary conditions must be specified. The motion of the flow described by the Laplace equation is subject to the boundary conditions illustrated in Figure 8-2.

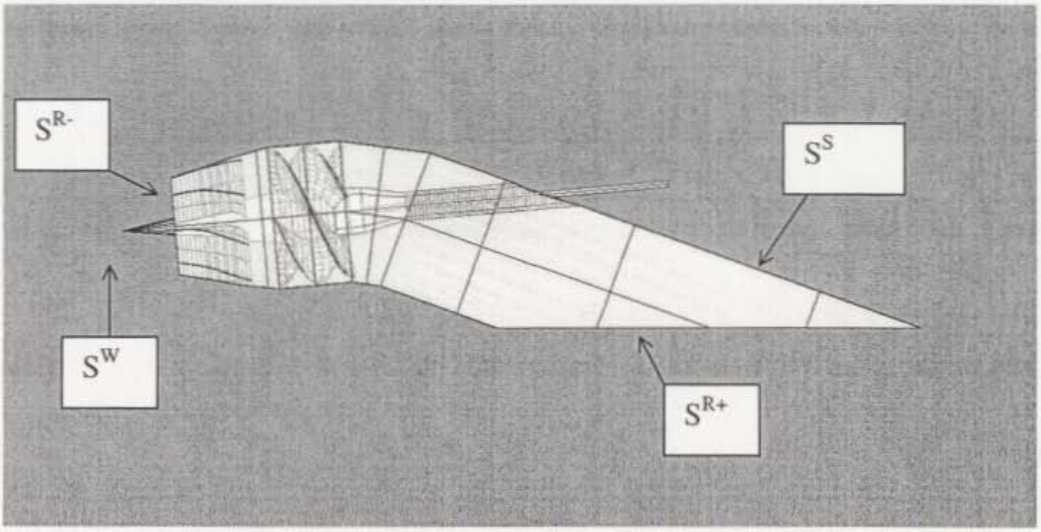

Figure 8-2. Waterjet Boundary Conditions

1. Kinematic Boundary Condition on the solid surface (S^S) that consists of the impeller, stator, and duct surfaces:

$$\hat{n} \cdot \vec{V} = \hat{n} \cdot \vec{U}_r + \frac{\partial \phi}{\partial n} = 0 \qquad [8.15]$$

where:

$\vec{V}$ is the total velocity

$\hat{n}$ is the unit vector normal to the solid surface (positive inward)

$\vec{U}_r(r,\theta)$ is the flow at point (r,θ) that may be expressed in terms of the oncoming velocity $\vec{V}_s$ and the rotational velocity $\vec{\Omega}$:

For impeller:

$$\vec{U}_r(r) = \vec{V}_s(r) - \vec{\Omega} \times \vec{x} \qquad [8.16]$$

For stators:

$$\vec{U}_r(r) = \vec{V}_s(r) \qquad [8.17]$$

2. Kutta condition at the trailing edge of the impeller and stator blades:

$$\left|\vec{V}_{T.E.}\right| < \infty \qquad [8.18]$$

3. Kinematic Boundary Condition on the wake surface (S^W) trailing the impeller and stator blades:

$$\Delta \frac{\partial \phi}{\partial n} = (\hat{n} \cdot \nabla \phi)^u - (\hat{n} \cdot \nabla \phi)^l \qquad [8.19]$$

where u and l represent the upper and lower surfaces of the wake, respectively.

4. Dynamic Boundary Condition on the wake surface (S^W) trailing the impeller and stator blades:

$$\Delta p = p^u - p^l = 0 \qquad [8.20]$$

where the pressure is denoted by p

5. Inlet Condition on the duct inlet opening surface (S^{R+}):

$$\hat{n} \cdot \vec{V} = \hat{n} \cdot \vec{V}_s + \frac{\partial \phi}{\partial n} = \frac{Q_j}{A_i} \qquad [8.21]$$

6. Outlet Condition on the duct outlet opening surface (S^{R-}):

$$\int_{S^{R+}} \hat{n} \cdot \vec{V} dS + \int_{S^{R-}} \hat{n} \cdot \vec{V} dS = 0 \qquad [8.22]$$

The waterjet system can be described in this manner, provided that the assumptions are valid and the boundary conditions are satisfied. Such assumptions are not always warranted, however, and the solutions are limited to specific flow conditions. Progress in the field of computational fluid dynamics has made it possible to solve the Navier Stokes equations that govern all aspects of fluid flow. CFD is therefore a much more versatile tool in the analysis of real world problems as the solutions are not restricted to potential flow. CFX 5.6® software was used to perform the simulation. It solves the unsteady Navier-Stokes equations using the finite volume method, described in Chapter 7. The remainder of this chapter is dedicated to the development of a numerical model of the waterjet system, and its subsequent simulation using computational fluid dynamics.

8.2 Flow Domain

The first step in any CFD simulation is determining the extent of the flow domain. The computational domain must be large enough to capture all of the flow properties of interest, while remaining efficient. Computer resources are limited, and an efficient

simulation is one that converges to a useful, and accurate solution in as little time as possible.

In the case of the waterjet experiment, much of the computational domain is fixed by geometry. Specifically, the walls of the waterjet, from the inlet to the nozzle outlet, form a fixed barrier, outside of which the solution has no relevance to this study. Modelling the entire wind tunnel, however, would increase the complexity of the simulation and not provide any further insight into the waterjet performance. Conversely, the behaviour of the jet stream exiting the waterjet is of interest, and the computational domain had to be extended in order to resolve the flow in this area.

It was decided that the CFD model would be developed from a series of modular components joined by specific interface connections. This permitted individual components to be modified, edited, added and removed without altering the mesh characteristics of other components (nodal connections, mesh density, etc.). As shown in, Figure 8-3, the model was made up of the following components: tunnel, jet, impeller, exit, and stream.

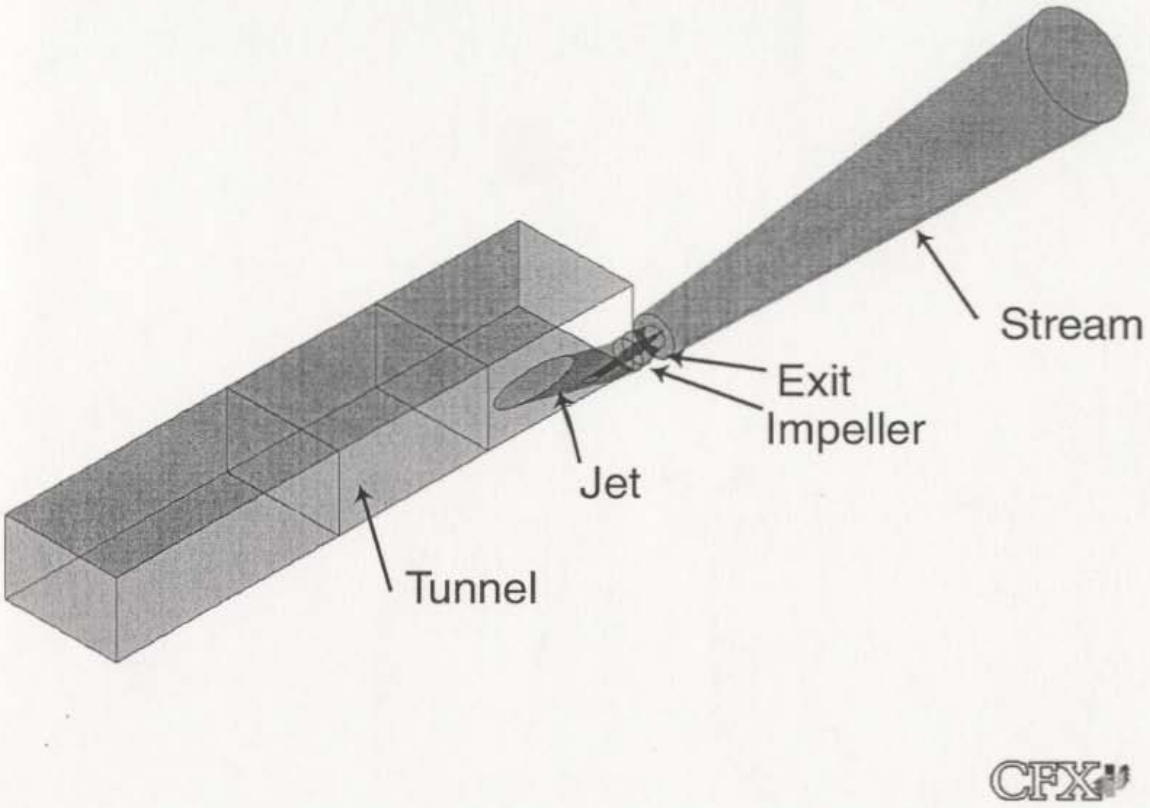

Figure 8-3. Component description

An accurate representation of the velocity profile approaching the waterjet inlet was necessary for agreement with the physical tests. The tunnel component was designed such that the numerical representation of the wind tunnel wall that was attached to the waterjet closely resembled that of the physical experiment. The remaining sides of the wind tunnel were not as important to the study and the grid was much coarser at these inconsequential surfaces. More grid refinement close to the wall of the wind tunnel meant that the velocity profile at the inlet was more accurate and well defined than in other areas of the tunnel. In the interest of computational efficiency, and once the size of the entire mesh was finalised, the length of the tunnel section was minimised. The modular

approach allowed for a number of different tunnel sections to be used. Refinement of the tunnel section was complete when the velocity profiles at stations 0, and 1a agreed with the experimental results.

The jet component consisted of the physical waterjet, without the impeller, stator, or nozzle. A Computer aided design (CAD) model was developed using Rhinoceros® software and imported into CFX in the IGES file format. After the file was imported, considerable editing was required in order to transform the model into a format that could be used for numerical analysis. This is due to the non-matching edges that result from geometric features in the CAD file that were approximated by the IGES format (CFX Build, 2003). According to Hu and Zangeneh (2001), the influence of the shaft is significant, and should be included in any numerical analysis of the intake duct. Inclusion of the shaft greatly complicated the geometric features of the mesh, but was considered necessary for a more complete description of the waterjet. Figure 8-4 shows a close-up view of the jet, impeller, and exit sections. It can be seen from the figure that the shaft has no rotational velocity since this waterjet unit was equipped with a shaft protection hub.

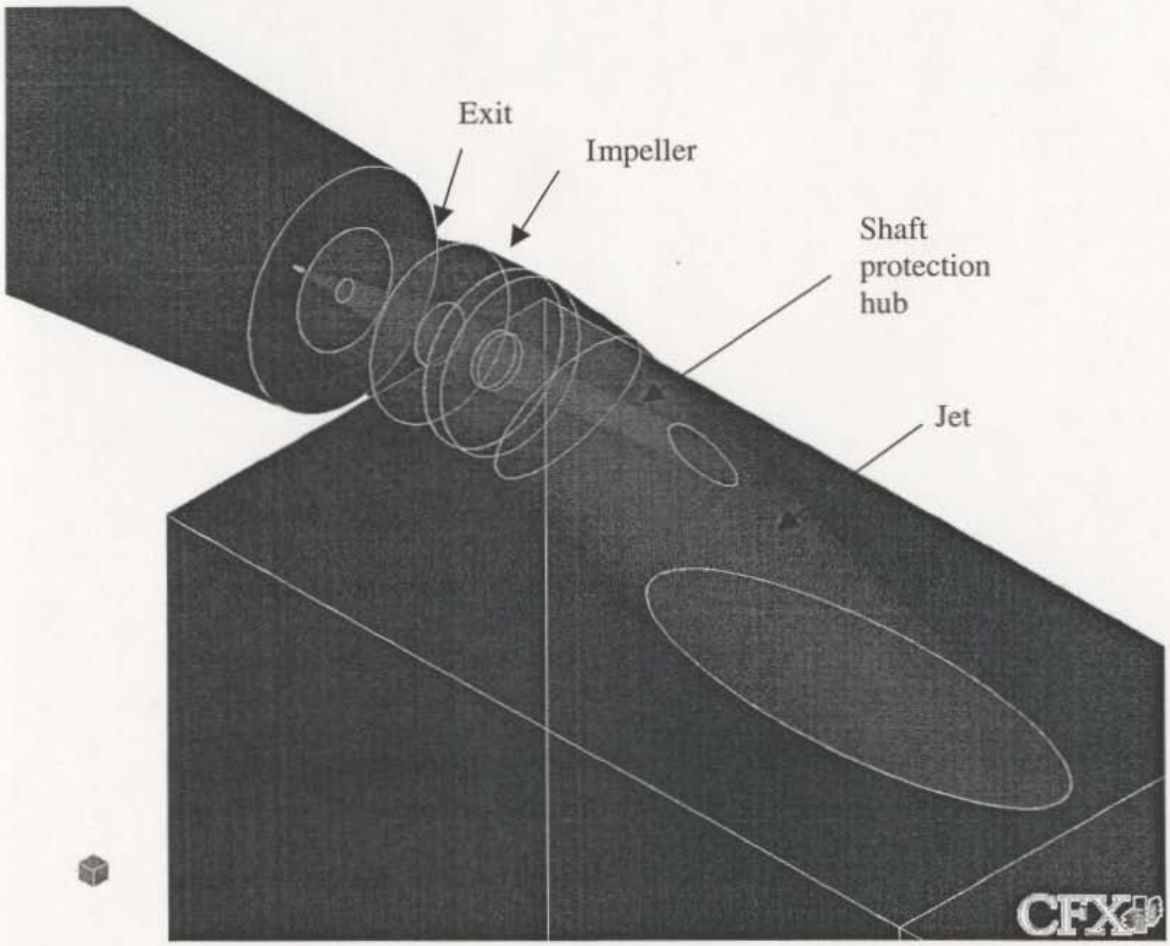

Figure 8-4. Jet, impeller, and exit

The impeller component was designed to model the pressure increase between the face of the impeller, and it's exit. It was decided that modelling this section with a rotating impeller would be far too time consuming, and its relevance to the overall system performance would be questionable. Instead, it was decided that a source term would be used in its place that reflected the pressure jump across this section. The impeller section was therefore built as a sub domain of the waterjet system so that source terms could be applied across the volume occupied by the physical impeller.

Similarly to the work of Widmark and Gustafsson (1998), the source term was uniform and did not account for the swirling of the rotor; therefore it was not necessary to model the stator.

The exit component simulated the system downstream of the impeller and consisted of the nozzle section and a stator cone. Like the jet component, it was designed directly from CAD drawings of the waterjet and modified as necessary.

The stream component was needed to predict the behaviour of the waterjet system beyond the outlet. This component had to be large enough to capture all of the jet stream, without taxing the simulation computationally. The grid resolution varied throughout the section and was much denser in the region of the assumed vena contracta. Similarly to the tunnel component, the size of the stream section was minimised such that it extended just far enough beyond the jet stream of the waterjet.

8.3 Meshing

As discussed in the introduction to computational fluid dynamics (Chapter 7), meshing is an extremely time consuming part of a numerical simulation. A background in fluid dynamics was necessary in order to identify areas that required further refinement from those that could be much coarser. The component approach to the simulation of this study allowed for tremendous variability between sections, not only in terms of grid density, but also in regard to the type of mesh geometry throughout the waterjet system. Grid density was increased in areas where a great deal of variation in the flow was expected,

and coarsened where the flow was assumed uniform, or not relevant. For this reason, an inflated boundary was created at all solid surfaces in order to account for the high velocity gradients normal to the surface, due to boundary layer effects. A computationally efficient mesh requires that elements in these regions have high aspect ratios, but tetrahedral elements are highly distorted at a solid surface. CFX overcomes the problem by using prisms to create a mesh that is finely resolved normal to the wall, but coarse parallel to it. This is known as an inflated boundary and Figure 8-5 shows a mesh made up of both inflated and tetrahedral elements.

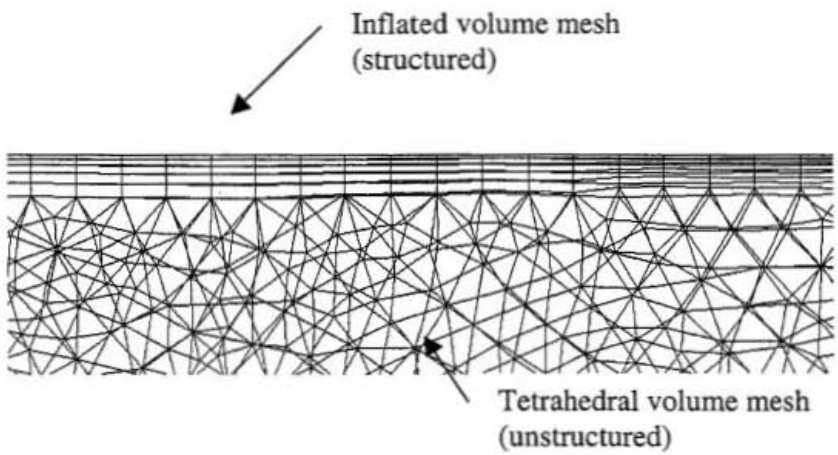

Figure 8-5. Inflated boundary

The meshes were also refined at each of the waterjet stations. This was done in order to produce a very dense collection of elements where point velocities were recorded during the physical experiment. The momentum flux calculations, presented later in this chapter, then benefited from a number of sampling points that would have proven extremely time consuming, if not physically impossible, to reproduce experimentally. Component

geometry also influenced the grid density and curved sections, for example required a higher grid density than flat uniform sections.

In order to define the boundaries between different components (meshes), domain interfaces were required. In the simulation, a fluid-fluid interface was defined between components and connected using General Grid Interface (GGI) functionality in CFX. The GGI interface permits the joining of different types of meshes and reduces the effort required for mesh generation. This is accomplished by generating a series of meshes and joining them together, rather than creating a single mesh for the entire domain (CFX Solver Modelling, 2003).Figure 8-6, shows the completed mesh of the waterjet system.

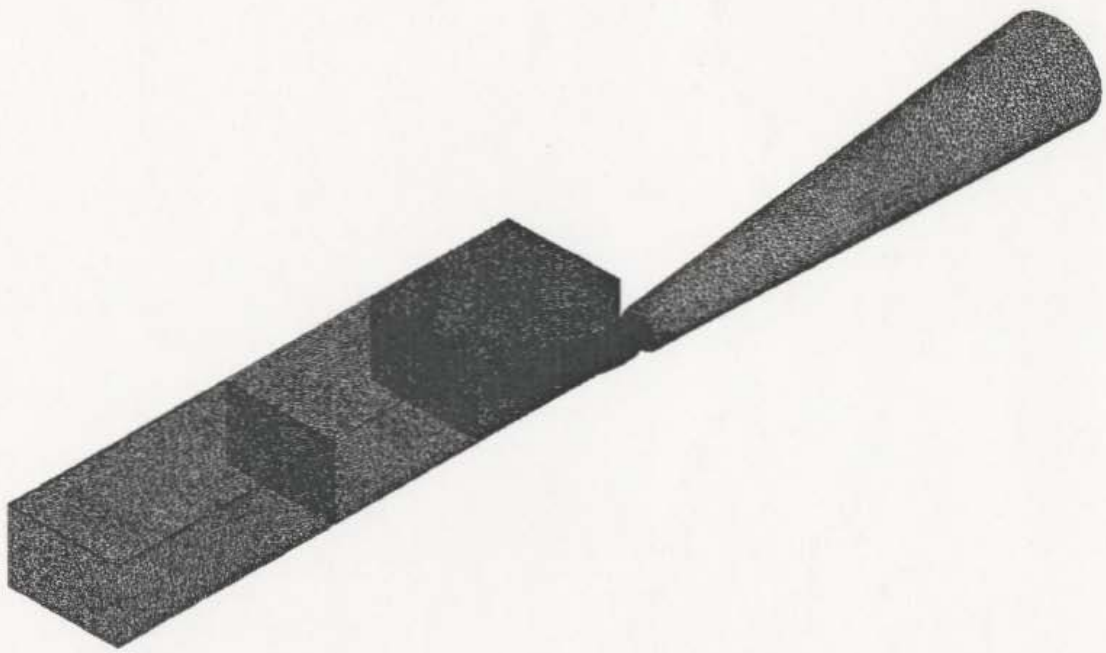

Figure 8-6. Mesh of waterjet system

Figure 8-6 shows that in order to replicate laboratory conditions in the wind tunnel, and capture the jet stream at the waterjet outlet, the computational domain had to be much

larger than the space occupied by the waterjet unit itself. For this reason, a large number of nodes were required in the tunnel and stream components, even though the grid densities in these regions were much smaller than those in the jet, impeller, and exit components. For example, although the density of the grid in the impeller component was more than 200 times greater than that in tunnel component from the wind tunnel inlet to the waterjet inlet, the volume occupied by the tunnel component was almost 300 times larger. Figure 8-7 and Figure 8-8 show estimates of the contribution of each of the components in terms of total volume and number of nodes.

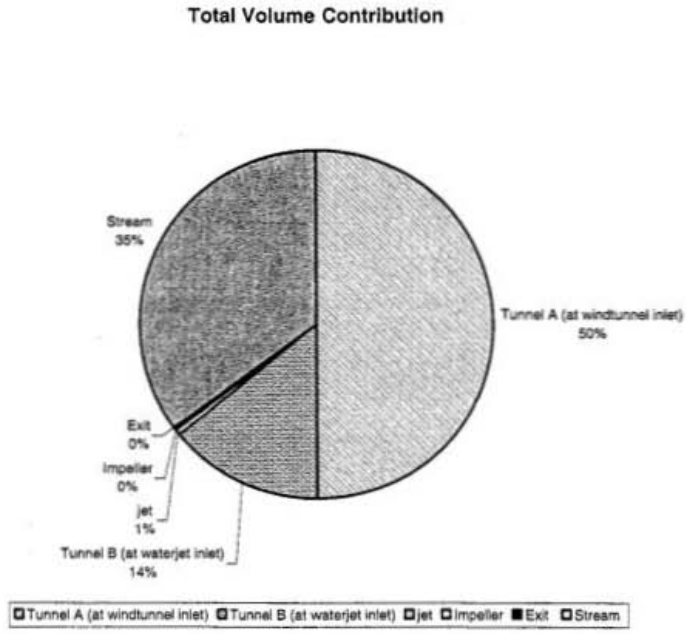

Figure 8-7. Component Volume Contribution

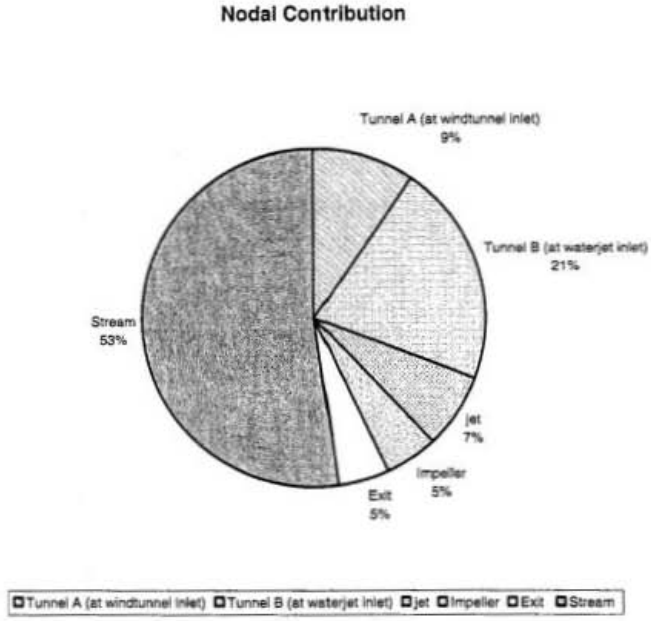

Figure 8-8. Component Nodal Contribution

The grid density for much of the domain is difficult to view in this manner and the variation in grid density throughout the waterjet can be seen more clearly in the isometric and top views of Figure 8-9 and Figure 8-10, which show the most important aspects of the mesh

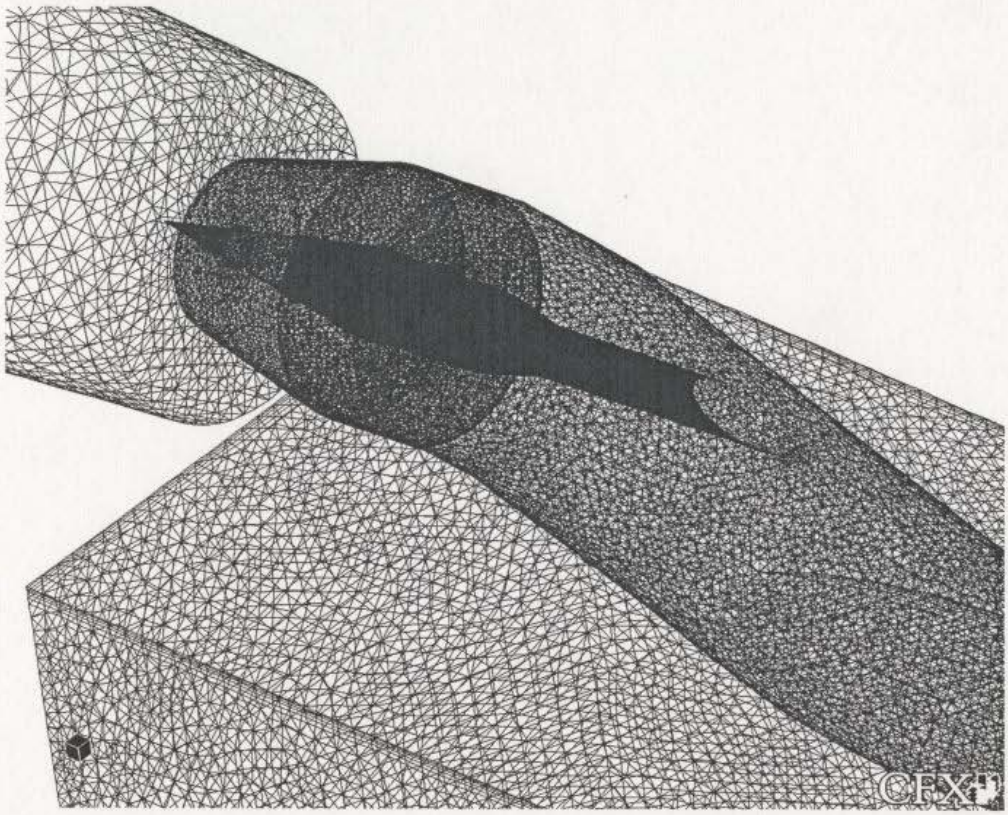

Figure 8-9. Isometric view of waterjet mesh

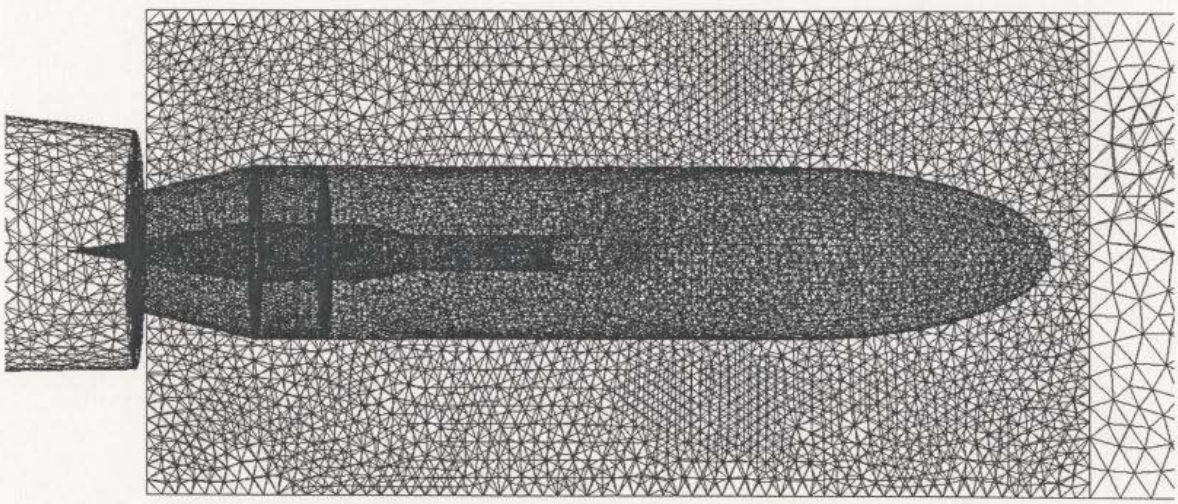

Figure 8-10. Top view of waterjet mesh

8.4 Boundary Conditions and Solver Parameters

The next step in the development of the numerical simulation was to define the boundary conditions. Figure 8-11 shows the boundary conditions applied to the waterjet simulation:

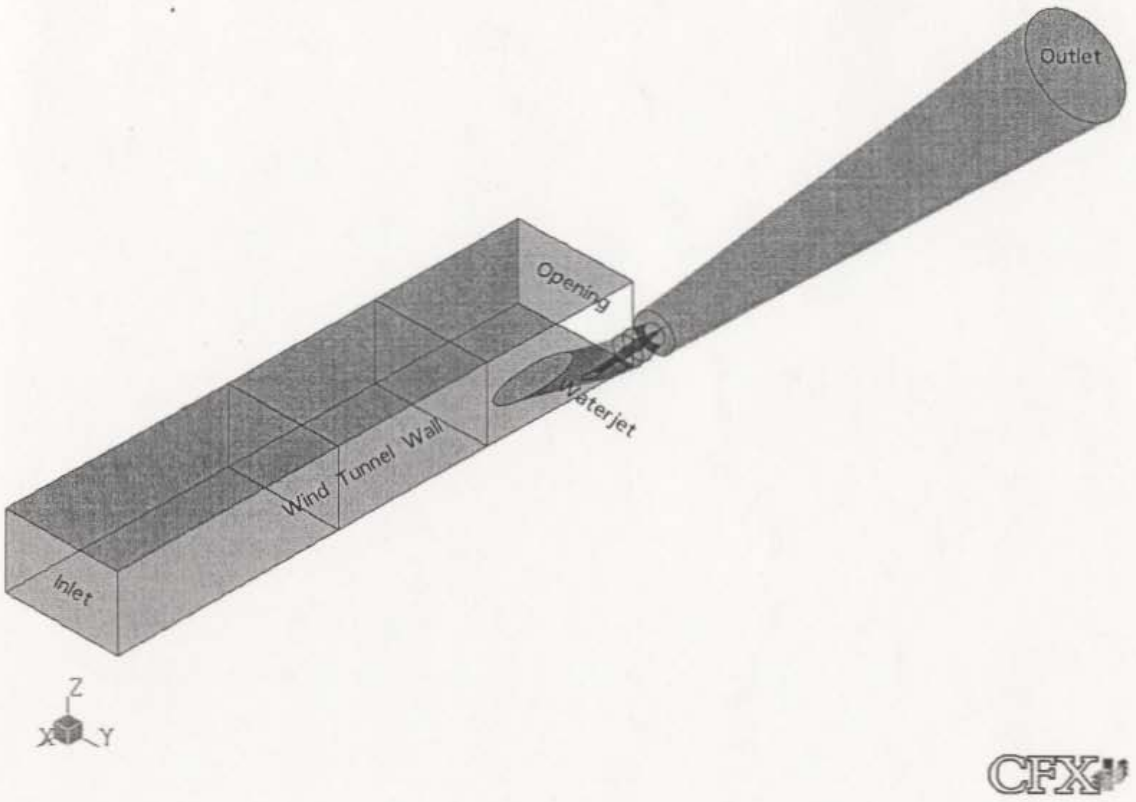

Figure 8-11. Boundary conditions

A mean velocity of 5 m/s was specified through the inlet boundary, located at the wind tunnel cross section, far from the waterjet. The wind tunnel wall was imparted with a surface roughness to simulate the roughness of the plywood wall of the physical apparatus. Turgay et al (1996) have specified that the roughness of plywood is between 0.3 mm and 0.5 mm and a value of 0.5 mm was therefore applied. As stated in the chapter

on instrumentation (Chaper 5), the wind tunnel that was used for the experiment was of the open circuit variety. As such, the flow is subject to atmospheric influences. Although the influence was assumed to be negligible for the purposes of experimentation, an opening boundary condition was applied nonetheless to the end of the numerical wind tunnel, to account for any changes in the flow that may have resulted. The outlet was located at the end of the stream component, sufficiently far away from the nozzle to capture all of the behaviour in the wake.

8.5 Solver Parameters and Initialisation

In order to replicate the laboratory conditions, key parameters had to be specified in the numerical simulation. The parameters are summarised in Table 8-1

Table 8-1. Solver parameters

Parameter	Setting
Advection scheme	high resolution
Physical timescale	0.5 s
Maximum number of iterations	300
Convergence criteria	Max residual
Residual Target	0.0001
Simulation type	steady state
Material	air @ 25 °C and 1 atm
Air density	1.185 kg/m^3
Air molar mass	28.96 kg/kmol
Air dynamic viscosity	1.831 x 10^{-5} kg/m s
Domain reference pressure	1 atm
Buoyancy	non buoyant
Impeller Subdomain	
Location	Impeller
Source	108 kg/m^2 s
Inlet	
Flow regime	subsonic
Mass and momentum	normal speed = 5 m/s
Turbulence	medium intensity (5%)
Outlet	
Flow regime	subsonic
Relative pressure	0 Pa
Opening	
Flow regime	subsonic
Relative pressure	0 Pa

The physical timescale was the result of an iterative process. Initially, the number was based on the residence time (Δt) of the fluid, that is, twice the time it took the fluid to move from the inlet to the outlet:

$$\Delta t = \frac{L}{2U} \qquad [8.23]$$

where,

L – is the length of the domain [m]

U – is the mean velocity throughout the domain [m/s]

At very small time scales a numerical solution can be extremely time consuming, while overly large time scales are characterized by bouncy convergence, or solutions that do not converge at all. The initial solution to the simulation required a small timescale, since it was expected that the solution would oscillate a great deal due to a limited initial guess. For subsequent work, the results of the previous simulation were used as an initial guess, which meant that the time scale could be increased

The simulations were performed with a high-speed personal computer running at 2 gigahertz and equipped with 2 gigabytes of Random Access Memory (RAM). After an initial solution was found, run times were very short (about 1.5 hours), and less than 20 iterations were required to achieve convergence for small changes to the system.

The residual is a measure of the local imbalance of each conservative control volume equation and is the most important measure of convergence (CFX Solver Advice, 2003). For most engineering applications, a maximum residual of 1×10^{-4} represents good

convergence and it is often not possible to achieve convergence as low as $5x10^{-5}$. Initially, the convergence criterion for the simulation was set at $1x10^{-4}$. Through the course of refinement, however, the residual target was reduced to $5x10^{-5}$, with little changes in the results.

The source term at the impeller was also the result of an iterative process. A solution to the system with no source term was first found and the strength of the source was then increased until key parameters, such as flowrate through the system, matched the experimental results. In order to finalise the mesh density and domain dimensions, a grid dependence study was performed.

Before a CFD solution commences, it is necessary to specify initial values for all of the solved variables. Steady state simulations, for example, begin calculations based on a flow field assigned to the solver. For the simulation of this study, a velocity of 5 m/s, directed into the wind tunnel was initially supplied in order to start the calculations. The results of the initial simulation then formed the initial guess for the subsequent simulation, and the process was repeated, as the solution was refined through the course of many iterations.

8.6 Grid Independence

As discussed in Chapter 7 a grid dependence study is necessary to minimise errors associated with the coarseness of a grid. Grid independence was achieved when key results did not change through subsequent refinement of the grid. The approach to this simulation required grid independence for each of the individual components that

comprised the numerical domain. As shown in Figure 8-12, mean velocity measurements were taken at a series of locations along the waterjet.

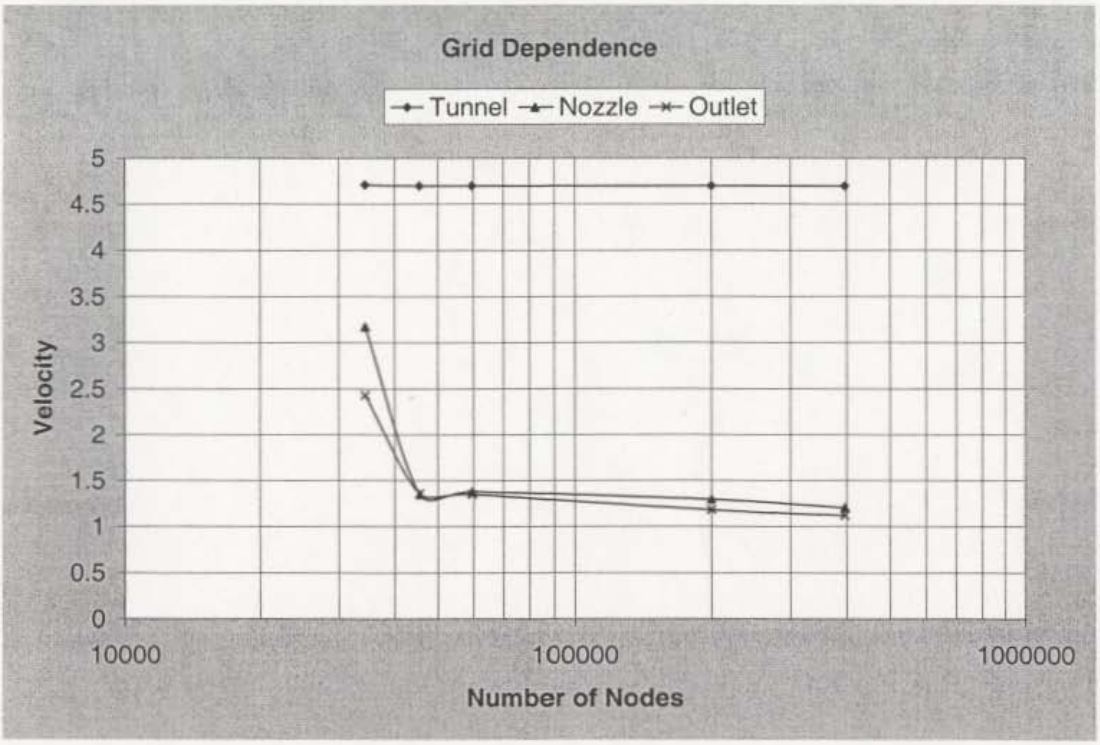

Figure 8-12. Grid refinement

The results showed that the grid density should be decreased in the tunnel section, and increased in the waterjet section. The resolution was therefore adjusted in these areas until grid independence was achieved. The following table summarises the final grid statistics:

Table 8-2 . Mesh Statistics

Number of nodes	561,654
Number of elements	2,770,519
Tetraheda	2,598,000
Wedges (inflation elements)	171,414
Pyramids	1,105

8.7 Validation

The numerical model was validated by the results from physical experimentation. Specifically, the volumetric flowrate through the waterjet system was used to determine the strength of the source term in the simulation. In addition, the contour plots produced by the physical tests, and point measurements at each of the waterjet cross-sections (stations) were compared with results from the simulation. A comparison was also made with the results of other published works (Verbeek et al, 1998, Roberts et al, 1998, Watson , 1998).

The contour plots presented in this chapter are based on both experimental and numerical work. Plots of the experimental work consisted of about one hundred and twenty data points while the contour plots of the numerical simulation benefited from the tremendous level of detail possible through CFD analysis, and consisted of almost five thousand. The experimental results discussed in Chapter 6 indicated that for the impeller rotating at 1000 rpm and the wind tunnel velocity set at 5m/s, the volumetric flowrate through the waterjet was 0.25 m^3/s. The source term at the impeller was then adjusted until the flow through the simulation matched the flow rate obtained through experimentation. The

orientation of the contour plots was described in Chapter 6, and is reproduced in Figure 8-13.

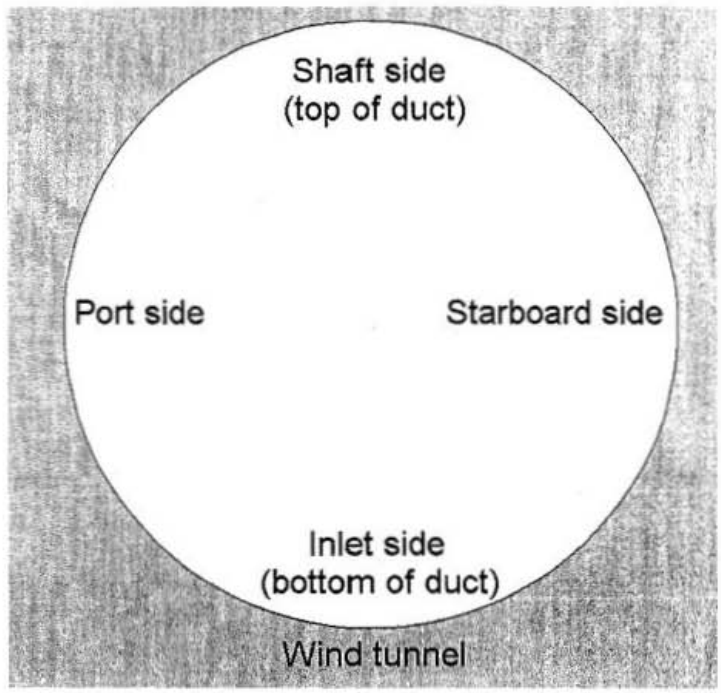

Figure 8-13. Orientation of contour plots

Figure 8-14 and Figure 8-15 show the contour plots at station 2. The velocity values are similar between the two plots, and they exhibit the same trends. Differences between the two plots may be attributed to the rotation of the impeller in the model tests and the turbulence it induced, along with a degree of experimental uncertainty. The offset in Figure 8-15, for example may have been the result of impeller rotation. Also, the plots produced by the simulation contain many more data points and the algorithms used to fit a surface contour over the data are not forced to interpolate over as large an area (i.e. data points are much closer together).

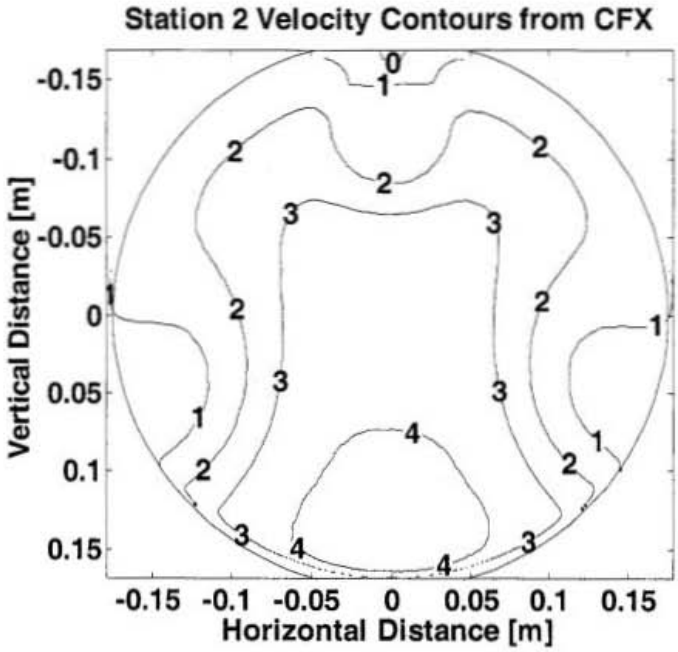

Figure 8-14. Station 2 contour plot (CFD)

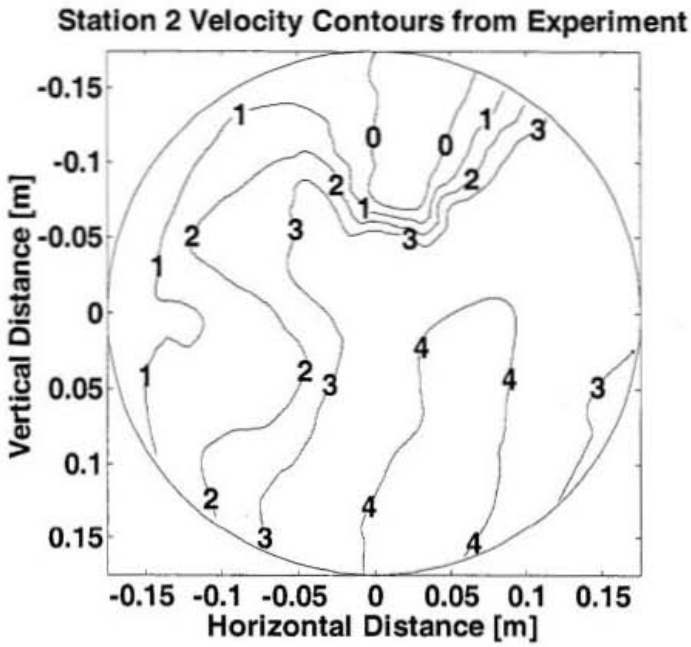

Figure 8-15. Station 2 contour plot (model tests)

Station 6 and station 7, shown in Figure 8-16 through Figure 8-19, showed good agreement, bearing in mind the effect of the rotating impeller and limited number of sample points in the physical experiment.

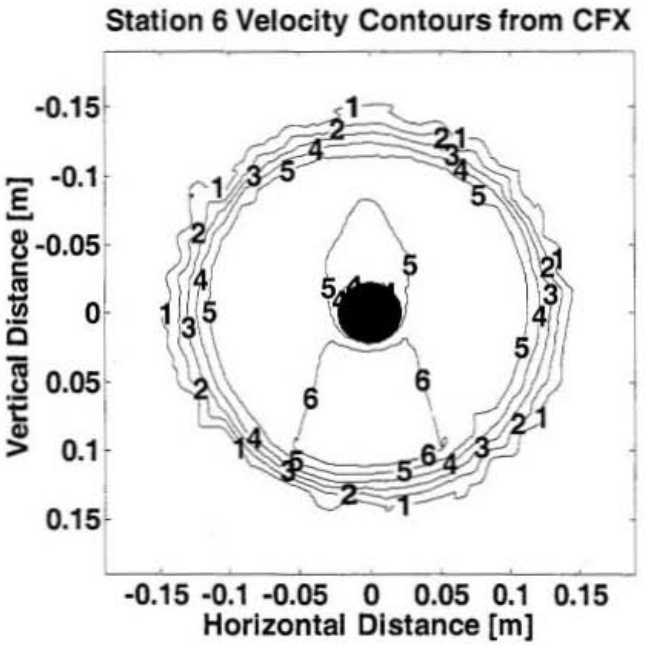

Figure 8-16. Station 6 contour plot (CFD)

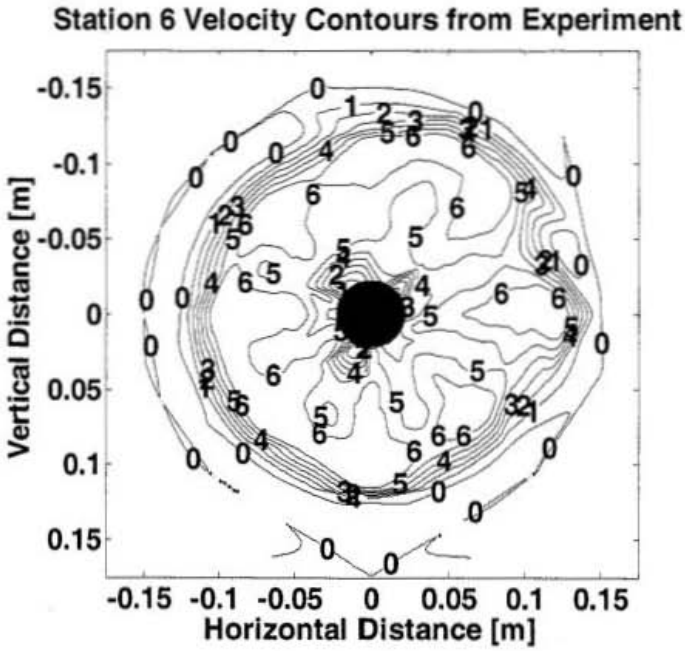

Figure 8-17. Station 6 contour plot (model tests)

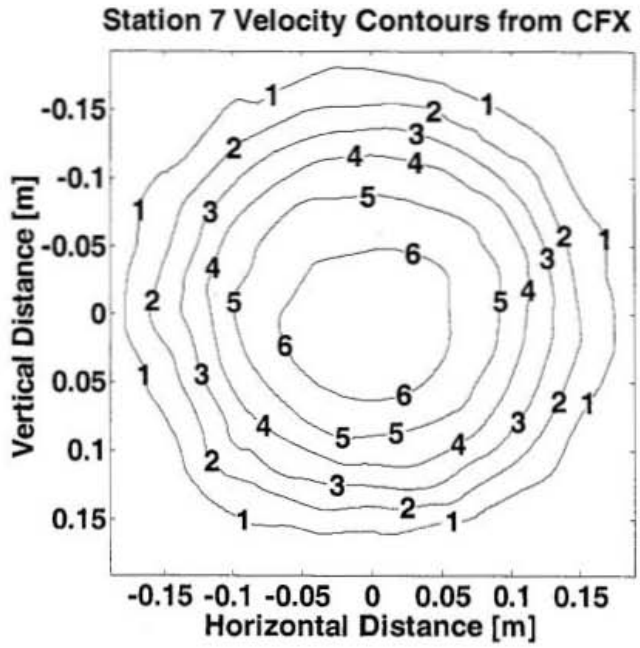

Figure 8-18. Station 7 contour plot (CFD)

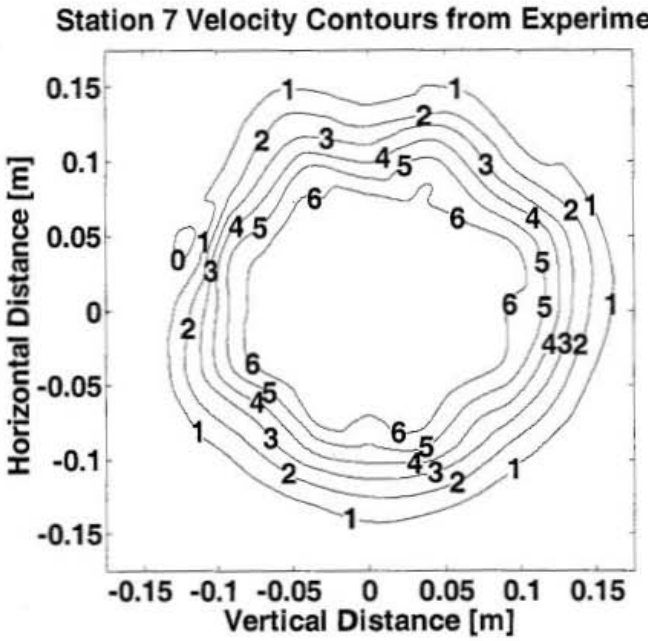

Figure 8-19. Station 7 contour plot (model tests)

The plots showed close agreement between velocity variations in terms of magnitude and location. In several instances the model tests appeared to have small 'hot-spots', where velocity values reached a maximum. This can be attributed to experimental uncertainty, resulting from interpolation between high and low data points and it should be considered when comparing the plots.

The velocity profile at station 1a was used for validation and is shown in Figure 8-20. It is clear from the figure that the flow entering the waterjet is similar for both the model and simulation. Differences exist near the wall, however, where the experimental velocity profile is larger than that obtained through the numerical simulation. There was considerable difficulty in matching the velocity profiles, since the experimental observations were not identical to those predicted by flat plate theory. As mentioned in

Chapter 6, the flow at the inlet is influenced by the roughness of the plywood wall and the transition from plastic to wood surfaces that occur throughout the wind tunnel. An effort was made to account for these inconsistencies by varying the roughness parameter along the wall of the numerical model, using published data (Turgay et al., 1996). The results show that the numerical simulation of the velocity profile at station 1a was closer to the experimental observations than those predicted from flat plate theory Figure 6-16, but an exact duplication of the flow behaviour was not obtained. In order to improve the accuracy of the simulation, the roughness along the wall of the numerical wind tunnel would have to be determined from physical experiments.

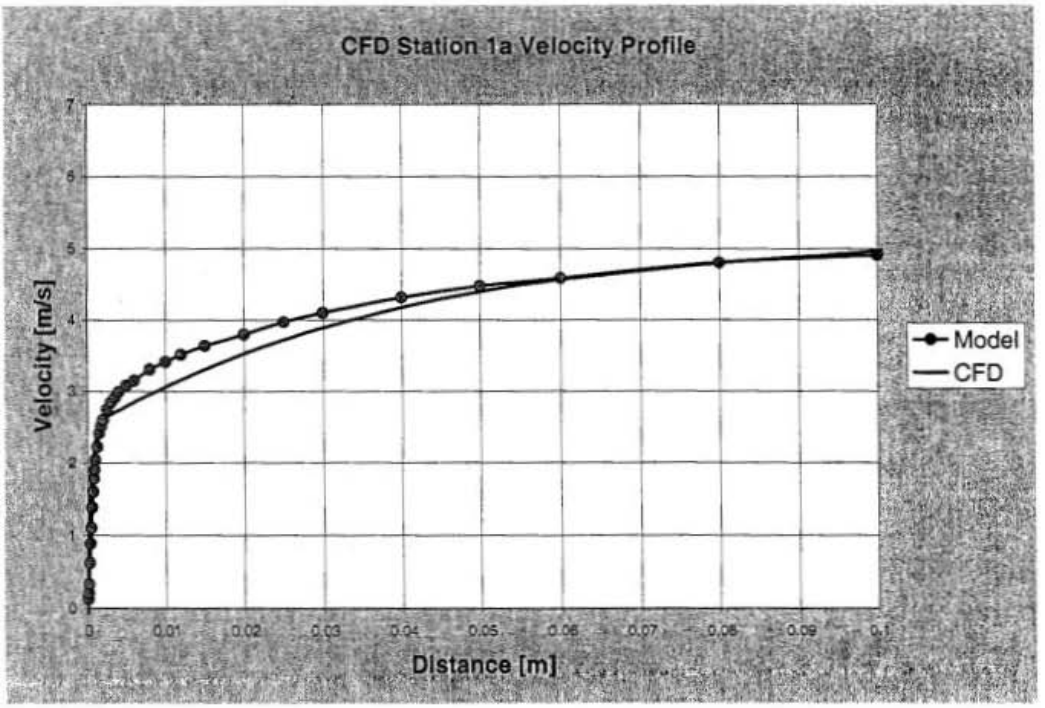

Figure 8-20. Comparison of velocity profiles

The most important part of the validation process was to establish close agreement between the flowrates of the physical and numerical tests. With this accomplished it was then possible to investigate the behaviour of the waterjet system and determine its performance characteristics.

8.8 Simulation Results

In addition to the figures discussed in section 8.7, the simulation provided a great deal of visual information with respect to the behaviour of the waterjet system. Figure 8-21 shows the velocity distribution through the centreline of the waterjet. Of particular interest were the shielding influence of the shaft and the distribution of velocity in the jet. The velocity dropped dramatically in the region behind the shaft, and was significantly lower along the wall of the duct section closest to the shaft. It is assumed that the effect of the shaft was exaggerated in the simulation, since in reality a rotating impeller would increase turbulence and make the distribution of velocity more uniform (Verbeek et al., 1998). According to Manunga (1998), flow separation at the inlet roof exists in real waterjets, and reduces their performance and efficiency, since impellers are designed to handle uniform loads. This behaviour was predicted by the numerical simulation and is illustrated by the non-uniformity of velocity contours at the roof of the waterjet inlet in Figure 8-21 and Figure 8-22.

This is a very active area of research, but is not the focus of this study. An advantage of the modular approach in the simulation, however is that it lends itself well to modification. Replacing the existing impeller component with a detailed rotating model

would be a time consuming endeavour, but a comparison between simulations would be helpful in identifying the extent of flow separation in the real waterjet.

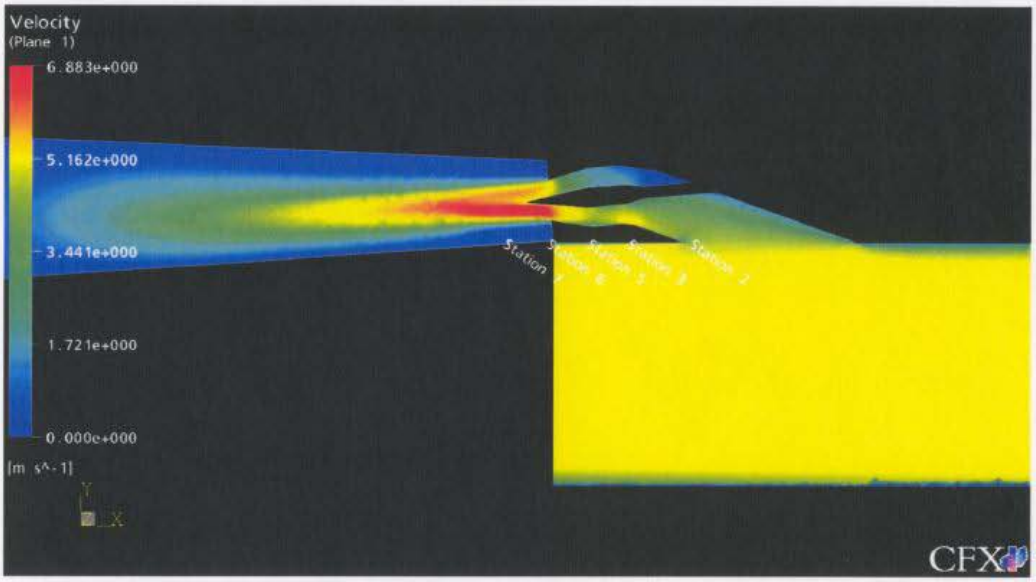

Figure 8-21. Centerline velocity

Viewing the figure in terms of velocity contours, Figure 8-22, highlights the distribution of velocity at the inlet and revealed some interesting features of the system near sharp corners. To further this, the system was plotted according to its pressure contours. The results, shown in Figure 8-23, reveal a low-pressure region near the intake, and increased pressure in the impeller section.

Figure 8-22. Centerline velocity contours

Figure 8-23. Centerline pressure contours

The co-ordinate axes for the numerical simulation are shown in Figure 8-11 and contours of the transverse velocity components (y,z) at various stations are shown in Figures 8-24 through 8-29 Although not substantiated by experimental data, these plots support the notion that the axial velocity measurements obtained through hot-wire anemometry could have been influenced by non-axial velocity components. According to Figure 8-24 and Figure 8-26, transverse velocity components at the inlet throat and nozzle outlet are significant and velocity measurements taken during physical testing were likely influenced by high cross-currents in these areas.

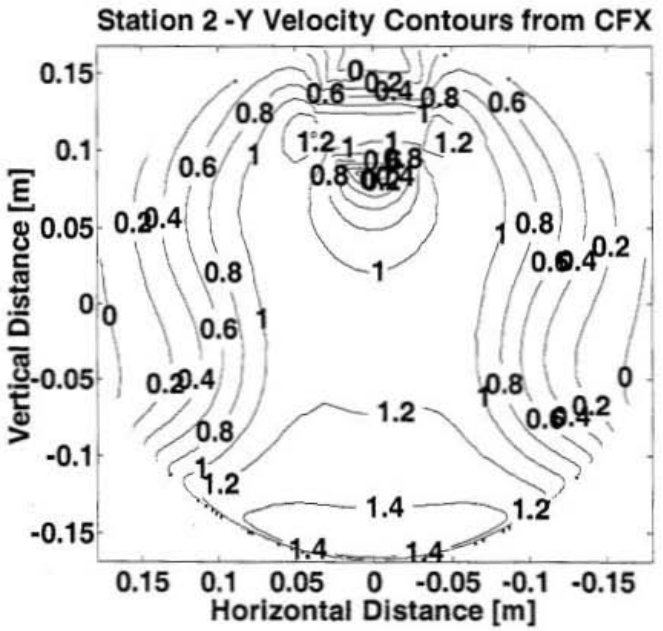

Figure 8-24. Station 2 - Y Velocity Contours (CFD)

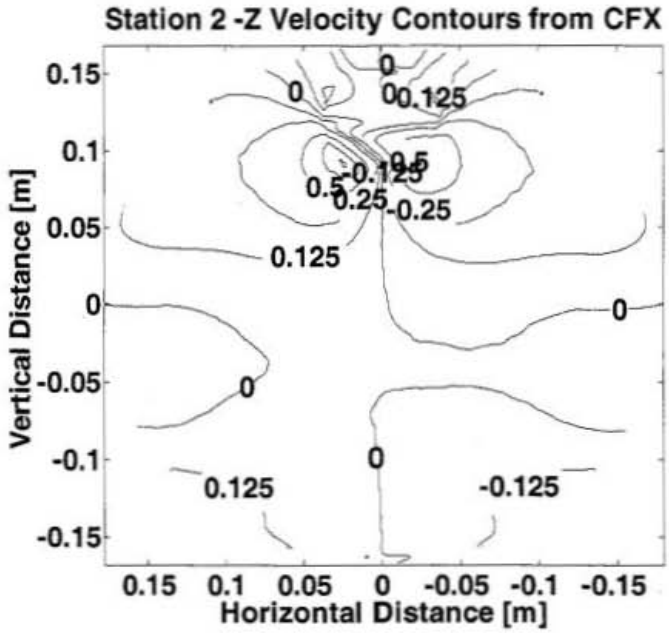

Figure 8-25. Station 2 -Z Velocity Contours (CFD)

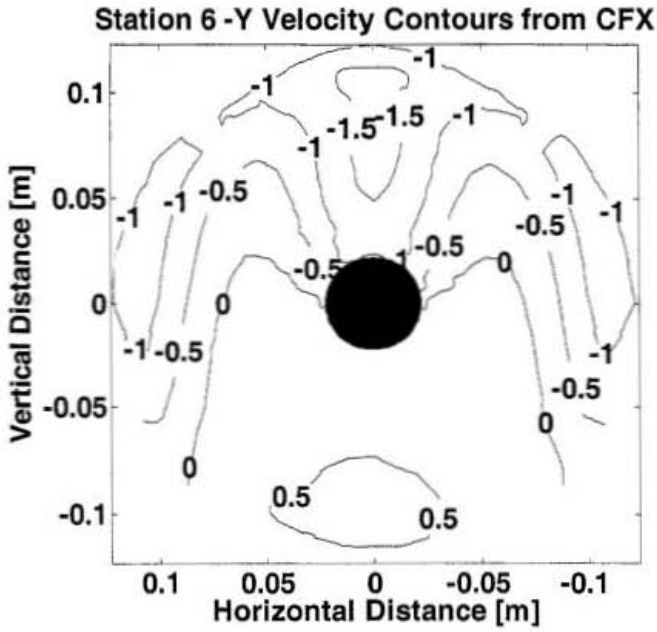

Figure 8-26. Station 6 -Y Velocity Contours (CFD)

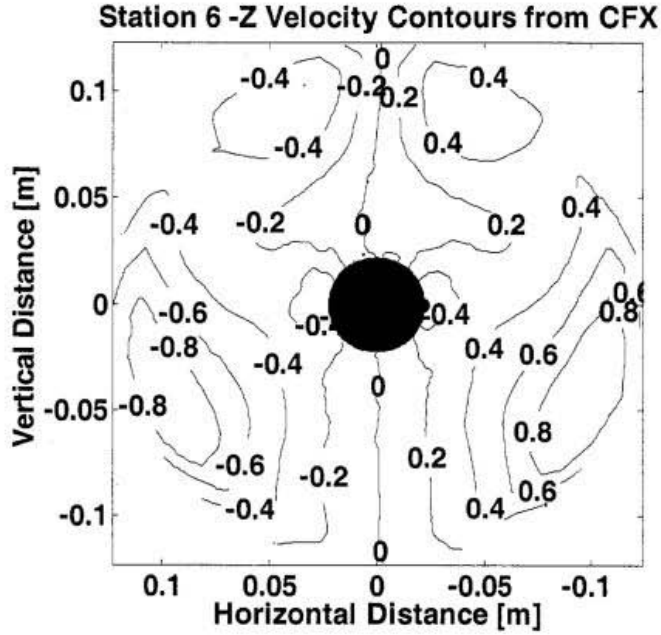

Figure 8-27. Station 6 -Z Velocity Contours (CFD)

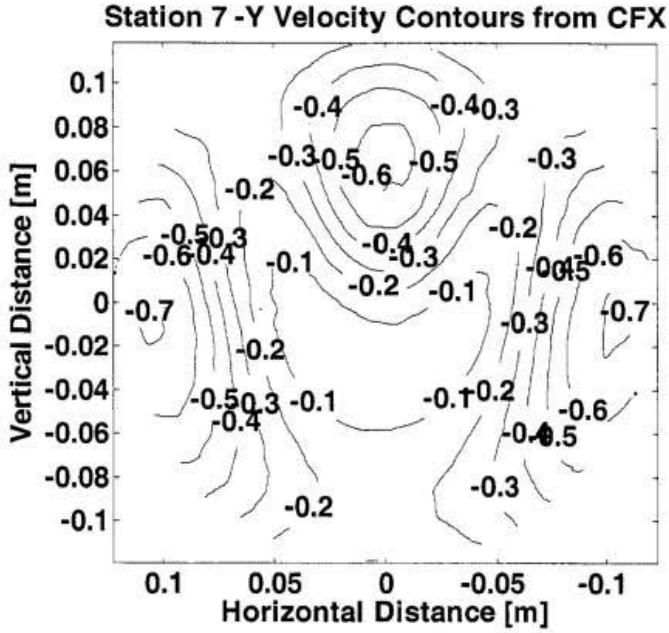

Figure 8-28. Station 7 -Y Velocity Contours (CFD)

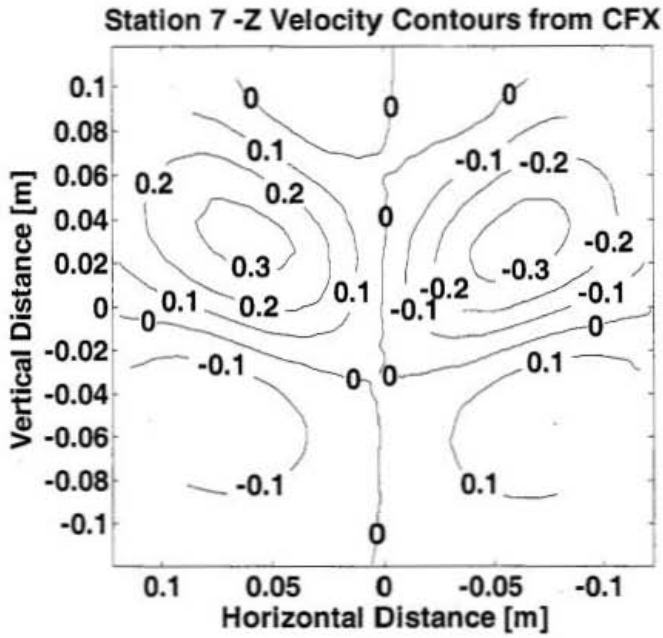

Figure 8-29. Station 7 -Z Velocity Contours (CFD)

8.9 Application of the Momentum Flux Method

The data collected at the stations shown in Figure 8-30 corresponded to the data obtained during physical testing, in accordance with the momentum flux method.

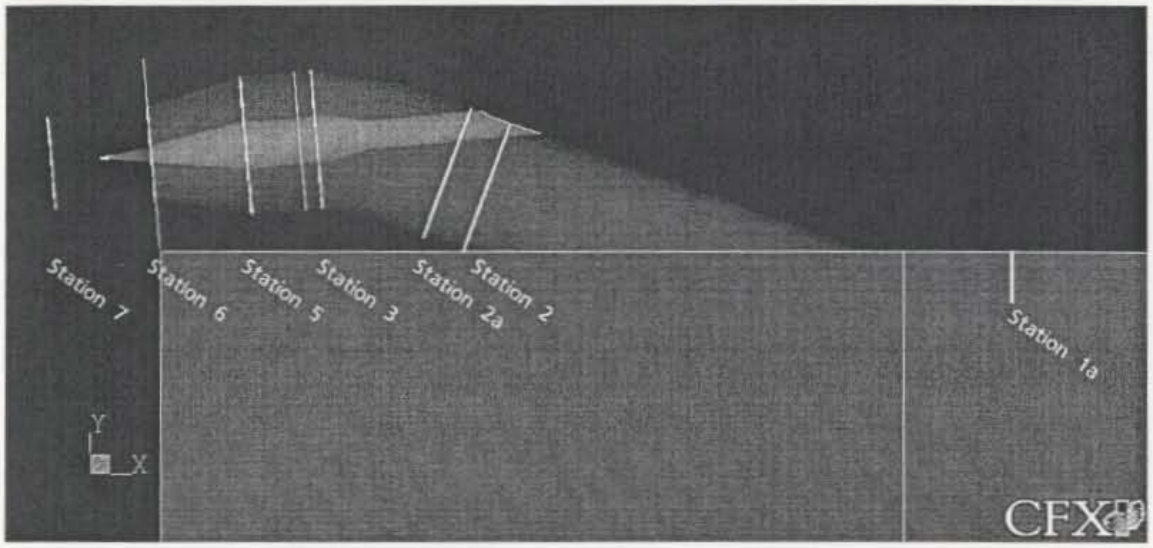

Figure 8-30. Station locations (CFD)

The velocity contours throughout the waterjet unit are shown in Figure 8-31. CFX is equipped with a number of internal functions that can perform integration and averaging over a specified line, area or volume. These functions were used to evaluate the expressions dictated by the momentum flux method described in Chapter 4.

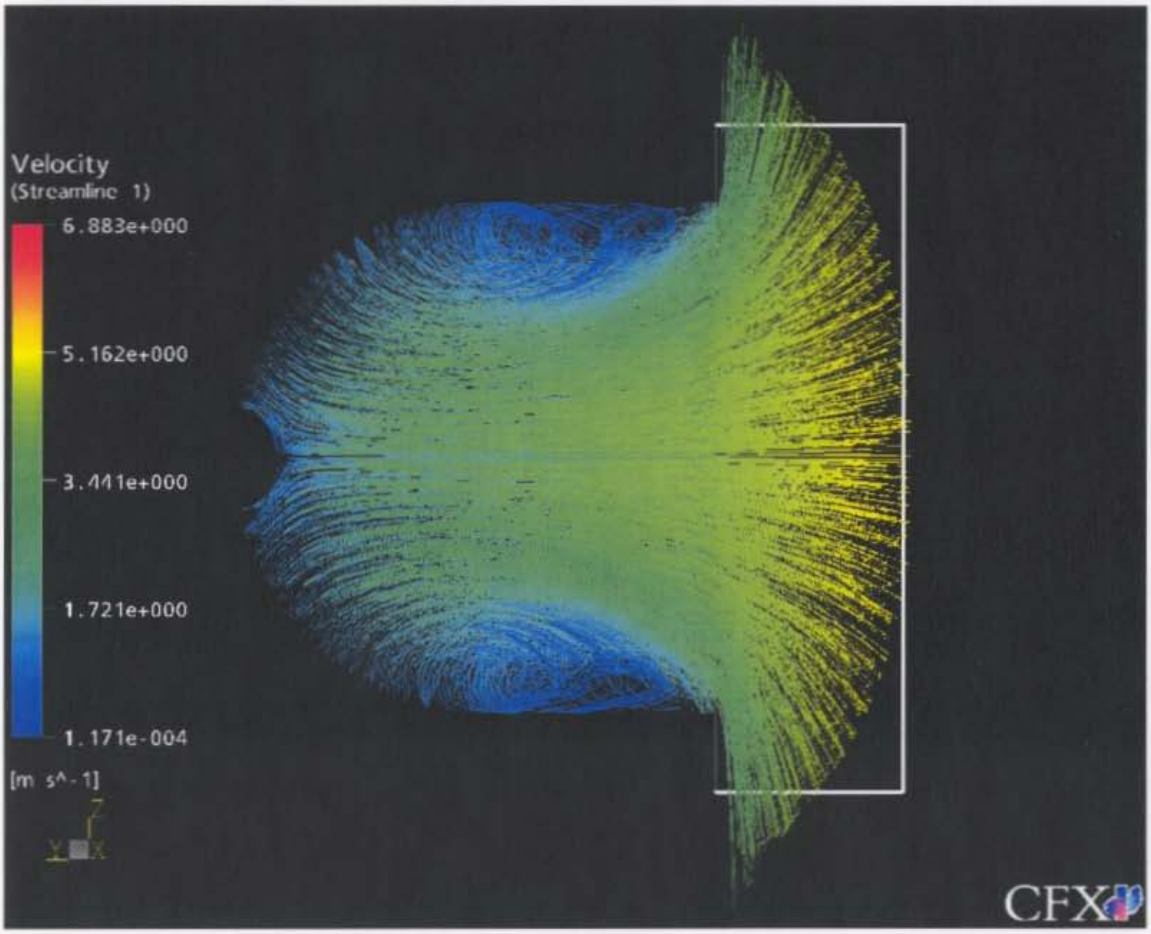

Figure 8-32. Inlet streamlines

It is clear from the figure that the assumed shape did not capture all of the flow that entered the inlet. Although the need for a sensitivity study has been recommended (Kruppa et al., 1996) the approximation appeared to have accounted for most of the flow through the inlet. A more mathematically sophisticated approximation may provide a more accurate representation of the flow, but a substantial improvement in the final prediction may not result.

The location of the vena contracta was assumed during physical testing but it was possible to verify its position using the results of the simulation. At the vena contracta the static pressure coefficient is zero. Numerical results showed that the static pressure coefficient was close to zero (3×10^{-5}) at the location chosen for station 7 during physical tests. In an effort to produce more accurate results and higher resolution at this location, station 7 was further refined and the cross sectional area was calculated based on the flowrate through the waterjet.

Recall from Chapter 4 that in order to compute the momentum and energy fluxes throughout the waterjet unit, an accurate description of the flowrate is necessary. The discrepancies that exist between the experimental and simulation results are due primarily to the inconsistencies in the measured flowrate. The inability of the single wire anemometer to measure flow in three dimensions, coupled with the swirling motion and turbulence induced by the rotating impeller, resulted in varied flow rate measurements at disparate locations throughout the waterjet. Station 3 and station 5, located at the pump face and impeller exit were particularly vulnerable to the limitations of hot-wire anemometry in turbulent flow regimes and the accuracy of velocity measurements at these locations is suspect. Furthermore, the equations of momentum and energy flux also rely on an estimate of the energy velocity, V_E at each station. The energy velocity at a particular location is a function of the component of velocity in the direction of motion (u), ship speed (V), and the coefficient of static pressure, C_p. In order to determine the static pressure coefficient, it was necessary to estimate the change in pressure that occurred as the fluid moved from the undisturbed flow region to the station of interest. If

the flow along a streamline is steady, incompressible, and inviscid, the change in pressure can be determined using the Bernoulli equation. The flow in this experiment, however, was assumed turbulent and the change in pressure from one location to another was determined from the energy equation for incompressible flow in pipes (Munson et al., 1998):

$$\frac{P_{out}}{\gamma}+\frac{V_{out}^2}{2g}+z_{out}=\frac{P_{in}}{\gamma}+\frac{V_{in}^2}{2g}+z_{in}+h_L \qquad [8.24]$$

where:

P_{in} and P_{out} are the pressure in and out of the control volume

V_{in} and V_{out} are the velocity components in the direction of flow in and out of the control volume

γ is the specific weight of the fluid

g is the acceleration due to gravity (9.81 m/s^2)

z_{in} and z_{out} are the vertical height of the fluid in and out of the control volume

h_L is the head loss experienced by the fluid as it moves from the beginning to the end of the control volume.

Head losses throughout given sections of the waterjet were classified as either major losses, described in terms of a friction factor, *f*, or minor losses, given in terms of loss coefficients, K_L. Friction factors were determined using the Colebrook formula (1939):

$$\frac{1}{f} = -2.0\log\left(\frac{\varepsilon/D}{3.7} + \frac{2.51}{\mathrm{Re}\sqrt{f}}\right) \qquad [8.25]$$

where ε represents the equivalent roughness in millimetres, D is the diameter of the section, and Re is the Reynolds number. The Colebrook formula was based on experimentals on commercial pipes and is limited by the uncertainties involved in the original work. For this reason, it is generally accepted that 10% accuracy is the best that can be expected in the friction factor estimate (Munson et al., 1998).

Loss coefficients relevant to the waterjet system of this study are presented in Table 8-3 and Table 8-4 summarises the coefficients of head loss throughout the system

Table 8-3. Loss coefficients for various components

Component	K_L
45° branch	0.5
Long radius bend	0.2
nozzle	0.07
contraction	$(1-A_1/A_2)$
exit	1

Table 8-4. Waterjet loss coefficients

Station	Location	Source of Loss	Coefficient
0 - 1a	free stream to station 1a	friction	$f = 0.018$
1a -2	inlet velocity profile to inlet throat	friction	$f = 0.019$
		branch	$K_{Lbr} = 0.50$
		contraction	$K_{Lc} = 0.43$
2 - 3	inlet throat to pump face	friction	$f = 0.019$
		bend	$K_{Lb} = 0.20$
3 - 5	pump face to pump exit	friction	$f = 0.019$
		pump (head rise)	n/a
5 - 6	pump exit to nozzle	friction	$f = 0.019$
		nozzle	$K_{Ln} = 0.070$
6 - 7	nozzle to vena contracta	exit	$K_{Le} = 1$

The major (frictional) loss through each station was computed from:

$$h_L = f \frac{\ell}{D} \frac{V^2}{2g} \qquad [8.26]$$

minor losses due to system components were computed from:

$$h_L = K_L \frac{V^2}{2g} \qquad [8.27]$$

The head rise through the pump was determined from Karassik et al.(1986):

$$h_{iP} = \frac{\eta \omega T}{\rho g Q} \qquad [8.28]$$

where,

η is the pump efficiency

ω is the angular velocity of the impeller

T is the shaft torque

ρ is the fluid density

Q is the volumetric flow rate through the section

For high-speed waterjets operating at low rpm values, the pump efficiency is usually understood to be in the range of 0.43-0.50 (Macpherson, 2000). In order to estimate the head rise through the pump section, an efficiency of 0.43 was therefore assumed. As discussed previously, the velocity data recorded at the pump section fluctuated a great deal and as a result the head rise through this section was a rough estimate, at best. The head losses determined throughout the waterjet unit are summarised in Table 8-5.

Table 8-5. Waterjet head losses

h_L	Head Loss	
$h_{L0\text{-}1}$	**0.2323**	**m**
$h_{L1\text{-}2}$	**0.3704**	**m**
$h_{L2\text{-}3}$	**0.0492**	**m**
$h_{3\text{-}5\ (rise)}$	**-1.976**	**m**
$h_{5\text{-}6}$	**0.0958**	**m**
$h_{6\text{-}7}$	**1.0973**	**m**

Figure 8-33 shows a plot of the normalised energy flux. The results are similar to those published by Kruppa et al. (1996) in both shape and magnitude, but there are obvious differences between the numerical and experimental values. As expected, the largest

discrepancies exist at the pump (station 3 and station 5), where measured velocities were suspect. Improved velocity measurements at the pump face and pump exit would improve confidence in the experimental results.

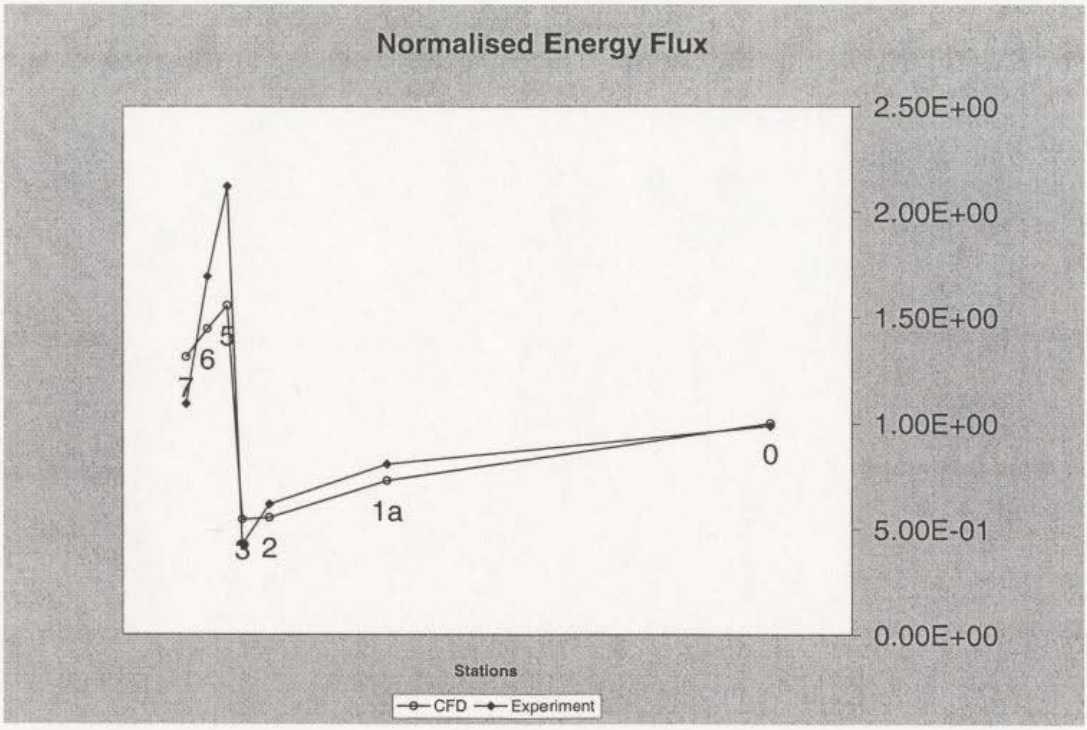

Figure 8-33. Normalized energy flux

The momentum flux calculations for the wind tunnel experiment are summarised in Table 8-6 and Table 8-7, and the full-scale results for the waterjet operating in seawater are shown in Table 8-8 and Table 8-9.

Table 8-6. Wind tunnel momentum flux calculations

ITTC Momentum Flux Calculations (Wind Tunnel)				
	CFD		Experiment	
ρair	1.19E+00	kg/m^3	1.19E+00	kg/m^3
Volume Flowrate (QJ)	2.53E-01	m^3/s	2.50E-01	m^3/s
Capture Width (b)	4.68E-01	m	4.68E-01	m
Station 1a				
ITTC Capture height	1.30E-01	m	1.15E-01	m
M1	1.26E+00	N	1.34E+00	N
E1	2.73E+00	W	3.03E+00	W
Station 7				
Volume Flowrate	2.53E-01	m^3/s	2.50E-01	m^3/s
radius	1.17E-01	m	1.17E-01	m
M7	1.69E+00	N	1.65E+00	N
E7	4.91E+00	W	4.62E+00	W
Station 0				
Ship Speed (V)	5.00E+00	m/s	5.00E+00	m/s
E0	3.75E+00	W	3.70E+00	W
Summary of Energy Flux				
Station #	CFD		Experiment	
0	3.75E+00	W	3.70E+00	W
1a	2.73E+00	W	3.03E+00	W
2	2.08E+00	W	2.32E+00	W
3	2.04E+00	W	1.60E+00	W
5	5.82E+00	W	7.94E+00	W
6	5.41E+00	W	6.34E+00	W
7	4.91E+00	W	4.08E+00	W

Table 8-7. Propulsion performance calculations

Propulsion Performance Calculations (Wind Tunnel)				
	CFD		Experiment	
Change of Momentum				
ρsaltwater	1.03E+03	kg/m^3	1.03E+03	kg/m^3
a	5.00E+00	degrees	5.00E+00	degrees
DM	4.23E-01	N	3.09E-01	N
Rs	3.66E+02	N	2.67E+02	N
Effective Jet System Power				
PJSE	2.18E+00		1.59E+00	
Elevation Power				
g	9.81E+00	m/s^2	9.81E+00	m/s^2
hJ	0.00E+00	m	0.00E+00	m
rgQJhJ	0.00E+00	kg m^2 s^-3	0.00E+00	kg m^2 s^-3
Internal Losses				
z13	1.85E-01		3.86E-01	
z57	1.86E-01		9.45E-01	
Losses (P_{IL})	1.60E+00		5.29E+00	
Effective Pump Power				
P_{PE}	3.78E+00	W	6.88E+00	W
Increase in Mean Total Head				
H_{35}	1.29E+00	m	2.54E+00	m

Table 8-8. Full-scale momentum flux calculations

Full Scale ITTC Momentum Flux Calculations				
	CFD		Experiment	
$\rho_{seawater}$	1.03E+03	kg/m^3	1.03E+03	kg/m^3
Volume flowrate (Q_J)	2.53E-01	m^3/s	2.50E-01	m^3/s
Capture width (b)	4.68E-01	m	4.68E-01	m
Station 1a				
ITTC capture height	1.30E-01	m	1.15E-01	m
M1	1.10E+03	N	1.16E+03	N
E1	2.37E+03	W	2.62E+03	W
Station 7				
Volume flowrate	2.53E-01	m^3/s	2.50E-01	m^3/s
radius	1.17E-01	m	1.17E-01	m
M7	1.47E+03	N	1.43E+03	N
E7	4.25E+03	W	4.00E+03	W
Station 0				
Ship speed (V)	5.00E+00	m/s	5.00E+00	m/s
E0	3.24E+03	W	3.20E+03	W
Summary of Energy Flux				
Station #	CFD		Experiment	
0	3.24E+03	W	3.21E+03	W
1a	2.37E+03	W	2.62E+03	W
2	1.80E+03	W	2.01E+03	W
3	1.77E+03	W	1.38E+03	W
5	5.04E+03	W	6.88E+03	W
6	4.68E+03	W	5.49E+03	W
7	4.25E+03	W	3.54E+03	W

Table 8-9. Full-scale propulsion performance calculations

Full Scale Propulsion Performance Calculations				
	CFD		Experiment	
Change of Momentum				
$\rho_{saltwater}$	1.03E+03	kg/m^3	1.03E+03	kg/m^3
a	5.00E+00	degrees	5.00E+00	degrees
DM	3.72E+02	N	2.73E+02	N
R_s	3.72E+02	N	2.73E+02	N
Effective Jet System Power				
PJSE	1.88E+03	W	1.38E+03	W
Elevation Power				
g	9.81E+00	m/s^2	9.81E+00	m/s^2
h_J	3.03E-01	m	3.03E-01	m
rgQ_Jh_J	7.69E+02	W	7.60E+02	W
Internal Losses				
z_{13}	1.85E-01		3.86E-01	
z_{57}	1.86E-01		9.45E-01	
Losses (P_{IL})	1.39E+03		4.58E+03	
Effective Pump Power				
P_{PE}	4.04E+03	W	6.72E+03	W
Increase in Mean Total Head				
H_{35}	1.59E+00	m	2.85E+00	m

The results show that the numerical values of the effective jet system power (PJSE) and elevation power were reasonably close to those obtained through experimentation. The internal losses, effective pump power, and increase in mean total head, however were all much higher in the experiment. The greatest variation occurred over the pump unit, as was expected.

The full-scale pump shaft power, P_{DS}, predicted by the simulation was:

$$P_{DS} = \frac{P_{PES}}{\eta_{PS} \cdot \eta_{inst}} = 10.1kW \qquad [8.29]$$

where, P_{PES} is the effective pump power, η_{PS} is the pump efficiency and η_{inst} is the installation efficiency that accounts for non-uniformities to the pump of the waterjet system (assumed to be 85%).

Similarly, the full-scale pump shaft power, P_{DSe}, obtained from experimental data was:

$$P_{DSe} = \frac{P_{PES}}{\eta_{PS} \cdot \eta_{inst}} = 16.8kW \qquad [8.30]$$

Using the average torque value from the physical experiment (0.11 Nm), the full-scale pump shaft power was verified:

$$P_{DS} = 2\pi Qn\frac{\rho_S}{\rho_M} = 2\pi(0.11N \cdot m)(16.7rps)\frac{1025kg/m^3}{1.185kg/m^3} = 10kW \qquad [8.31]$$

As discussed in Chapter 4, one of the limitations of the momentum flux method is the requirement of assumed pump and installation efficiencies. Large scale testing of the complete waterjet system would improve confidence in full-scale predictions, but the results are encouraging, nonetheless. It is assumed that pump efficiency increases with impeller speed but in order to obtain reasonable estimates for the pump efficiency, further testing is required.

8.10 Summary

Numerical simulations were performed on a waterjet system previously tested in the Memorial University wind tunnel. The simulation showed good correlation with the

experimental flow rate and velocity contours. Insufficient experimental velocity measurements at the pump face and pump exit, however, resulted in unreliable power predictions based on the momentum flux method and did not compare well with the numerical simulation near the pump.

The strength of CFD simulation lies in its ability to predict the flow behaviour of real-world situations. The waterjet simulation predicted the separation observed near the intake roof of real waterjets, and showed good correlation between the traditional method of determining pump shaft power, and modern methods using CFD and the momentum flux method.

9 Conclusions and Recommendations

The objective of this thesis was to predict the performance characteristics of a waterjet using computational fluid dynamics validated by experimental work in a wind tunnel. A similitude analysis of the waterjet system was presented along with a description of the momentum flux method. Physical testing of the waterjet system was discussed, followed by the numerical simulation and application of the momentum flux method that ensued. The remainder of this chapter is concerned with the major conclusions from both the physical experiments and numerical simulations, along with recommendations pertaining to future work.

9.1 Physical Experiments

A revision of the existing waterjet test platform determined that the system stiffness needed improvement and a more suitable impeller was necessary. A number of bracket supports were added to the system to address the stiffness concerns, and a model impeller was fabricated using the laminated object manufacture (LOM) system located at Memorial University. The LOM system was particularly suitable for wind tunnel testing, as it is an inexpensive method of manufacturing large models that do not experience heavy loading, or require watertightness. Modifications in these areas resulted in much less system vibration and noise.

A single wire, constant temperature, hot-wire anemometer was used to record wind velocities at multiple locations throughout the waterjet system. Hot-wire anemometry is a

suitable method for measuring subsonic incompressible continuum flows, but measurements recorded with the single wire were not capable of measuring flows in more than one direction. In areas of high turbulence, such as near the impeller, Laser Doppler Anemometry (LDA) may provide more meaningful results.

Wind velocity data was recorded at multiple locations throughout the waterjet system and produced flow patterns characteristic of waterjets. Flow separation at the inlet showed regions of low speed flow at the top of the inlet duct, and high speed flow near the bottom. Furthermore, a concentrated jet stream was produced at the nozzle outlet and vena contracta, while the boundary layer measurements at the inlet were in good agreement with theoretical predictions.

The testing of waterjets using a wind tunnel is a convenient and economical alternative to traditional testing methods at small scales. The threat of harmful discharge to the laboratory is removed when testing in air and loading on critical components is much smaller. Waterjets can therefore be tested at much larger scales and need not be completely watertight. Testing at large scales provides for much easier access to sections within the waterjet, and intrusive measurement techniques have a smaller relative influence on the flow. A major limitation of the test, however, is the inability of air measurements to provide information pertaining to cavitation.

The physical experiments of this study did not account for the trim and sinkage experienced by real-world prototypes, nor was the wall of the wind tunnel modified to accurately represent the underside of a ship's hull. Pressure changes along the wind tunnel wall, therefore, did not correctly describe the behaviour beneath the hull. In order

to represent the correct behaviour, the waterjet and hull would have to be treated as a single unit, and the geometry of specific hull forms would be necessary.

A substantial amount of data was obtained for the impeller operating at 1000 rpm, and a wind tunnel speed of 5 m/s. The data was necessary for validation of the numerical simulation and could be used to augment further numerical and/or experimental testing.

9.2 Numerical Simulation

Numerical simulations were performed on a full-scale waterjet previously tested in the MUN wind tunnel. The software chosen for the application was CFX 5.6 because of its reputation as a reliable CFD program that has gathered momentum in the treatment of jet flows, turbo machinery, and hull and wake analysis.

The experiment was described in terms of modular components that represented the wind tunnel, waterjet, impeller exit, and jet stream. This permitted individual components to be modified, edited, added, or removed without altering other parts of the mesh. A grid dependence study was carried out on the individual components, and on the system as a whole, until grid independence was achieved. The simulation was validated by good correlation with the volumetric flowrate, velocity contours, and point velocities obtained from the physical tests.

Momentum flux calculations determined that for the impeller operating at 1000 rpm and the vessel moving at 5m/s, the full-scale effective pump power and pump shaft power were 4 kW and 10 kW, respectively. Excellent agreement was established between the

traditional methods of determining pump shaft power and those determined by computational fluid dynamics and the momentum flux method. The method, however, is not without its shortcomings as it relies heavily on an accurate description of flowrate and estimates of pump and installations efficiencies

In addition, the intake capture area obtained through CFD analysis appears to be wider than that recommended by the ITTC, and elliptical rather than rectangular in shape. Further study into the limitations of the momentum flux method may improve confidence in full-scale predictions.

This study demonstrates that although simulation has not usurped the mantle of physical testing as the most accepted method of interpreting real-world behaviour, it serves as a valuable tool for obtaining detailed information at a resolution that is not possible using traditional methods. As the speed and memory capabilities of computers continue to improve, the field of hydrodynamics will move further into the realm of simulation and it's reliance on physical modelling will be reduced. CFD simulation, validated by physical experimentation is an excellent technique for evaluating the performance of waterjets.

9.3 Recommendations for Future Work

Although the results obtained from the numerical simulation were in close agreement with those obtained from physical testing, some of the limitations of the physical experiments were duplicated in the CFD model. In order to improve the accuracy of the physical experiment, the wall of the wind tunnel should be modified at the inlet to reflect

the shape of a typical hull. Moreover, an effort should be made to account for the trim and sinkage of real world vessels.

Hot-wire anemometers are not suitable for measuring high turbulence levels. It is therefore recommended that velocity measurements in areas of high turbulence should be obtained by more appropriate methods, such as Laser Doppler Velocimetry.

Single wire anemometers can only account for one component of the three-dimensional velocity vector. In order to fully understand the nature of the flow throughout the waterjet, a description of the velocity at the inlet would be beneficial. It is recommended that multiple wire anemometers obtain velocity measurement at the inlet.

In order to completely describe the waterjet under realistic operating conditions, a test program consisting of a number of impeller speeds, and wind tunnel velocities is necessary. Destructive testing of the model impeller is therefore required to establish its physical limitations. Should the impeller fail at high rpm values, a stronger impeller should be constructed using alternate means and/or materials.

The information obtained from the improved physical experiment will go a long way in improving the accuracy of the numerical experiment. With detailed data at the impeller, the numerical model would benefit from rotating components. The modular design of the existing numerical model is perfectly suited to the addition or subtraction of components, and a comparison between numerical simulations would be readily available. It is therefore recommended that future numerical simulations include a rotating impeller

validated by three- dimensional velocity measurements. An accurate computer model would then be able to address any concerns about cavitation at the impeller.

10 References

Acheson, D. J., Elementary Fluid Dynamics, New York, Oxford Press, 1998.

Alexander, K. "The Waterjet as an Engine Dynamometer" International Symposium on Waterjet Propulsion Latest Developments, RINA, London, 1994

Allison, J.L.. Marine Waterjet Propulsion. Presented before the Chesapeake Section of the Society of Naval Architects and Marine Engineers, 1992

Allison, J.L., Jiang, C., Stricker, J.G., Athavale, M.M., Kerwin, J., Taylor, T, "Modern Tools for Waterjet Pump Design and Recent Advances in the Field" International Symposium on Waterjet Propulsion, Latest Developments, RINA, Amsterdam, 1998

Allison, J.L., Becnel, A.J., Purnell, J.G, Gorski, J.J, Hoyt III, J.G. and Wilson, M.B., "Research in Waterjet Inlet, Hull, and Jet Interactions", International Conference on Waterjet Propulsion III, RINA, Gothenburg, 2001

Anderson, J. D., Computational Fluid Dynamics: The Basics with Applications, McGraw-Hill, 1995.

Atkins Consultants, Best Practices Guidelines for Marine Applications of Computational Fluid Dynamics, W.S. Atkins Consultants, 2003

Barth, T. J., Jesperson, D. C., "The Design and Application of Upwind Schemes on Unstructured Meshes", AIAA Paper 89-0366, 1989

Bruun. H., Hot-Wire Anemometry: Principles and Signal Analysis, New York, Oxford Press, 1995

Chio, J., Hwang, E., So, H. Y. Kim, B., "An Uncertainty Evaluation for Multiple Measurements by GUM", Accreditation and Quality Assurance, Vol.. 8, no. 3, pp. 13-15 2003.

CFX Limited, "CFX Build", Release 5.6, CFX Limited, Waterloo, Ontario, Canada, 2003

CFX Limited, "Solver Advice", Release 5.6, CFX Limited, Waterloo, Ontario, Canada, 2003

CFX Limited, "Solver Manager", Release 5.6, CFX Limited, Waterloo, Ontario, Canada, 2003

CFX Limited, "Solver Modelling", Release 5.6, CFX Limited, Waterloo, Ontario, Canada, 2003

CFX Limited, "Solver Theory", Release 5.6, CFX Limited, Waterloo, Ontario, Canada, 2003

Colebrook, C.F., "Turbulent Flow in Pipes with Particular Reference to the Transition Between Smooth and Rough Pipe Laws", Journal of the Institute of Civil Engineers London, Vol. 11, 1939

Dantec Dynamics "Instruction Manual 55M10 CTA Standard Bridge", Copyright Dantec Dynamics, n. d.

Duplain, E., Royer, H., "Testing of Full Size Waterjet Propulsion System in Wind Tunnel", Undergraduate research submitted to Memorial University, Faculty of Engineering and Applied Science, St. John's, Newfoundland, Canada, 2002.

Dyne, G., Lindell, P., "Waterjet Testing in the SSPA Towing Tank" International Symposium on Waterjet Propulsion Latest Developments, RINA, London, 1994

Fluent Inc., "Introduction to CFD Analysis", Fluent Incorporated, 2003

Griffith-Jones, G., Bowen, A. J., "Modelling of the flow through a 3d curved Intake of a Waterjet Propulsion Unit and a Planing Hull", 11th Australasian Fluid Mechanics Conference, University of Tasmania, Hobart, Australia, 1992

Harvald, Sv., Aa., Resistance and Propulsion of Ships, New York, John Wiley & Sons, 1983.

Hastings, C. Approximations for Digital Computers, Princeton, NJ, Princeton Press, 1985

Hu, P., Zangeneh, M., "CFD Calculation of the Flow through a Waterjet Pump", International Conference on Waterjet Propulsion III, RINA, Gothenburg, 2001.

Huntsman, I., Hothersall, R., "Development of Quasi 3D Methods and 3D Flow Solvers for the Hydrodynamic Design of Waterjets", International Conference on Waterjet Propulsion III, RINA, Gothenburg, 2001

ITTC 1996; "Supplement to the Report of the Waterjets Group", 21st International Towing Tank Conference, Trondheim, Norway, 1996

ITTC 2002, "The Specialist Committee on Validation of Waterjet Test Procedures Final Report and Recommendations to the 23rd ITTC", 23rd International Towing Tank Conference, Venice, 2002

Jørgensen, F. E., Hot to Measure Turbulence with Hot-Wire Anemometers – A Practical Guide, Denmark, Dantec Dynamics, 2002.

Karassik, I. J., Pump Handbook, 3rd Edition, McGraw-Hill, 2003

Kempf & Remmers Technical Data R 25/8, Copyright Kempf & Remmers, n.d.

Kruppa, C., et al., "Report of the Specialist Committee on Waterjets Final Report and Recommendations to the 21st ITTC", 21st International Towing Tank Conference, Trondheim, Norway, 1996

Leveque, R. J., Finite Volume Methods for Hyperbolic Problems, Cambridge University Press, 2002

Macpherson, D. H., "Solution of Commercial Waterjets, New Performance Coefficients Point the Way", Society of Naval Architects and Marine Engineers, New England Section, Feb. 2000

McNeel, R., Rhinoceros Help Manual, copyright Robert McNeel and Associates, 2002

Moran, M. J., Shapiro, H. N., Fundamental s of Engineering Thermodynamics, New York, John Wiley & Sons, 1996.

Munson, B. R., Young, D. F., Okiishi, T. H., Fundamentals of Fluid Mechanics, 3rd Edition, New York, John Wiley & Sons, 1998.

Mununga, L., Huntsman, I, Hothersall, R., "Effects of Splitter Plate and Screen Grid on Waterjet Intake Flow", 13th Australasian Fluid Mechanics Conference, Monash University, Melbourne, Autralia, 1998

Nayyar, Mohinder, Piping Handbook, 7th Edition McGraw-Hill, 2002

Patankar, S. V., Numerical Heat Transfer and Fluid Flow, New York, Hemisphere Publishing Corporation, 1980.

Reeves, P.E., Codd, R.C. "Surface Deviation Modelling of LMT Processes – a Comparative Analysis", Proc. 3rd European Conference on Rapid Prototyping and Manufacturing, Nottingham, 1994

Reynolds, O. "On the Dynamical Theory of Incompressible Viscous Fluids and the Determination of the Criterion", Philos. Trans. R. Soc. London, Ser. A, 186, pp. 123-164, 1895

Rhie, C.M. and Chow, W.L. "A Numerical Study of the Turbulent Flow Past an Isolated Airfoil with Trailing Edge Separation", AIAA Paper 82-0998, 1982

Roache, P.J., Fundamentals of Computational Fluid Dynamics, Albuquerque, New Mexico, Hermosa Publishers, 1998

Roberts, J.L., Walker, G. J., "Boundary Layer Ingestion Effects in Flush Waterjet Intakes" International Symposium on Waterjet Propulsion, Latest Developments, RINA, Amsterdam, 1998

Seil, G.J., "The Effect of the Shaft, Shaft Rotation and Scale on the Flow in Waterjet Inlets", International Conference on Waterjet Propulsion III, RINA, Gothenburg, 2001

Sharp, J. J., Moore, E. "Partial Analysis and Matrix Methods", International Journal of Math Education Science and Technology, Vol. 14, no. 4, pp. 393-402, 1982

Shaw, C. T., Using Computational Fluid Dynamics, Upper Saddle River NJ, Prentice Hall, 1992.

Shellabear, M., "Model manufacturing Processes – State of the Art in Rapid Prototyping", Raptec Task 4.2, Report 1, 1998

Speziale, C. G. "Analytical Methods for the Development of Reynolds-Stress Closure in Turbulence", Annual Review of Fluid Mechanics, Annual Reviews Inc, 1991

Stainback, P.C., "Review of Hot-Wire Anemometry Techniques and the Range of their Applicability for Various Flows", Electronic Journal of Fluids Engineering, Dec 1996, scholar.lib.vt.edu/ejournals/JFE/data/ JFE/DB96-DEC/S&N/hot-wire.pdf

Sutardi, "Effect of Different Shaped Transverse Grooves on a zero Pressure Gradient Turbulent Boundary Layer", PhD Thesis Submitted to the Memorial University of Newfoundland, Faculty of Engineering and Applied Science, St. John's, Newfoundland, Canada, 2002

Thornhill, E., "Development of Waterjet Testing Techniques", Thesis Submitted to the Memorial University of Newfoundland, Faculty of Engineering and Applied Science, St. John's, Newfoundland, Canada, 1999

Thornhill, E., "Application of a General CFD Code to Planing Craft Performance", PhD Thesis Submitted to the Memorial University of Newfoundland, Faculty of Engineering and Applied Science, St. John's, Newfoundland, Canada, 2002

Thornhill, E. "Ocean Marine Hydrodynamics Lecture Notes", Engr 9015 Ocean Marine Hydrodynamics, Memorial University, Fall Term, 2003

Turgay A, Salim, H, Nadir, A,. "Surface Absorption, Surface Roughness, and Formaldehyde Emission of Turkish MDF". Forest Products Journal, Vol.50(6):45-49. June 2000.

Turnock S. R., Hughes, A. W., "Evaluation of a CFD Code for Investigating Hull-Waterjet Flow Interaction". International Conference on Power, Performance & Operability of Small Craft, RINA, Southampton, UK, 1997

Verbeek, R., Bulten, N., "Recent Developments in Waterjet Design" International Symposium on Waterjet Propulsion, Latest Developments, RINA, Amsterdam, 1998

Veersteeg, H. K., Malalasekera, W., An Introduction to Computational Fluid Dynamics, Harlow, England, 1995.

Watson, S.J.P, "The Use of CFD in Sensitivity Studies of Inlet Design" International Symposium on Waterjet Propulsion, Latest Developments, RINA, Amsterdam, 1998

Widmark, C., Gustafsson, L.T.. "3-dimensional CFD calculations on a complete waterjet unit". International Conference on Power, Performance & Operability of Small Craft, RINA Southampton, UK, 1997

Wilcox, D. C., Turbulence Modelling for CFD, DCW Industries, 2000

Ziegler, M., "The Construction of a Hot-Wire Anemometer with Linear Scale and Negligible Lag", Proc. R. Ned Akad. Wet15, no. 1, 1934

Appendix A

Engineering Drawings

This Appendix contains the assembly and detail drawings of the original waterjet tested in the Memorial University wind tunnel.

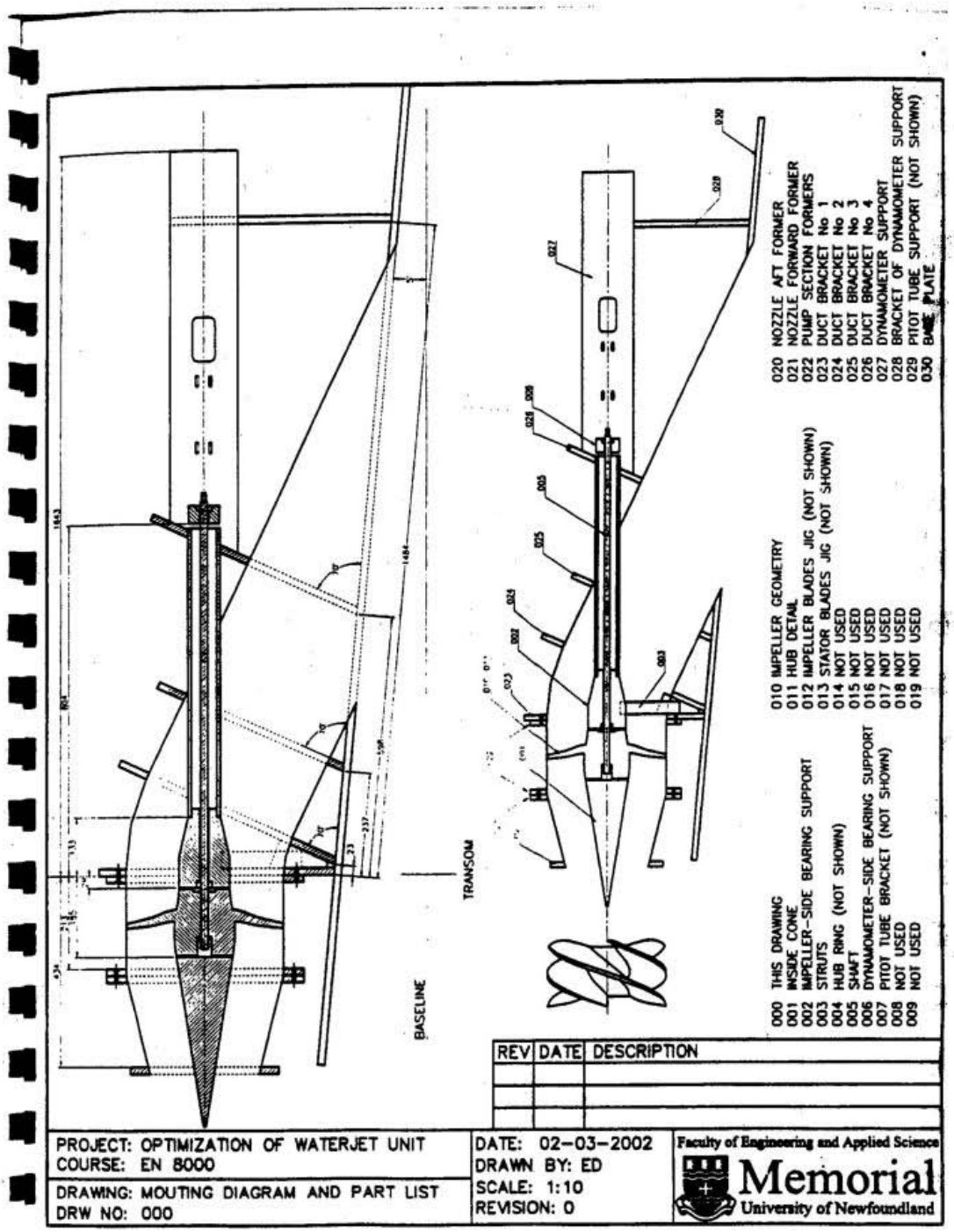

Figure A.1. Mounting diagram and parts list

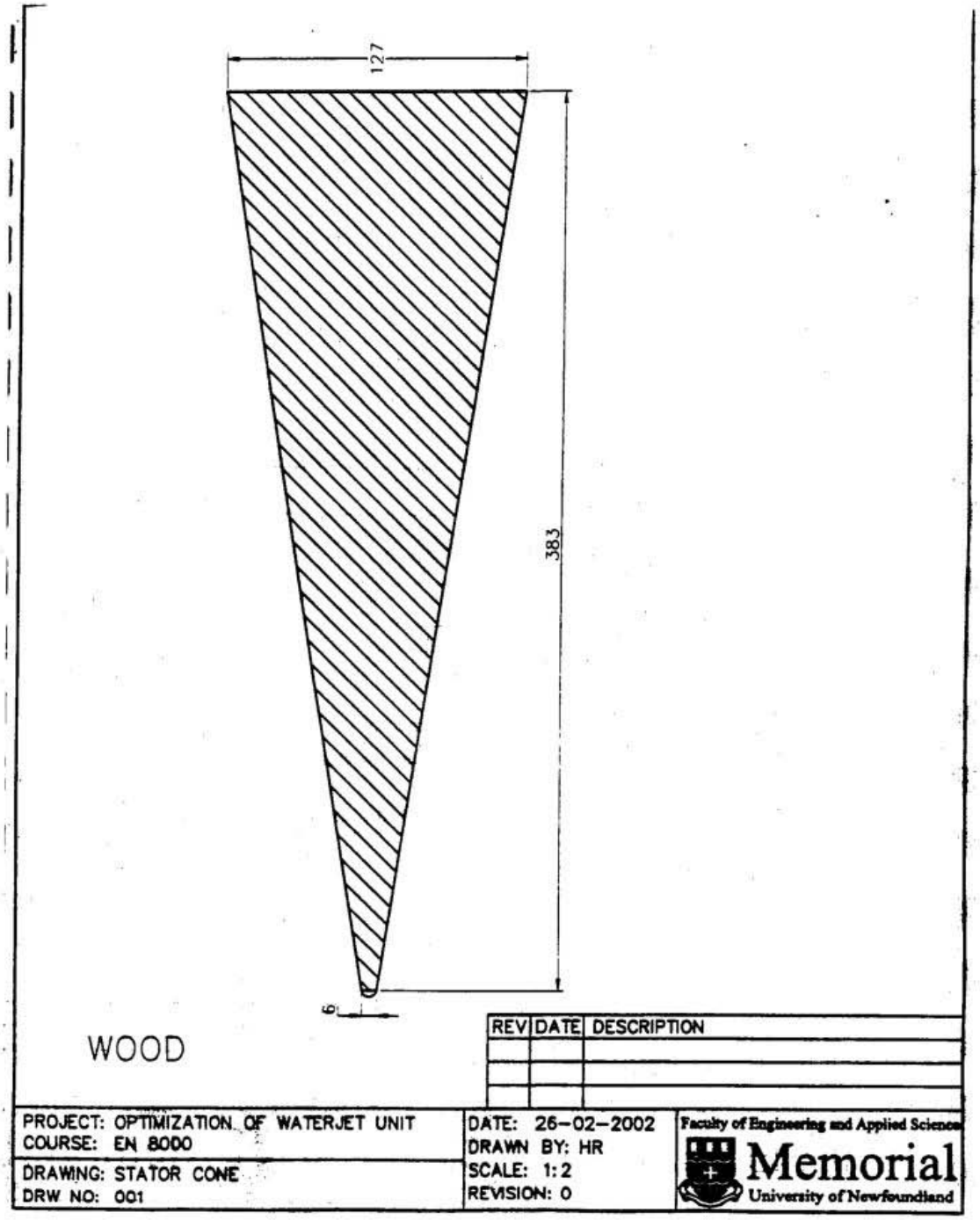

Figure A.2: Stator Cone

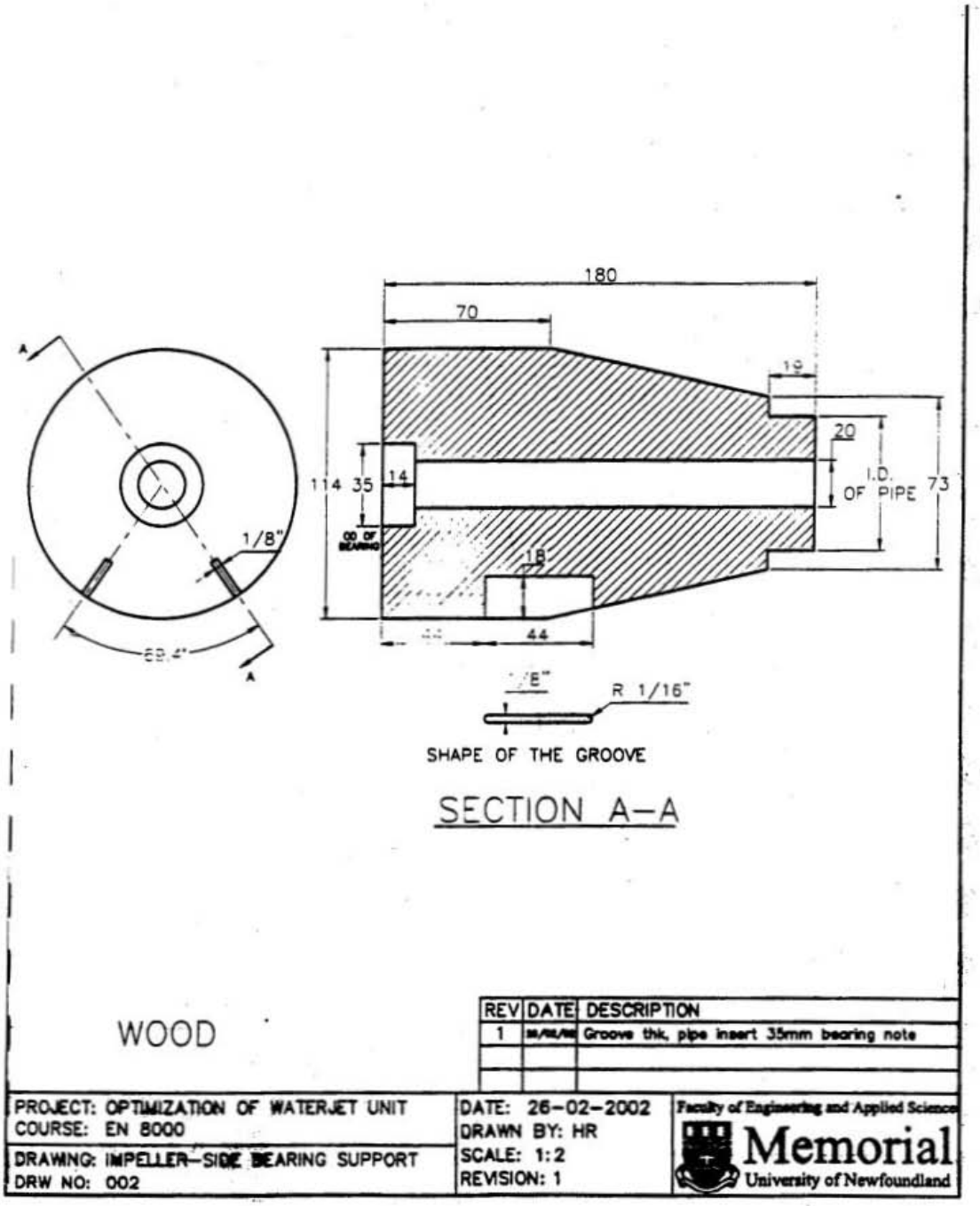

Figure A.3: Impeller – side bearing support

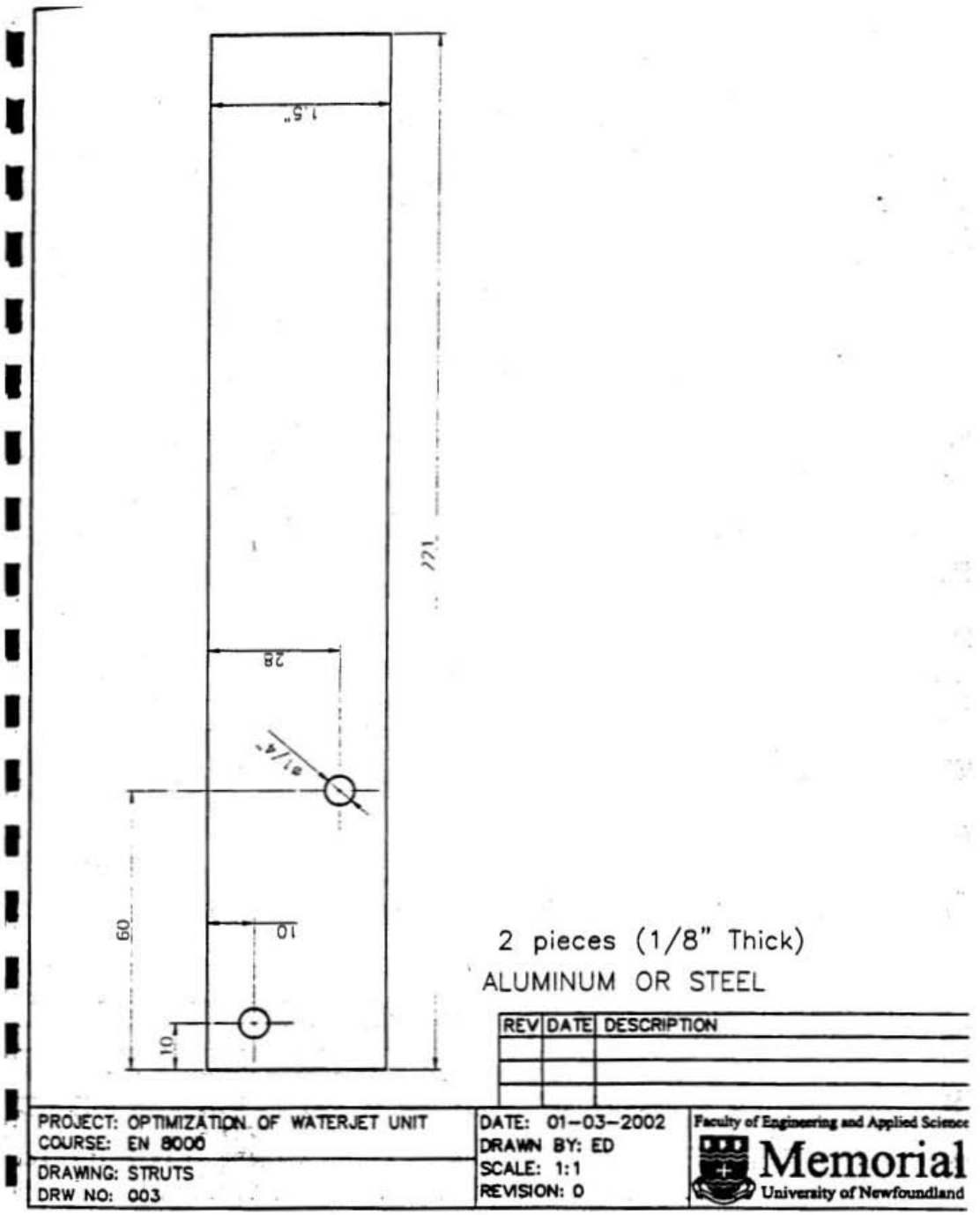

Figure A.4: Struts

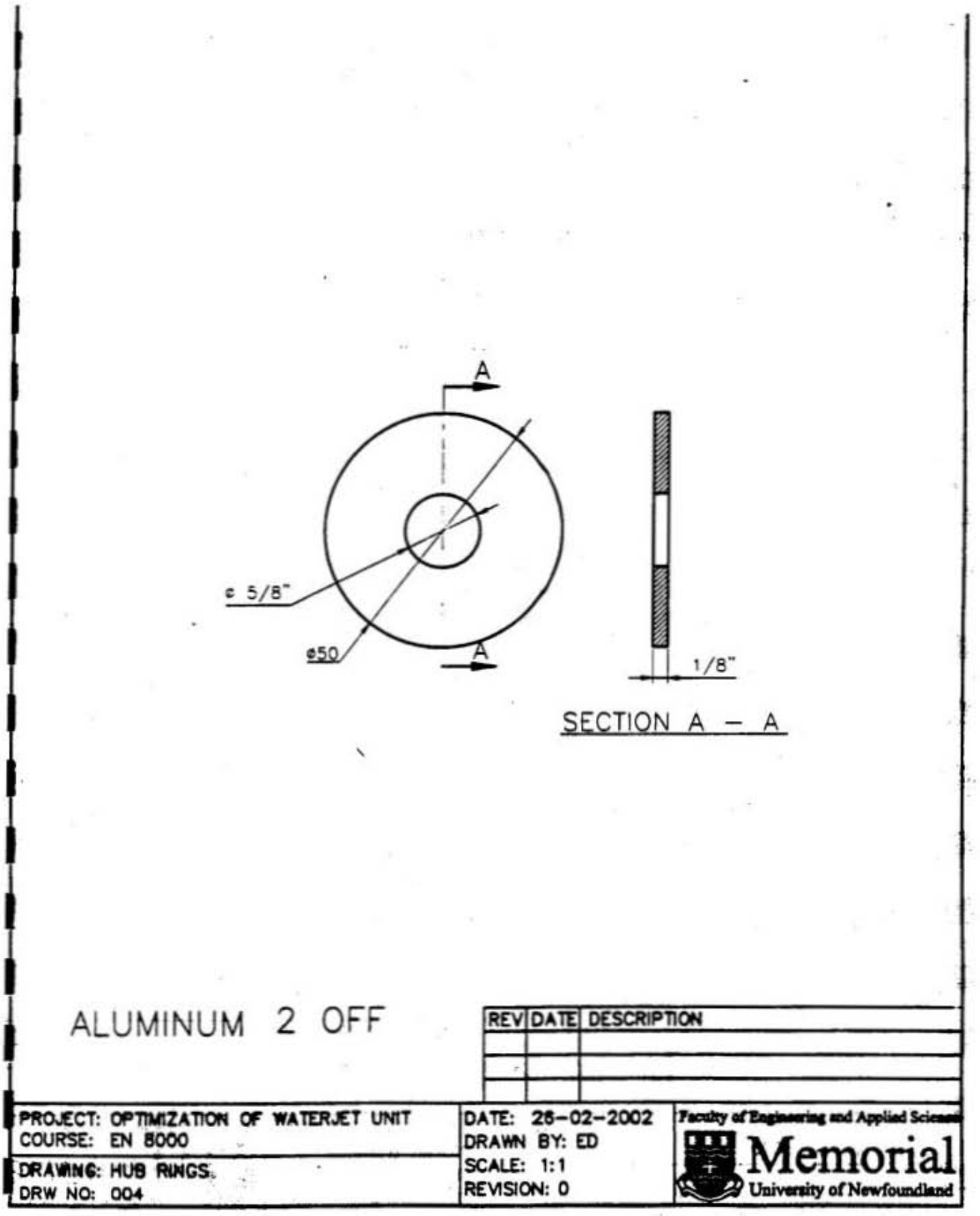

Figure A.5: Hub rings

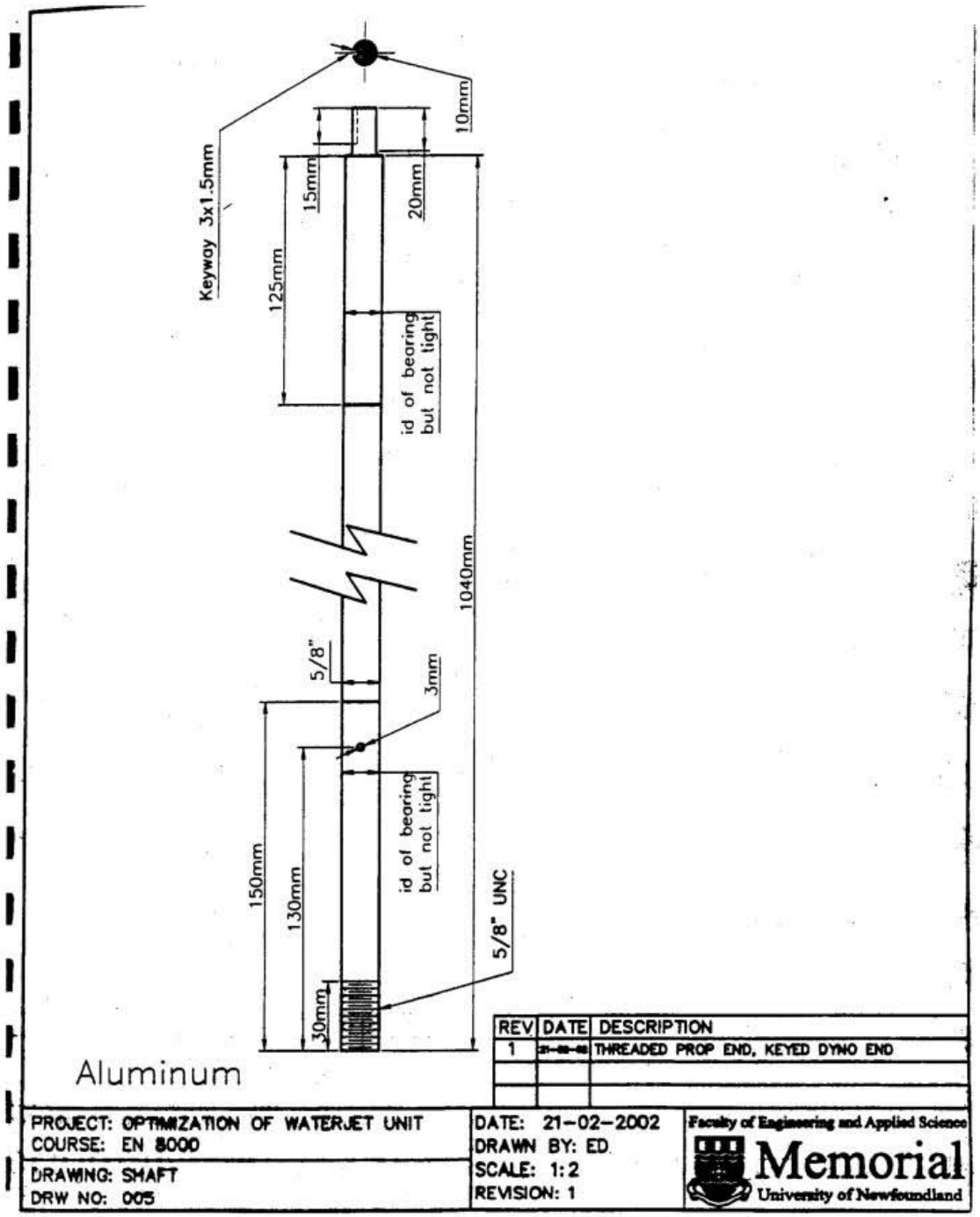

Figure A.6. Shaft

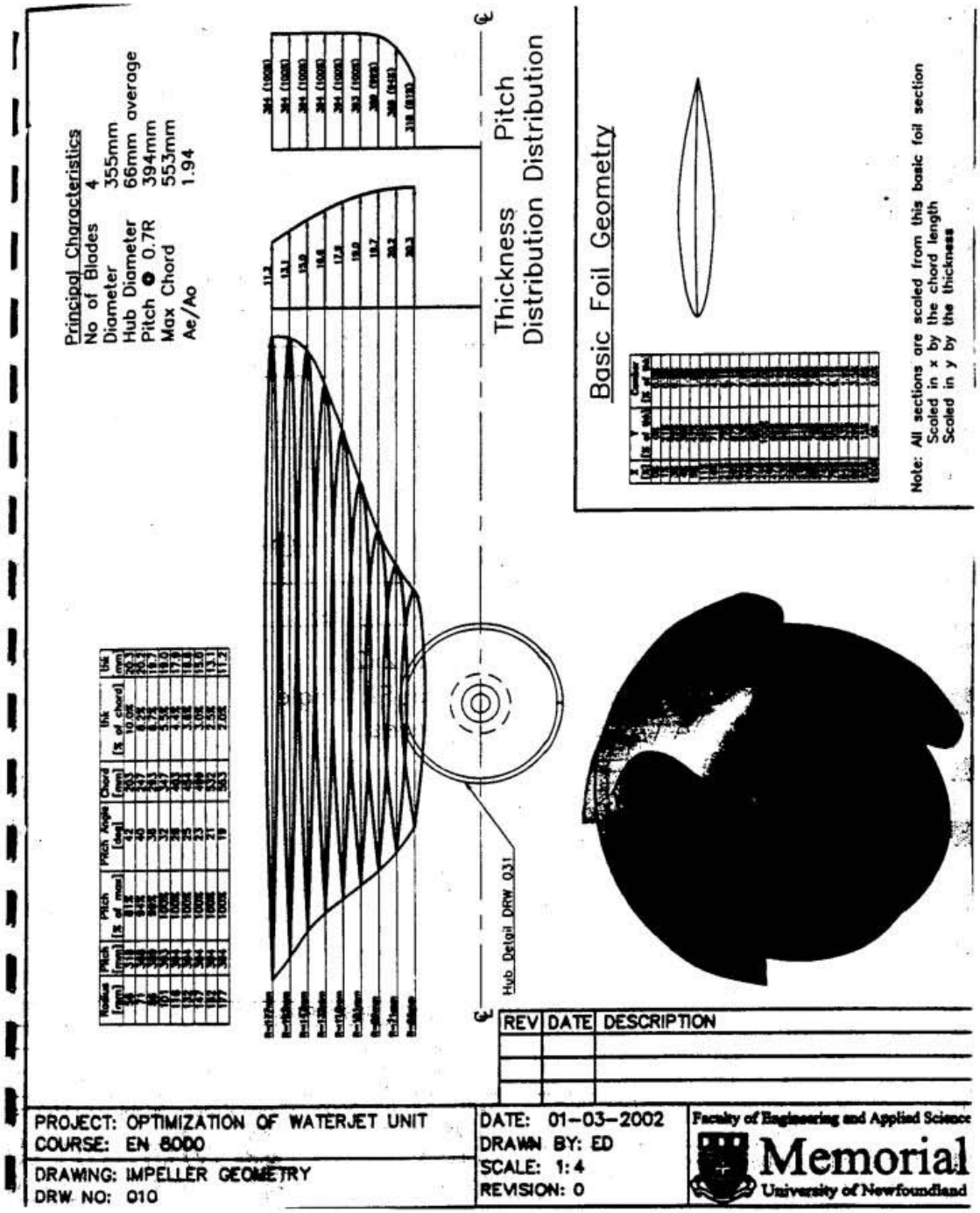

Figure A.7: Impeller geometry

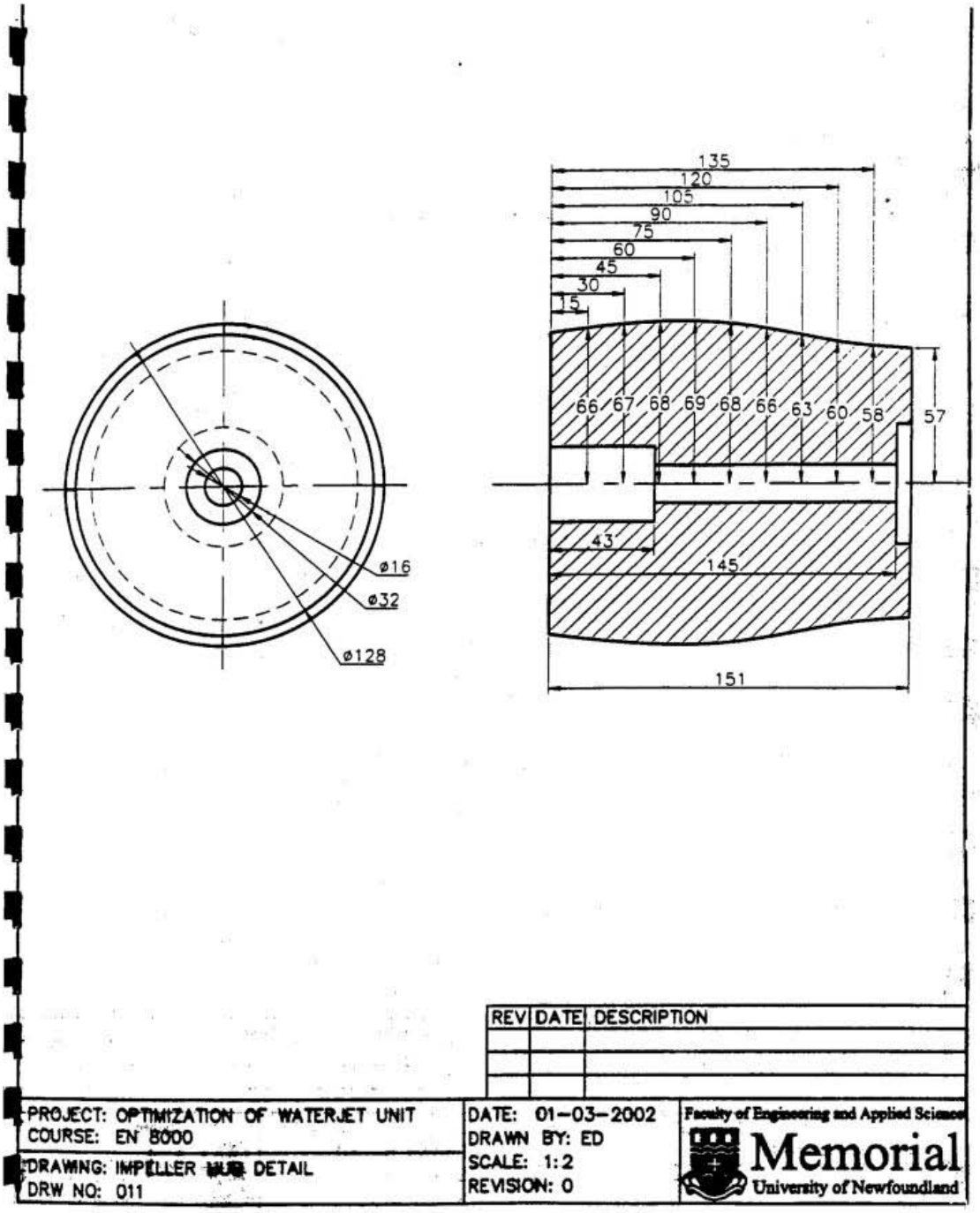

Figure A.8: Impeller hub detail

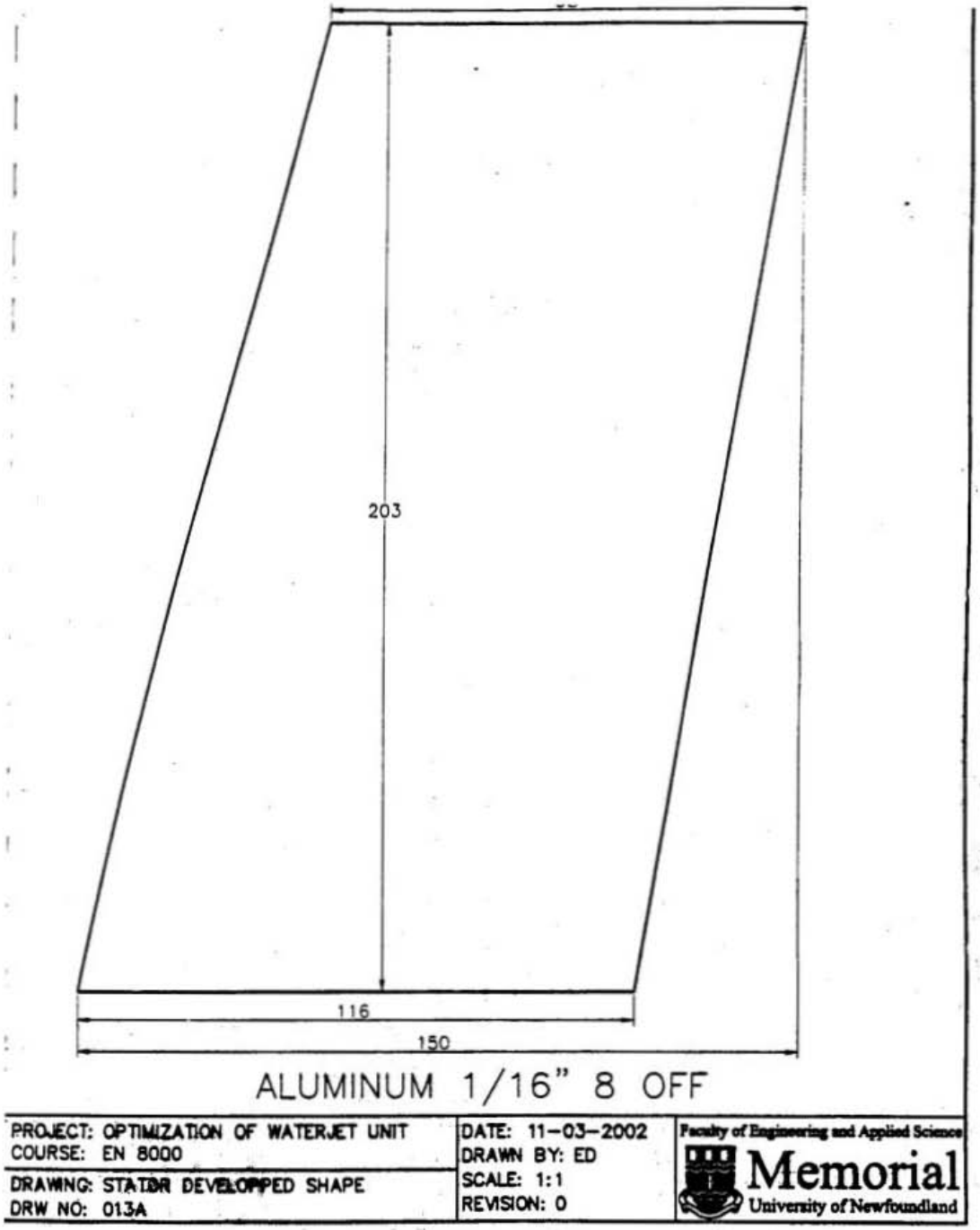

Figure A.9: Stator developed shape

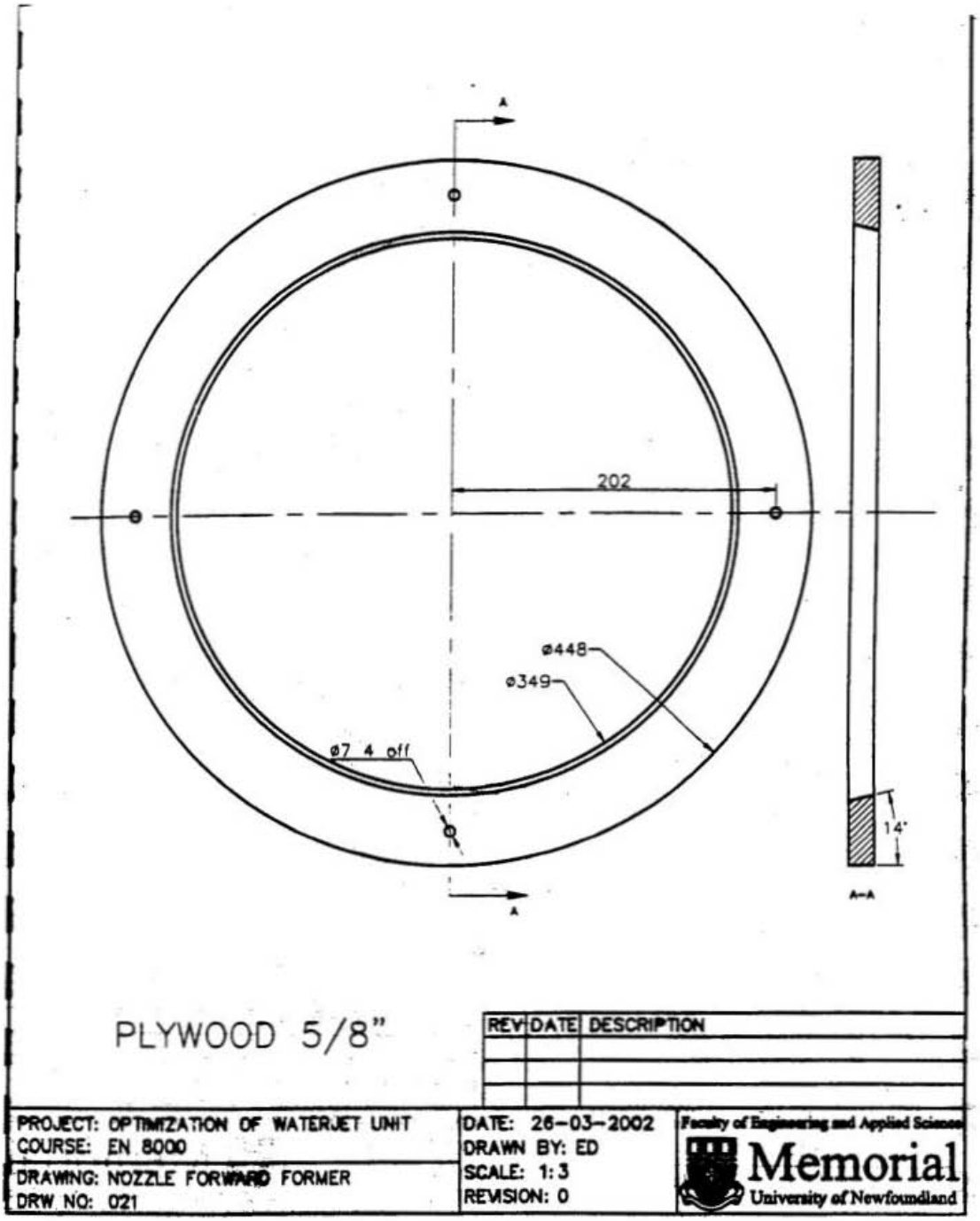

Figure A.10: Nozzle forward former

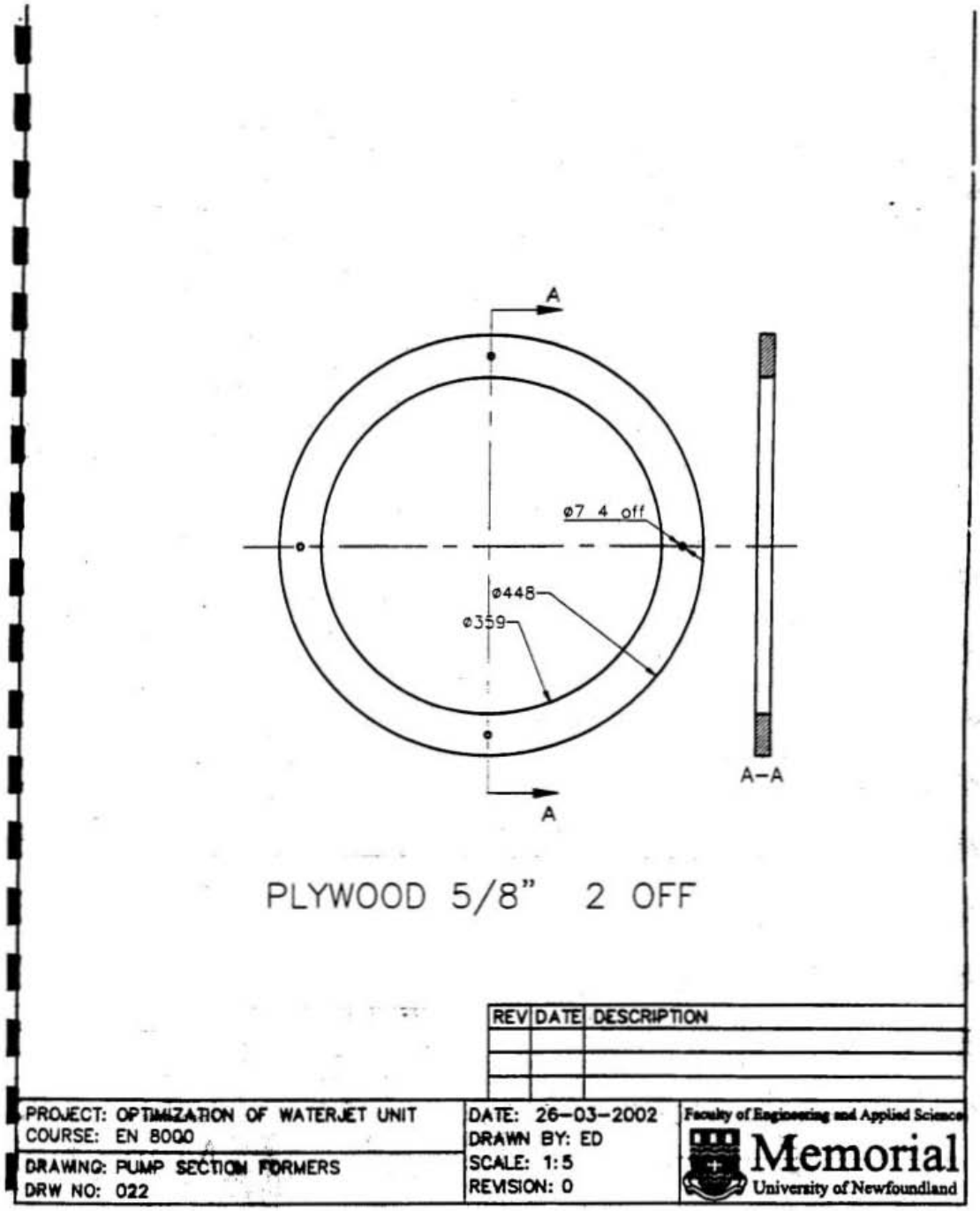

Figure A.11: Pump section formers

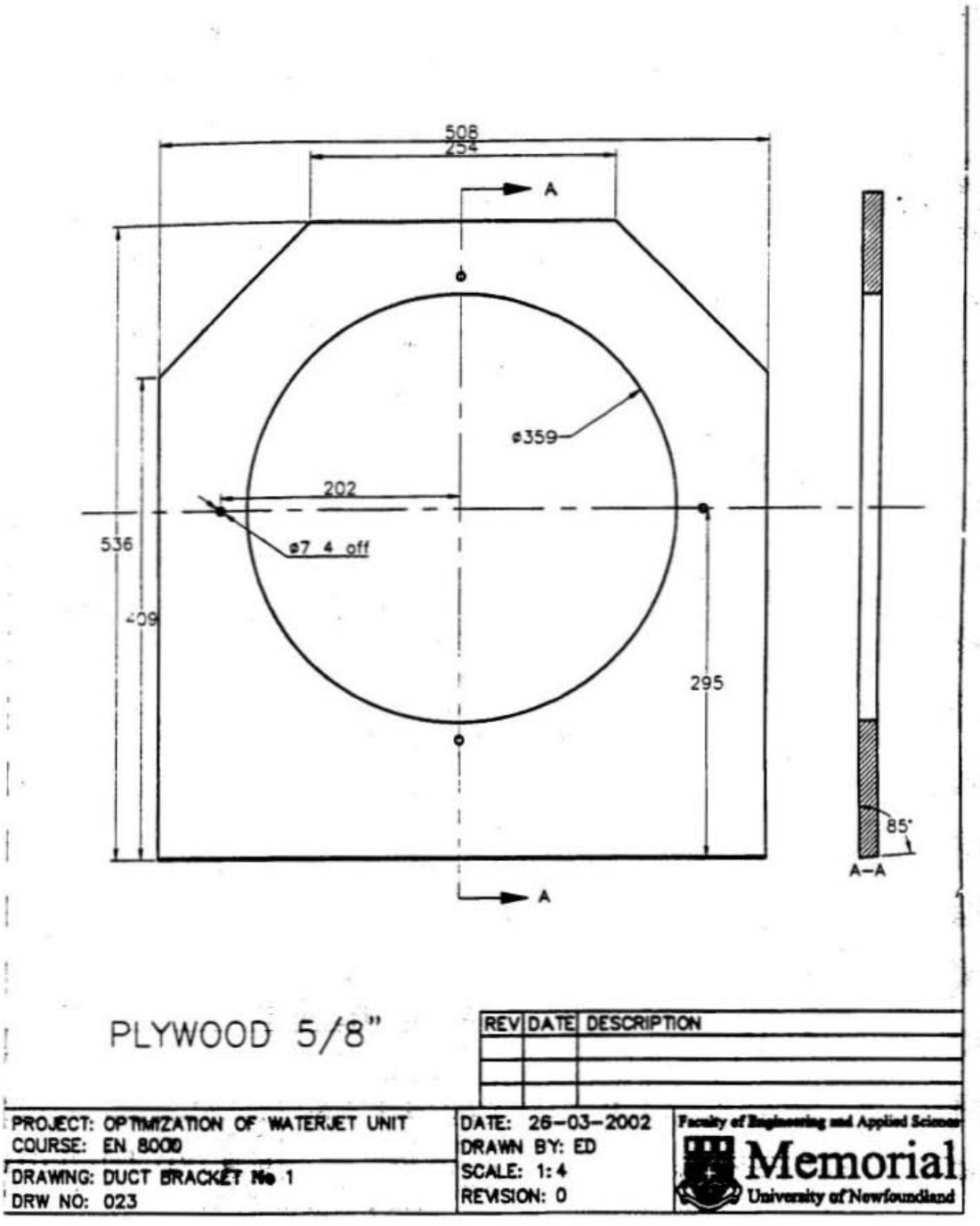

Figure A.12: Duct bracket no. 1

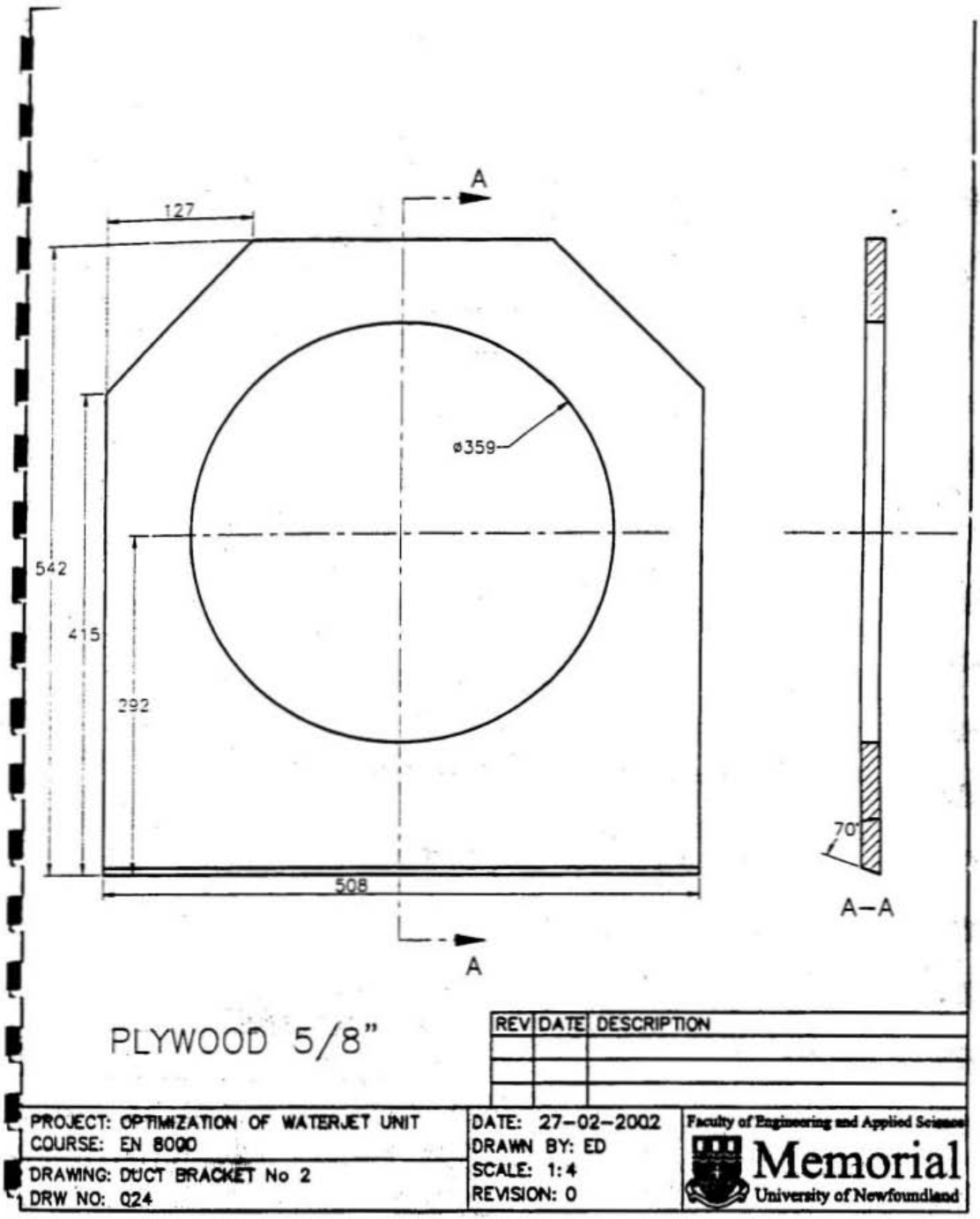

Figure A.13: Duct bracket no. 2

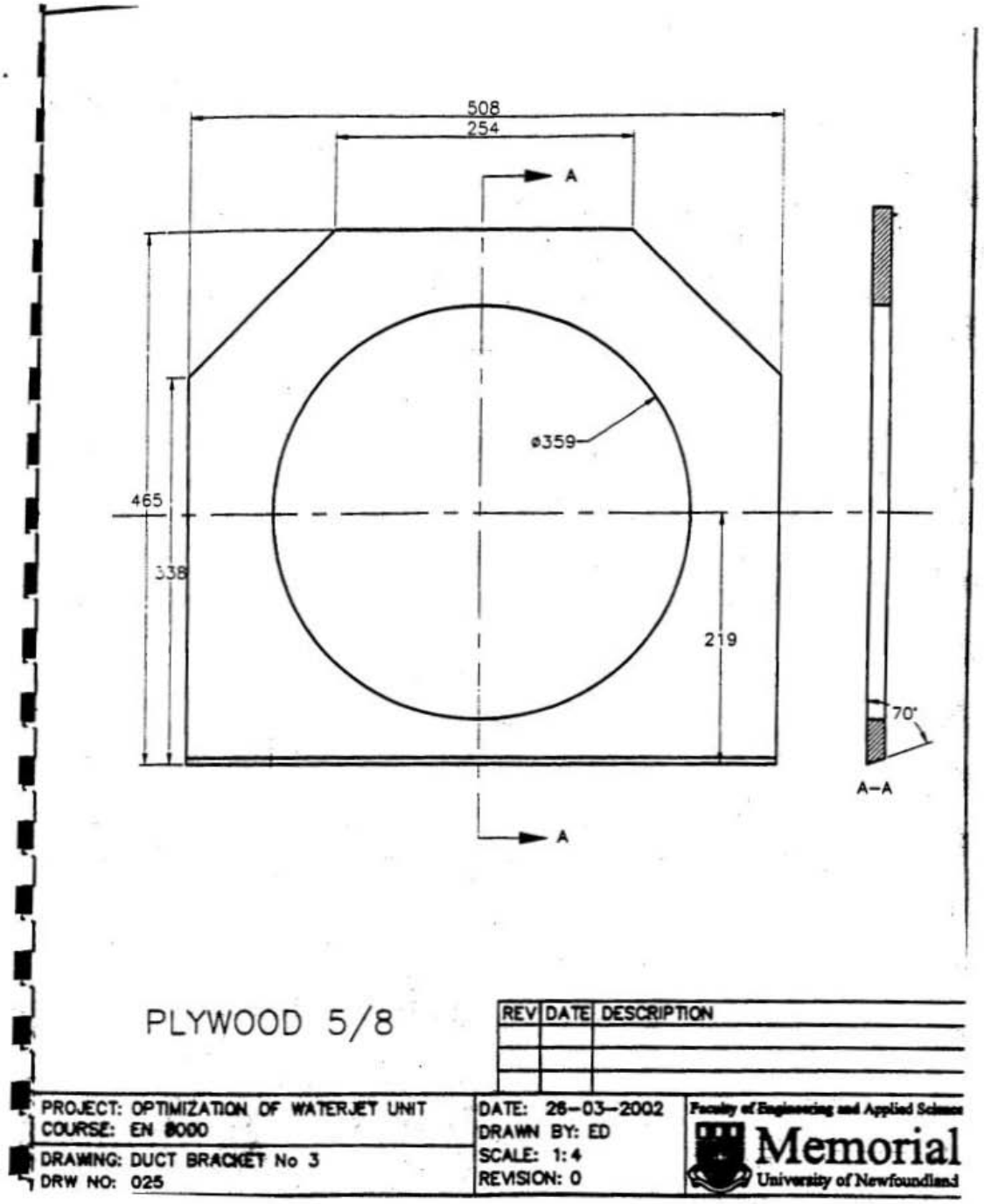

Figure A.14: Duct bracket no. 3

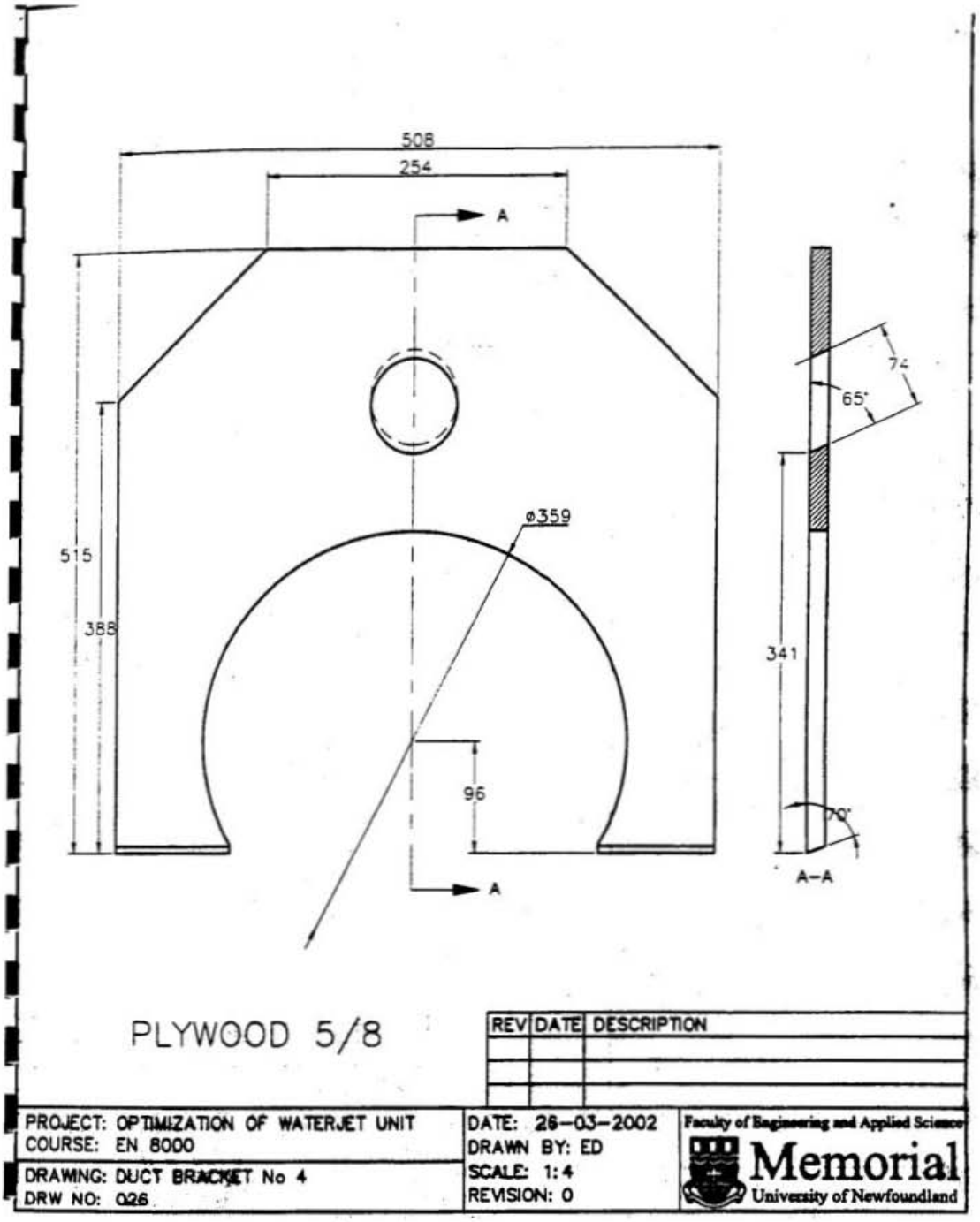

Figure A.15: Duct bracket no. 4

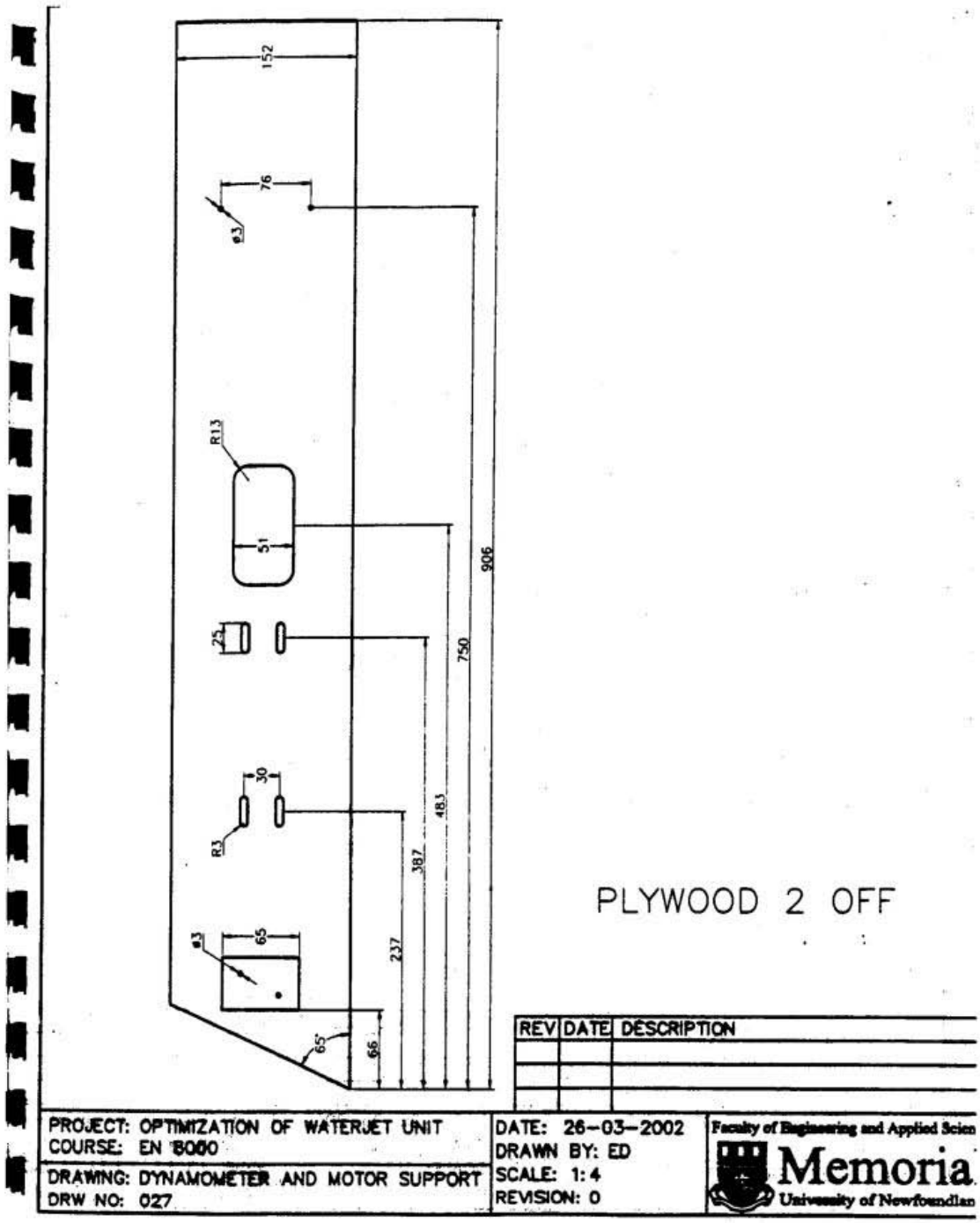

Figure A.16: Dynamometer and motor support

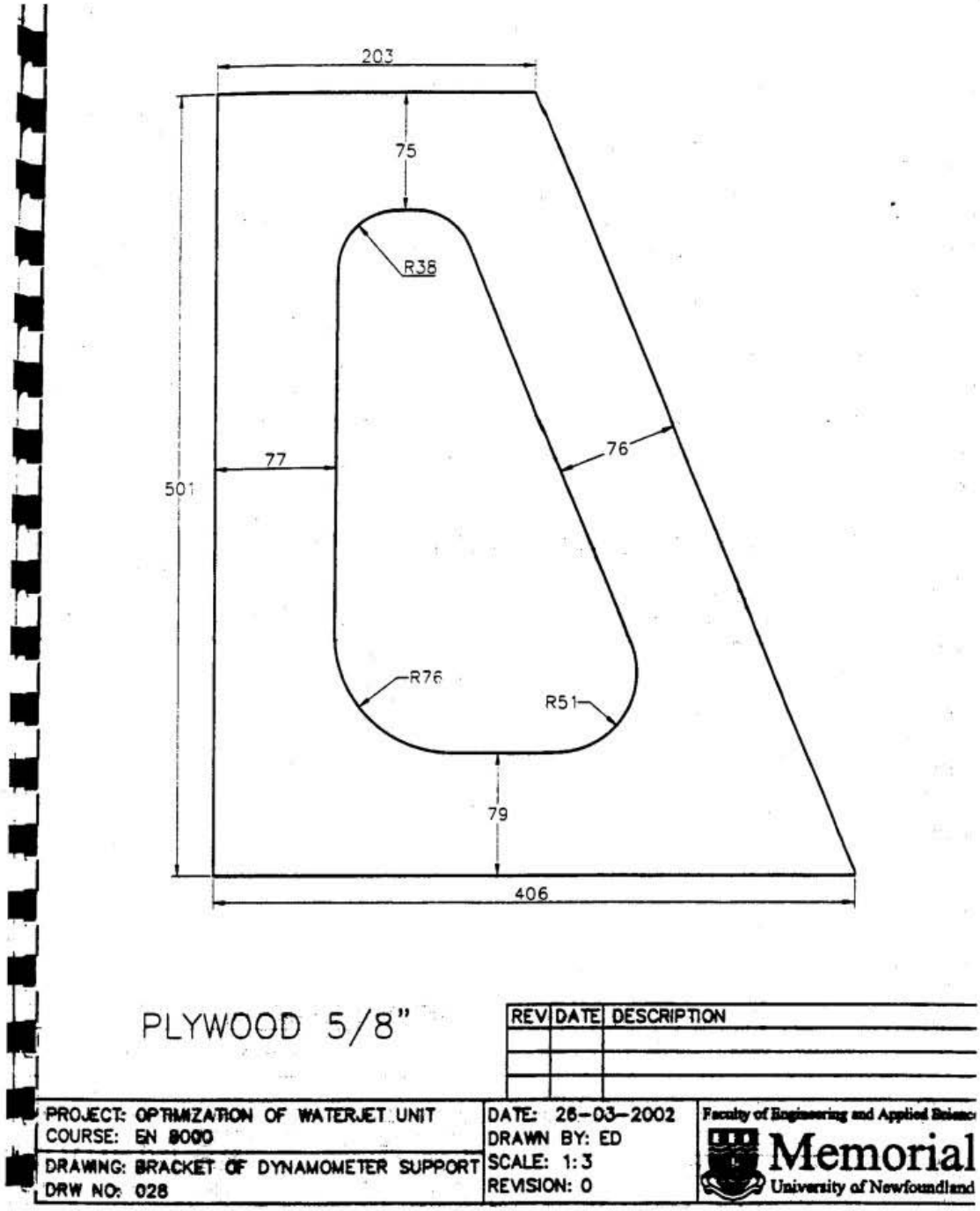

Figure A.17: Bracket of dynamometer support

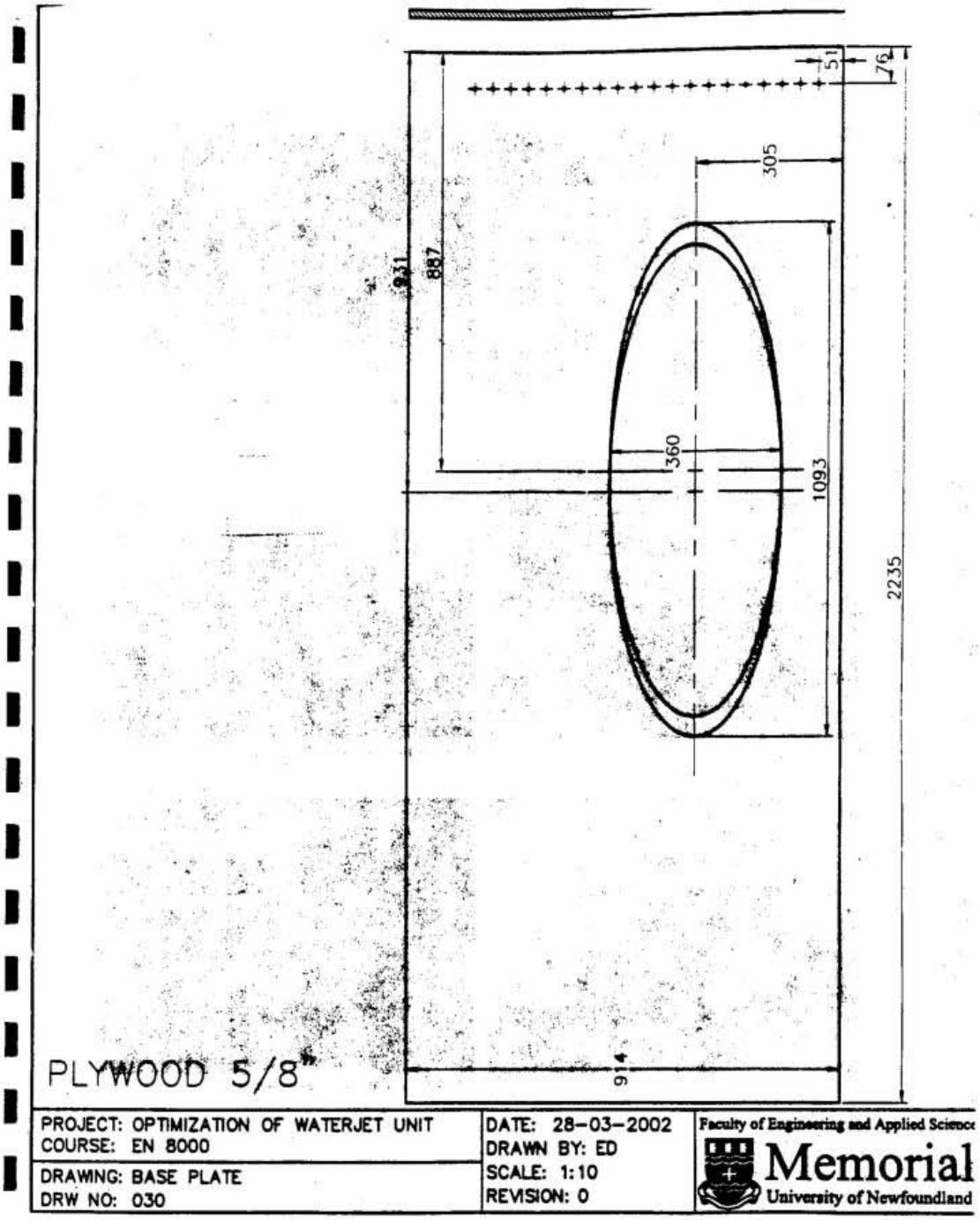

Figure A.18: Base plate

Appendix B

Matlab Routines

```
function varargout = jetcontours(varargin)
% JETCONTOURS Application M-file for jetcontours.fig
%    FIG = JETCONTOURS launch jetcontours GUI.
%    JETCONTOURS('callback_name', ...) invoke the named callback.

% Last Modified by GUIDE v2.0 01-Aug-2003 11:20:16

if nargin == 0  % LAUNCH GUI

      fig = openfig(mfilename,'reuse');

      % Use system color scheme for figure:
      set(fig,'Color',get(0,'defaultUicontrolBackgroundColor'));

      % Generate a structure of handles to pass to callbacks, and store
it.
      handles = guihandles(fig);
      guidata(fig, handles);

      if nargout > 0
            varargout{1} = fig;
      end

elseif ischar(varargin{1}) % INVOKE NAMED SUBFUNCTION OR CALLBACK

      try
            if (nargout)
                  [varargout{1:nargout}] = feval(varargin{:}); % FEVAL
switchyard
            else
                  feval(varargin{:}); % FEVAL switchyard
            end
      catch
            disp(lasterr);
      end

end


%| ABOUT CALLBACKS:
%| GUIDE automatically appends subfunction prototypes to this file, and
%| sets objects' callback properties to call them through the FEVAL
%| switchyard above. This comment describes that mechanism.
%|
%| Each callback subfunction declaration has the following form:
%| <SUBFUNCTION_NAME>(H, EVENTDATA, HANDLES, VARARGIN)
%|
%| The subfunction name is composed using the object's Tag and the
%| callback type separated by '_', e.g. 'slider2_Callback',
%| 'figure1_CloseRequestFcn', 'axis1_ButtondownFcn'.
%|
%| H is the callback object's handle (obtained using GCBO).
%|
%| EVENTDATA is empty, but reserved for future use.
```

```
%|
%| HANDLES is a structure containing handles of components in GUI using
%| tags as fieldnames, e.g. handles.figure1, handles.slider2. This
%| structure is created at GUI startup using GUIHANDLES and stored in
%| the figure's application data using GUIDATA. A copy of the structure
%| is passed to each callback.  You can store additional information in
%| this structure at GUI startup, and you can change the structure
%| during callbacks.  Call guidata(h, handles) after changing your
%| copy to replace the stored original so that subsequent callbacks see
%| the updates. Type "help guihandles" and "help guidata" for more
%| information.
%|
%| VARARGIN contains any extra arguments you have passed to the
%| callback. Specify the extra arguments by editing the callback
%| property in the inspector. By default, GUIDE sets the property to:
%| <MFILENAME>('<SUBFUNCTION_NAME>', gcbo, [], guidata(gcbo))
%| Add any extra arguments after the last argument, before the final
%| closing parenthesis.


% --------------------------------------------------------------------
function varargout = station_popup_Callback(h, eventdata, handles,
varargin)

val=get(h,'Value');
selected_string={val};%convert from cell array to string
switch val
case 1
    %The user has selected the first sheet
    [a]=xlsread('C:\Tests\sections.xls','sfree');L=3.5;deltax=.15
    a_xy_in(a,L,deltax)
    % This station requires plotting along the x and y axes
    %Create new function to plot the data in 2D
    TITLE('Free Stream Velocity Profile (5m/s
wind)','FontWeight','bold')
case 2
    [a]=xlsread('C:\Tests\sections.xls','s1a');L=9;deltax=0.25
    a_xy_in(a,L,deltax)
    TITLE('Section 1a Velocity Profile (5m/s
wind)','FontWeight','bold')
case 3
    [a]=xlsread('C:\Tests\sections.xls','s1');L=6.3;deltax=0.25
     a_xy_in(a,L,deltax)
    %aconts_in(a)
    TITLE('Section 1 Velocity Profile (5m/s wind)','FontWeight','bold')
case 4
    [a]=xlsread('C:\Tests\sections.xls','s2');
    shaft_radius=0
    aconts_in(a,shaft_radius)
    TITLE('Section 2 Velocity Contours (1000 RPM, 5m/s
wind)','FontWeight','bold')
case 5
    [a]=xlsread('C:\Tests\sections.xls','s3');
    shaft_radius = 0.057
    aconts_in(a,shaft_radius)
```

```
    TITLE('Section 3 Velocity Contours (1000 RPM, 5m/s
wind)','FontWeight','bold')
case 6
    [a]=xlsread('C:\Tests\sections.xls','s5');
    shaft_radius = 0.057
    aconts_in(a,shaft_radius)
    TITLE('Section 5 Velocity Contours (1000 RPM, 5m/s
wind)','FontWeight','bold')
case 7
    [a]=xlsread('C:\Tests\sections.xls','s6');
    shaft_radius = 0.022217
    aconts_in(a,shaft_radius)
    TITLE('Section 6 Velocity Contours (1000 RPM, 5m/s
wind)','FontWeight','bold')
case 8
    %The user has selected the last sheet
    [a]=xlsread('C:\Tests\sections.xls','s7');
    shaft_radius = 0
    aconts_in(a,shaft_radius)
    TITLE('Section 7 Velocity Contours (1000 RPM, 5m/s
wind)','FontWeight','bold')
case 9
    %The user has selected CFX Station 2
    shaft_radius=0
    [a]=xlsread('C:\Tests\sections.xls','CFX_2');
    CFX_2(a,shaft_radius)
    TITLE('Station 2 Velocity Contours from CFX (1000 RPM, 5m/s
wind)','FontWeight','bold')
case 10
    %The user has selected CFX Station 3
    shaft_radius = 0.057
    [a]=xlsread('C:\Tests\sections.xls','CFX_3');
    CFX_2(a,shaft_radius)
    TITLE('Station 3 Velocity Contours from CFX (1000 RPM, 5m/s
wind)','FontWeight','bold')
case 11
    %The user has selected CFX Station 5
    shaft_radius = 0.057
    [a]=xlsread('C:\Tests\sections.xls','CFX_5');
    CFX_2(a,shaft_radius)
    TITLE('Station 5 Velocity Contours from CFX (1000 RPM, 5m/s
wind)','FontWeight','bold')
case 12
    %The user has selected CFX Station 6
    shaft_radius = 0.022217
    [a]=xlsread('C:\Tests\sections.xls','CFX_6');
    CFX_2(a,shaft_radius)
    TITLE('Station 6 Velocity Contours from CFX (1000 RPM, 5m/s
wind)','FontWeight','bold')
case 13
    %The user has selected CFX Station 7
    shaft_radius = 0
    [a]=xlsread('C:\Tests\sections.xls','CFX_7');
    CFX_2(a,shaft_radius)
    TITLE('Station 7 Velocity Contours from CFX (1000 RPM, 5m/s
wind)','FontWeight','bold')
```

```
end


% --------------------------------------------------------------------
function varargout = file_menu_Callback(h, eventdata, handles,
varargin)

if isempty(get(handles.axes1,'Children'))
    set(handles.print_submenu,'Enable','off')
else
    set(handles.print_submenu,'Enable','on')
end
end



% --------------------------------------------------------------------
function varargout = print_submenu_Callback(h, eventdata, handles,
varargin)

print -f handles.figure1

end
% --------------------------------------------------------------------
function varargout = close_submenu_Callback(h, eventdata, handles,
varargin)

delete(handles.figure1)
end

% --------------------------------------------------------------------
function a_xy_in(a,L,deltax)
clc
a;
x=a(:,1)./1000;
y=a(:,2);
% Theoretical pipe equation is
%U=Wmax(1-r/Rmax)^(1/7)
%Determine Boundary layer thickness
rho=1.23; %kg/m^3
mu = 0.0000179; %dynamic viscosity of air
Umax1 =max(y);
Rx = rho*Umax1*L/mu;
delta = L*0.370/(Rx^(1/5));
theo_x=linspace(0,delta,100)
Utheo=Umax1*(x./delta).^0.143;Utheo2=Umax1*(theo_x./delta).^0.143;
%We just want the values up to the boundary layer.
% so we locate the indices for the values less than delta
i=find(x<delta+0.035);
%create a table to compare the experimental with theoretical
perc = 100*(Utheo-y)./Utheo;
disp('     X     Experimental  Theo      Diff')
table = [x(1:max(i)) y(1:max(i)) Utheo(1:max(i)) y(1:max(i))-
Utheo(1:max(i))];
disp(table)
%-----------------------------------------------------------------
%--       Plot of only experimental and Theoretical             --
```

```
%-----------------------------------------------------------------
figure
plot(x(1:max(i)),y(1:max(i)),'o-',theo_x,Utheo2,'r','LineWidth',2)
grid on
legend('Raw Data','Theoretical',0)
XLABEL('Horizontal Distance from Wall [m]','FontWeight','bold')
YLABEL('Velocity [m/s]','FontWeight','bold')

% ----------------------------------------------------------------------
function aconts_in(a,shaft_radius)
clc
x=a(:,1)/1000
y=a(:,2)/1000
z=a(:,3);
average_sample_velocity=mean(z)
ti = -.175:.001:.175;
[XI,YI] = meshgrid(ti,ti);
ZI = griddata(x,y,z,XI,YI,'cubic');
average_fitted_velocity=nanmean(nanmean(ZI)')
max_fitted_velocity=nanmax(nanmax(ZI)')
contourf(XI,YI,ZI), hold
%Now we plot the outer dimension of the waterjet
theta = linspace(0,2*pi,100);
%plot of the shaft
shaft_x = shaft_radius*cos(theta);shaft_y = shaft_radius*sin(theta);
%make sure the shaft cover the proper area
    fill(shaft_x,shaft_y,'k')
COLORBAR('vert'), hold off
XLABEL('Horizontal Distance [mm]')
YLABEL('Verticl Distance [mm]')
LEGEND
PLOTEDIT ON
set(gca,'DataAspectRatio',[1 1 1],'PlotBoxAspectRatio',[1 1 1]);
grid

% ----------------------------------------------------------------------
function f = moody(ed,Re)
% Find friction factor by solving the Colebrook equation (Moody Chart)
%
% Synopsis:  f = moody(ed,Re)
%
% Input:     ed = relative roughness = epsilon/diameter
%            Re = Reynolds number
%
% Output:    f = friction factor
%
%

if Re<0
  error(sprintf('Reynolds number = %f cannot be negative',Re));
elseif Re<2000
  f = 64/Re;  return      %  laminar flow
end
if ed>0.05
  warning(sprintf('epsilon/diameter ratio = %f is not on Moody
chart',ed));
end
```

```
if Re<3500, warning(sprintf('Re = %f in transition range\n\n',Re));
end

%     Find f from Colebrook equation (use fzero).
%     coleFun is an inline function object to evaluate F(f,e/d,Re)
%     fzero returns the value of f such that F(f,e/d/Re) = 0
(approximately)
%     fi = initial guess
%     Iterations of fzero are terminated when f is known within +/-
dfTol
coleFun = inline('1.0/sqrt(f) + 2.0*log10( ed/3.7 + 2.51/( Re*sqrt(f))
)','f','ed','Re');
fi = 1/(1.8*log10(6.9/Re + (ed/3.7)^1.11))^2;   %  initial guess at f
dfTol = 5e-6;
f = fzero(coleFun,fi,optimset('TolX',dfTol,'Display','off'),ed,Re);
if f<0, error(sprintf('Friction factor = %f, but cannot be
negative',f)); end
```

Appendix C

Experimental Data

This Appendix contains the experimental data from waterjet system tests performed in the Memorial University wind tunnel.

Station 1a Flux Calculations
Experimental Data

Density of air	1.19E+00	kg/m^3
Ship speed	5.00E+00	m/s
h_{L0-1}	2.32E-01	m
b	4.68E-01	m
height	1.15E-01	m

Gravity	9.81E+00	m/s^2
Head loss	2.32E-01	m
V_E	4.52E+00	m/s
Q	2.50E-01	m^3/s
E_1	3.03E+00	W
M_1	1.34E+00	N

x [mm]	u [m/s]	x [m]	p-p_0 [Pa]	C_p	V_E	A1	A1 sum
2.00E-02	5.18E-01	2.00E-05	1.20E+01	8.07E-01	4.52E+00	5.18E-06	5.18E-06
7.00E-02	4.98E-01	7.00E-05	1.20E+01	8.08E-01	4.52E+00	2.54E-05	3.06E-05
1.20E-01	5.73E-01	1.20E-04	1.19E+01	8.05E-01	4.52E+00	2.68E-05	5.73E-05
1.70E-01	6.98E-01	1.70E-04	1.18E+01	7.98E-01	4.52E+00	3.18E-05	8.91E-05
2.70E-01	9.93E-01	2.70E-04	1.15E+01	7.78E-01	4.52E+00	8.46E-05	1.74E-04
3.70E-01	1.25E+00	3.70E-04	1.12E+01	7.55E-01	4.52E+00	1.12E-04	2.86E-04
4.70E-01	1.47E+00	4.70E-04	1.08E+01	7.31E-01	4.52E+00	1.36E-04	4.22E-04
5.70E-01	1.75E+00	5.70E-04	1.03E+01	6.95E-01	4.52E+00	1.61E-04	5.84E-04
6.70E-01	1.97E+00	6.70E-04	9.82E+00	6.63E-01	4.52E+00	1.86E-04	7.70E-04
7.70E-01	2.15E+00	7.70E-04	9.38E+00	6.33E-01	4.52E+00	2.06E-04	9.75E-04
8.70E-01	2.27E+00	8.70E-04	9.05E+00	6.11E-01	4.52E+00	2.21E-04	1.20E-03
9.70E-01	2.41E+00	9.70E-04	8.67E+00	5.85E-01	4.52E+00	2.34E-04	1.43E-03
1.22E+00	2.59E+00	1.22E-03	8.14E+00	5.49E-01	4.52E+00	6.25E-04	2.06E-03
1.47E+00	2.78E+00	1.47E-03	7.54E+00	5.09E-01	4.52E+00	6.71E-04	2.73E-03
1.72E+00	2.88E+00	1.72E-03	7.19E+00	4.85E-01	4.52E+00	7.08E-04	3.43E-03
1.97E+00	2.97E+00	1.97E-03	6.88E+00	4.65E-01	4.52E+00	7.32E-04	4.17E-03
2.47E+00	3.11E+00	2.47E-03	6.37E+00	4.30E-01	4.52E+00	1.52E-03	5.69E-03
2.97E+00	3.21E+00	2.97E-03	6.00E+00	4.05E-01	4.52E+00	1.58E-03	7.27E-03
3.47E+00	3.28E+00	3.47E-03	5.73E+00	3.87E-01	4.52E+00	1.62E-03	8.89E-03
3.97E+00	3.36E+00	3.97E-03	5.42E+00	3.66E-01	4.52E+00	1.66E-03	1.06E-02
4.97E+00	3.45E+00	4.97E-03	5.05E+00	3.41E-01	4.52E+00	3.41E-03	1.40E-02
5.97E+00	3.52E+00	5.97E-03	4.75E+00	3.21E-01	4.52E+00	3.49E-03	1.74E-02
7.97E+00	3.68E+00	7.97E-03	4.10E+00	2.77E-01	4.52E+00	7.20E-03	2.46E-02
9.97E+00	3.78E+00	9.97E-03	3.65E+00	2.47E-01	4.52E+00	7.46E-03	3.21E-02
1.20E+01	3.88E+00	1.20E-02	3.19E+00	2.15E-01	4.52E+00	7.66E-03	3.98E-02
1.50E+01	4.01E+00	1.50E-02	2.60E+00	1.75E-01	4.52E+00	1.18E-02	5.16E-02
2.00E+01	4.16E+00	2.00E-02	1.84E+00	1.24E-01	4.52E+00	2.04E-02	7.20E-02
2.50E+01	4.34E+00	2.50E-02	9.70E-01	6.55E-02	4.52E+00	2.12E-02	9.33E-02
3.00E+01	4.47E+00	3.00E-02	2.65E-01	1.79E-02	4.52E+00	2.20E-02	1.15E-01
4.00E+01	4.68E+00	4.00E-02	-8.90E-01	-6.01E-02	4.52E+00	4.58E-02	1.61E-01
5.00E+01	4.84E+00	5.00E-02	-1.79E+00	-1.21E-01	4.52E+00	4.76E-02	2.09E-01
6.00E+01	4.96E+00	6.00E-02	-2.45E+00	-1.65E-01	4.52E+00	4.90E-02	2.58E-01
8.00E+01	5.01E+00	8.00E-02	-2.73E+00	-1.84E-01	4.52E+00	9.96E-02	3.57E-01
1.00E+02	5.01E+00	1.00E-01	-2.73E+00	-1.84E-01	4.52E+00	1.00E-01	4.57E-01
1.25E+02	5.01E+00	1.25E-01	-2.73E+00	-1.84E-01	4.52E+00	1.25E-01	5.83E-01
1.50E+02	5.01E+00	1.50E-01	-2.73E+00	-1.84E-01	4.52E+00	1.25E-01	7.08E-01

Station 2 Flux Calculations
Experimental Data

Density of air	1.19E+00	kg/m^3
Ship speed	5.00E+00	m/s
$h_{L0\text{-}1}$	2.32E-01	m
$h_{L1\text{-}2}$	3.70E-01	m

Gravity	9.81E+00	m/s^2
Head loss	6.03E-01	m
V_E	3.63E+00	m/s
Q	2.97E-01	m^3/s
E_2	2.32E+00	W

x [m]	y [m]	u [m/s]	p-p_0 [Pa]	C_p	V_E
-1.75E-01	1.07E-17	0.00E+00	7.81E+00	5.27E-01	3.63E+00
-1.62E-01	-6.70E-02	7.18E-01	7.50E+00	5.06E-01	3.63E+00
-1.39E-01	-5.74E-02	1.02E+00	7.19E+00	4.85E-01	3.63E+00
-1.24E-01	-1.24E-01	8.33E-01	7.40E+00	4.99E-01	3.63E+00
-1.24E-01	1.24E-01	3.51E+00	5.20E-01	3.51E-02	3.63E+00
-1.15E-01	-4.78E-02	1.64E+00	6.21E+00	4.19E-01	3.63E+00
-1.06E-01	-1.06E-01	1.06E+00	7.14E+00	4.82E-01	3.63E+00
-1.06E-01	1.06E-01	3.63E+00	-2.10E-02	-1.42E-03	3.63E+00
-9.24E-02	-3.83E-02	2.78E+00	3.21E+00	2.17E-01	3.63E+00
-9.16E-02	1.00E-01	3.69E+00	-2.47E-01	-1.67E-02	3.63E+00
-8.84E-02	-8.84E-02	1.84E+00	5.79E+00	3.91E-01	3.63E+00
-8.84E-02	8.84E-02	3.64E+00	-2.64E-02	-1.78E-03	3.63E+00
-7.07E-02	-7.07E-02	2.59E+00	3.85E+00	2.60E-01	3.63E+00
-7.07E-02	7.07E-02	3.62E+00	3.69E-02	2.49E-03	3.63E+00
-7.07E-02	4.68E-02	2.75E+00	3.34E+00	2.26E-01	3.63E+00
-6.93E-02	-2.87E-02	3.15E+00	1.92E+00	1.29E-01	3.63E+00
-6.70E-02	-1.62E-01	7.02E-01	7.51E+00	5.07E-01	3.63E+00
-6.70E-02	1.62E-01	3.58E+00	2.20E-01	1.49E-02	3.63E+00
-5.74E-02	-1.39E-01	9.26E-01	7.30E+00	4.93E-01	3.63E+00
-5.74E-02	1.39E-01	3.61E+00	7.00E-02	4.73E-03	3.63E+00
-5.30E-02	-5.30E-02	2.97E+00	2.57E+00	1.74E-01	3.63E+00
-5.30E-02	5.30E-02	3.62E+00	3.70E-02	2.50E-03	3.63E+00
-5.00E-02	3.06E-18	3.61E+00	7.38E-02	4.98E-03	3.63E+00
-4.78E-02	-1.15E-01	2.15E+00	5.06E+00	3.42E-01	3.63E+00
-4.78E-02	1.15E-01	3.62E+00	3.18E-02	2.15E-03	3.63E+00
-4.62E-02	1.91E-02	3.59E+00	1.64E-01	1.11E-02	3.63E+00
-4.62E-02	-1.91E-02	3.34E+00	1.20E+00	8.13E-02	3.63E+00
-3.83E-02	-9.24E-02	2.51E+00	4.06E+00	2.74E-01	3.63E+00
-3.83E-02	9.24E-02	3.88E+00	-1.09E+00	-7.38E-02	3.63E+00
-3.54E-02	-3.54E-02	3.28E+00	1.44E+00	9.74E-02	3.63E+00
-3.54E-02	3.54E-02	3.70E+00	-3.01E-01	-2.03E-02	3.63E+00
-2.87E-02	-6.93E-02	2.76E+00	3.28E+00	2.21E-01	3.63E+00

x [m]	y [m]	u [m/s]	$p-p_0$ [Pa]	C_p	V_E
-2.87E-02	6.93E-02	3.89E+00	-1.14E+00	-7.68E-02	3.63E+00
-2.50E-02	1.53E-18	3.65E+00	-9.28E-02	-6.27E-03	3.63E+00
-2.31E-02	9.57E-03	3.74E+00	-4.61E-01	-3.11E-02	3.63E+00
-2.31E-02	-9.57E-03	3.58E+00	2.24E-01	1.52E-02	3.63E+00
-1.91E-02	-4.62E-02	3.11E+00	2.08E+00	1.40E-01	3.63E+00
-1.91E-02	4.62E-02	3.83E+00	-8.97E-01	-6.05E-02	3.63E+00
-1.77E-02	-1.77E-02	3.28E+00	1.43E+00	9.64E-02	3.63E+00
-1.77E-02	1.77E-02	3.62E+00	2.83E-02	1.91E-03	3.63E+00
-9.57E-03	-2.31E-02	3.41E+00	9.21E-01	6.22E-02	3.63E+00
-9.57E-03	2.31E-02	3.81E+00	-7.97E-01	-5.38E-02	3.63E+00
0.00E+00	-1.75E-01	5.00E-01	7.66E+00	5.17E-01	3.63E+00
0.00E+00	-1.50E-01	8.16E-01	7.41E+00	5.00E-01	3.63E+00
0.00E+00	-1.25E-01	9.10E-01	7.32E+00	4.94E-01	3.63E+00
0.00E+00	-1.00E-01	1.19E+00	6.96E+00	4.70E-01	3.63E+00
0.00E+00	-7.50E-02	1.72E+00	6.06E+00	4.09E-01	3.63E+00
0.00E+00	-5.00E-02	2.44E+00	4.28E+00	2.89E-01	3.63E+00
0.00E+00	-2.50E-02	3.16E+00	1.89E+00	1.27E-01	3.63E+00
0.00E+00	0.00E+00	3.64E+00	-4.74E-02	-3.20E-03	3.63E+00
0.00E+00	2.50E-02	3.90E+00	-1.21E+00	-8.15E-02	3.63E+00
0.00E+00	5.00E-02	3.99E+00	-1.64E+00	-1.11E-01	3.63E+00
0.00E+00	7.50E-02	4.05E+00	-1.91E+00	-1.29E-01	3.63E+00
0.00E+00	1.00E-01	3.95E+00	-1.43E+00	-9.63E-02	3.63E+00
0.00E+00	1.25E-01	3.69E+00	-2.71E-01	-1.83E-02	3.63E+00
0.00E+00	1.50E-01	3.42E+00	8.75E-01	5.91E-02	3.63E+00
0.00E+00	1.75E-01	3.15E+00	1.91E+00	1.29E-01	3.63E+00
0.00E+00	0.00E+00	3.68E+00	-2.14E-01	-1.44E-02	3.63E+00
9.57E-03	-2.31E-02	3.06E+00	2.27E+00	1.53E-01	3.63E+00
9.57E-03	2.31E-02	3.90E+00	-1.20E+00	-8.11E-02	3.63E+00
1.77E-02	-1.77E-02	3.13E+00	2.02E+00	1.36E-01	3.63E+00
1.77E-02	1.77E-02	3.85E+00	-9.82E-01	-6.63E-02	3.63E+00
1.91E-02	-4.62E-02	2.10E+00	5.20E+00	3.51E-01	3.63E+00
1.91E-02	4.62E-02	4.10E+00	-2.13E+00	-1.44E-01	3.63E+00
2.31E-02	-9.57E-03	3.62E+00	5.12E-02	3.46E-03	3.63E+00
2.31E-02	9.57E-03	3.76E+00	-5.68E-01	-3.83E-02	3.63E+00
2.50E-02	-4.59E-18	3.75E+00	-5.12E-01	-3.45E-02	3.63E+00
2.87E-02	-6.93E-02	1.56E+00	6.36E+00	4.29E-01	3.63E+00
2.87E-02	6.93E-02	4.14E+00	-2.33E+00	-1.57E-01	3.63E+00
3.54E-02	-3.54E-02	2.28E+00	4.73E+00	3.19E-01	3.63E+00
3.54E-02	3.54E-02	4.07E+00	-1.99E+00	-1.34E-01	3.63E+00
3.83E-02	-9.24E-02	1.48E+00	6.52E+00	4.40E-01	3.63E+00
3.83E-02	9.24E-02	3.96E+00	-1.50E+00	-1.01E-01	3.63E+00
4.62E-02	-1.91E-02	3.50E+00	5.32E-01	3.59E-02	3.63E+00

x [m]	y [m]	u [m/s]	$p-p_0$ [Pa]	C_p	V_E
4.62E-02	1.91E-02	3.87E+00	-1.08E+00	-7.30E-02	3.63E+00
4.78E-02	-1.15E-01	1.35E+00	6.73E+00	4.54E-01	3.63E+00
4.78E-02	1.15E-01	3.49E+00	5.90E-01	3.99E-02	3.63E+00
5.00E-02	-9.19E-18	3.78E+00	-6.45E-01	-4.36E-02	3.63E+00
5.30E-02	-5.30E-02	1.96E+00	5.53E+00	3.74E-01	3.63E+00
5.30E-02	5.30E-02	4.11E+00	-2.18E+00	-1.47E-01	3.63E+00
5.74E-02	-1.39E-01	1.26E+00	6.86E+00	4.63E-01	3.63E+00
5.74E-02	1.39E-01	3.04E+00	2.35E+00	1.58E-01	3.63E+00
6.70E-02	-1.62E-01	5.73E-01	7.61E+00	5.14E-01	3.63E+00
6.70E-02	1.62E-01	2.75E+00	3.34E+00	2.25E-01	3.63E+00
6.93E-02	-2.87E-02	3.40E+00	9.72E-01	6.56E-02	3.63E+00
6.93E-02	2.87E-02	3.99E+00	-1.61E+00	-1.09E-01	3.63E+00
7.07E-02	-7.07E-02	1.92E+00	5.62E+00	3.80E-01	3.63E+00
7.07E-02	7.07E-02	4.18E+00	-2.54E+00	-1.71E-01	3.63E+00
7.50E-02	-1.38E-17	3.88E+00	-1.10E+00	-7.43E-02	3.63E+00
8.84E-02	-8.84E-02	2.24E+00	4.85E+00	3.27E-01	3.63E+00
8.84E-02	8.84E-02	3.95E+00	-1.42E+00	-9.60E-02	3.63E+00
9.24E-02	-3.83E-02	3.28E+00	1.42E+00	9.58E-02	3.63E+00
9.24E-02	3.83E-02	4.06E+00	-1.95E+00	-1.32E-01	3.63E+00
1.00E-01	-1.84E-17	3.94E+00	-1.38E+00	-9.30E-02	3.63E+00
1.06E-01	-1.06E-01	2.19E+00	4.97E+00	3.35E-01	3.63E+00
1.06E-01	1.06E-01	3.59E+00	1.52E-01	1.03E-02	3.63E+00
1.15E-01	-4.78E-02	3.42E+00	8.70E-01	5.87E-02	3.63E+00
1.15E-01	4.78E-02	4.10E+00	-2.17E+00	-1.47E-01	3.63E+00
1.24E-01	-1.24E-01	1.39E+00	6.67E+00	4.50E-01	3.63E+00
1.24E-01	1.24E-01	2.94E+00	2.69E+00	1.82E-01	3.63E+00
1.25E-01	-2.30E-17	4.02E+00	-1.76E+00	-1.19E-01	3.63E+00
1.39E-01	-5.74E-02	3.42E+00	8.69E-01	5.87E-02	3.63E+00
1.39E-01	5.74E-02	4.18E+00	-2.55E+00	-1.72E-01	3.63E+00
1.50E-01	-2.76E-17	4.07E+00	-2.02E+00	-1.37E-01	3.63E+00
1.62E-01	-6.70E-02	3.06E+00	2.26E+00	1.52E-01	3.63E+00
1.62E-01	6.70E-02	3.89E+00	-1.17E+00	-7.93E-02	3.63E+00
1.75E-01	-3.22E-17	4.04E+00	-1.85E+00	-1.25E-01	3.63E+00

Station 3 Flux Calculations
Experimental Data

Density of air	1.19E+00	kg/m^3
Ship speed	5.00E+00	m/s
$h_{L0\text{-}1}$	2.32E-01	m
$h_{L1\text{-}2}$	3.70E-01	m
$h_{L2\text{-}3}$	4.92E-02	m

Gravity	9.81E+00	m/s^2
Head loss	6.52E-01	m
V_E	3.49E+00	m/s
Q_3	2.21E-01	m^3/s
E3	1.60E+00	W

x [m]	y [m]	u [m/s]	p-p_0 [Pa]	C_p	V_E
-1.72E-01	1.05E-17	1.80E+00	5.31E+00	3.58E-01	3.49E+00
-1.60E-01	9.80E-18	1.58E+00	5.75E+00	3.88E-01	3.49E+00
-1.35E-01	8.27E-18	1.92E+00	5.05E+00	3.41E-01	3.49E+00
-1.22E-01	-1.22E-01	1.55E+00	5.82E+00	3.93E-01	3.49E+00
-1.22E-01	1.22E-01	6.00E-01	7.02E+00	4.74E-01	3.49E+00
-1.13E-01	1.13E-01	2.10E+00	4.61E+00	3.11E-01	3.49E+00
-1.12E-01	-1.12E-01	1.63E+00	5.66E+00	3.82E-01	3.49E+00
-1.10E-01	6.74E-18	1.96E+00	4.95E+00	3.34E-01	3.49E+00
-9.55E-02	9.55E-02	2.57E+00	3.32E+00	2.24E-01	3.49E+00
-9.40E-02	-9.40E-02	2.39E+00	3.85E+00	2.60E-01	3.49E+00
-8.50E-02	5.21E-18	2.07E+00	4.70E+00	3.17E-01	3.49E+00
-7.78E-02	7.78E-02	2.93E+00	2.15E+00	1.45E-01	3.49E+00
-7.64E-02	-7.64E-02	2.72E+00	2.86E+00	1.93E-01	3.49E+00
-6.01E-02	6.01E-02	2.82E+00	2.52E+00	1.70E-01	3.49E+00
-6.00E-02	3.68E-18	1.81E+00	5.29E+00	3.57E-01	3.49E+00
-5.87E-02	-5.87E-02	2.44E+00	3.72E+00	2.51E-01	3.49E+00
-4.24E-02	4.24E-02	1.55E+00	5.81E+00	3.92E-01	3.49E+00
-4.10E-02	-4.10E-02	8.20E-01	6.84E+00	4.62E-01	3.49E+00
-2.14E-17	-1.75E-01	0.00E+00	7.23E+00	4.88E-01	3.49E+00
-2.11E-17	-1.72E-01	2.02E+00	4.81E+00	3.25E-01	3.49E+00
-1.96E-17	-1.60E-01	1.96E+00	4.95E+00	3.34E-01	3.49E+00
-1.65E-17	-1.35E-01	2.50E+00	3.53E+00	2.38E-01	3.49E+00
-1.35E-17	-1.10E-01	2.77E+00	2.70E+00	1.83E-01	3.49E+00
-1.04E-17	-8.50E-02	3.26E+00	9.41E-01	6.35E-02	3.49E+00
-7.35E-18	-6.00E-02	3.82E+00	-1.40E+00	-9.45E-02	3.49E+00
0.00E+00	6.00E-02	3.82E+00	-1.40E+00	-9.45E-02	3.49E+00
0.00E+00	8.50E-02	3.26E+00	9.41E-01	6.35E-02	3.49E+00
0.00E+00	1.10E-01	2.77E+00	2.70E+00	1.83E-01	3.49E+00
0.00E+00	1.35E-01	2.50E+00	3.53E+00	2.38E-01	3.49E+00
0.00E+00	1.60E-01	1.96E+00	4.95E+00	3.34E-01	3.49E+00
0.00E+00	1.72E-01	2.02E+00	4.81E+00	3.25E-01	3.49E+00
4.10E-02	-4.10E-02	8.20E-01	6.84E+00	4.62E-01	3.49E+00

x [m]	y [m]	u [m/s]	$p-p_0$ [Pa]	C_p	V_E
4.60E-02	4.60E-02	1.55E+00	5.81E+00	3.92E-01	3.49E+00
5.87E-02	-5.87E-02	2.44E+00	3.72E+00	2.51E-01	3.49E+00
6.00E-02	-1.10E-17	1.81E+00	5.29E+00	3.57E-01	3.49E+00
6.36E-02	6.36E-02	2.82E+00	2.52E+00	1.70E-01	3.49E+00
7.64E-02	-7.64E-02	2.72E+00	2.86E+00	1.93E-01	3.49E+00
8.13E-02	8.13E-02	2.93E+00	2.15E+00	1.45E-01	3.49E+00
8.50E-02	-1.56E-17	2.07E+00	4.70E+00	3.17E-01	3.49E+00
9.40E-02	-9.40E-02	2.39E+00	3.85E+00	2.60E-01	3.49E+00
9.90E-02	9.90E-02	2.57E+00	3.32E+00	2.24E-01	3.49E+00
1.10E-01	-2.02E-17	1.96E+00	4.95E+00	3.34E-01	3.49E+00
1.12E-01	-1.12E-01	1.63E+00	5.66E+00	3.82E-01	3.49E+00
1.17E-01	1.17E-01	2.10E+00	4.61E+00	3.11E-01	3.49E+00
1.22E-01	-1.22E-01	1.55E+00	5.82E+00	3.93E-01	3.49E+00
1.22E-01	1.22E-01	6.00E-01	7.02E+00	4.74E-01	3.49E+00
1.35E-01	-2.48E-17	1.92E+00	5.05E+00	3.41E-01	3.49E+00
1.60E-01	-2.94E-17	1.58E+00	5.75E+00	3.88E-01	3.49E+00
1.72E-01	-3.16E-17	1.80E+00	5.31E+00	3.58E-01	3.49E+00

Station 5 Flux Calculations
Experimental Data

Density of air	1.19E+00	kg/m^3
Ship speed	5.00E+00	m/s
h_{L0-1}	2.32E-01	m
h_{L1-2}	3.70E-01	m
h_{L2-3}	4.92E-02	m
h_{3-5}	1.98E+00	

Gravity	9.81E+00	m/s^2
Head loss	-1.32E+00	m
V_E	7.14E+00	m/s
Q_5	2.63E-01	m^3/s
E_5	7.94E+00	W

x [m]	y [m]	u [m/s]	$p-p_0$ [Pa]	C_p	V_E
-1.72E-01	1.05E-17	2.92E+00	2.52E+01	1.70E+00	7.14E+00
-1.55E-01	9.49E-18	4.72E+00	1.70E+01	1.15E+00	7.14E+00
-1.30E-01	7.96E-18	2.79E+00	2.56E+01	1.73E+00	7.14E+00
-1.22E-01	-1.22E-01	2.50E+00	2.65E+01	1.79E+00	7.14E+00
-1.22E-01	1.22E-01	2.60E+00	2.62E+01	1.77E+00	7.14E+00
-1.10E-01	-1.10E-01	3.03E+00	2.48E+01	1.67E+00	7.14E+00
-1.10E-01	1.10E-01	4.62E+00	1.75E+01	1.18E+00	7.14E+00
-1.05E-01	6.43E-18	2.24E+00	2.72E+01	1.84E+00	7.14E+00
-9.19E-02	-9.19E-02	3.44E+00	2.32E+01	1.56E+00	7.14E+00
-9.19E-02	9.19E-02	4.35E+00	1.90E+01	1.28E+00	7.14E+00
-8.00E-02	4.90E-18	3.07E+00	2.46E+01	1.66E+00	7.14E+00
-7.42E-02	-7.42E-02	2.83E+00	2.54E+01	1.72E+00	7.14E+00
-7.42E-02	7.42E-02	3.11E+00	2.45E+01	1.65E+00	7.14E+00
-5.66E-02	-5.66E-02	2.93E+00	2.51E+01	1.70E+00	7.14E+00
-5.66E-02	5.66E-02	3.40E+00	2.34E+01	1.58E+00	7.14E+00
-5.50E-02	3.37E-18	7.53E-01	2.99E+01	2.02E+00	7.14E+00
-3.89E-02	-3.89E-02	1.50E+00	2.89E+01	1.95E+00	7.14E+00
-3.89E-02	3.89E-02	7.29E-01	2.99E+01	2.02E+00	7.14E+00
-2.11E-17	-1.72E-01	2.63E+00	2.61E+01	1.76E+00	7.14E+00
-1.90E-17	-1.55E-01	2.28E+00	2.71E+01	1.83E+00	7.14E+00
-1.59E-17	-1.30E-01	1.79E+00	2.83E+01	1.91E+00	7.14E+00
-1.29E-17	-1.05E-01	3.24E+00	2.40E+01	1.62E+00	7.14E+00
-9.80E-18	-8.00E-02	2.37E+00	2.69E+01	1.81E+00	7.14E+00
-6.74E-18	-5.50E-02	2.65E+00	2.60E+01	1.76E+00	7.14E+00
0.00E+00	5.50E-02	8.64E-02	3.02E+01	2.04E+00	7.14E+00
0.00E+00	8.00E-02	1.91E+00	2.80E+01	1.89E+00	7.14E+00
0.00E+00	1.05E-01	2.90E+00	2.52E+01	1.70E+00	7.14E+00
0.00E+00	1.30E-01	3.52E+00	2.29E+01	1.54E+00	7.14E+00
0.00E+00	1.55E-01	2.57E+00	2.63E+01	1.78E+00	7.14E+00
0.00E+00	1.72E-01	3.01E+00	2.48E+01	1.68E+00	7.14E+00
3.89E-02	-3.89E-02	1.50E+00	2.89E+01	1.95E+00	7.14E+00

x [m]	y [m]	u [m/s]	$p-p_0$ [Pa]	C_p	V_E
3.89E-02	3.89E-02	7.29E-01	2.99E+01	2.02E+00	7.14E+00
5.50E-02	-1.01E-17	7.53E-01	2.99E+01	2.02E+00	7.14E+00
5.66E-02	-5.66E-02	2.93E+00	2.51E+01	1.70E+00	7.14E+00
5.66E-02	5.66E-02	3.40E+00	2.34E+01	1.58E+00	7.14E+00
7.42E-02	-7.42E-02	2.83E+00	2.54E+01	1.72E+00	7.14E+00
7.42E-02	7.42E-02	3.11E+00	2.45E+01	1.65E+00	7.14E+00
8.00E-02	-1.47E-17	3.07E+00	2.46E+01	1.66E+00	7.14E+00
9.19E-02	-9.19E-02	3.44E+00	2.32E+01	1.56E+00	7.14E+00
9.19E-02	9.19E-02	4.35E+00	1.90E+01	1.28E+00	7.14E+00
1.05E-01	-1.93E-17	2.24E+00	2.72E+01	1.84E+00	7.14E+00
1.10E-01	-1.10E-01	3.03E+00	2.48E+01	1.67E+00	7.14E+00
1.10E-01	1.10E-01	4.62E+00	1.75E+01	1.18E+00	7.14E+00
1.22E-01	-1.22E-01	2.50E+00	2.65E+01	1.79E+00	7.14E+00
1.22E-01	1.22E-01	2.60E+00	2.62E+01	1.77E+00	7.14E+00
1.30E-01	-2.39E-17	2.79E+00	2.56E+01	1.73E+00	7.14E+00
1.55E-01	-2.85E-17	4.72E+00	1.70E+01	1.15E+00	7.14E+00
1.72E-01	-3.16E-17	2.92E+00	2.52E+01	1.70E+00	7.14E+00

Station 6 Flux Calculations
Experimental Data

Density of air	1.19E+00	kg/m^3
Ship speed	5.00E+00	m/s
$h_{L0\text{-}1}$	2.32E-01	m
$h_{L1\text{-}2}$	3.70E-01	m
$h_{L2\text{-}3}$	4.92E-02	m
$h_{3\text{-}5}$	1.98E+00	m
$h_{5\text{-}6}$	9.58E-02	m

Gravity	9.81E+00	m/s^2
Head loss	-1.23E+00	m
V_E	7.01E+00	m/s
Q_6	2.18E-01	m^3/s
E6	6.34E+00	W

x [m]	y [m]	u [m/s]	$p\text{-}p_0$ [Pa]	C_p	V_E
-1.75E-01	1.07E-17	0.00E+00	2.91E+01	1.96E+00	7.01E+00
-1.62E-01	6.70E-02	0.00E+00	2.91E+01	1.96E+00	7.01E+00
-1.62E-01	-6.70E-02	0.00E+00	2.91E+01	1.96E+00	7.01E+00
-1.50E-01	9.19E-18	0.00E+00	2.91E+01	1.96E+00	7.01E+00
-1.39E-01	5.74E-02	0.00E+00	2.91E+01	1.96E+00	7.01E+00
-1.39E-01	-5.74E-02	0.00E+00	2.91E+01	1.96E+00	7.01E+00
-1.25E-01	7.66E-18	6.80E+00	1.66E+00	1.12E-01	7.01E+00
-1.25E-01	7.66E-18	0.00E+00	2.91E+01	1.96E+00	7.01E+00
-1.24E-01	-1.24E-01	0.00E+00	2.91E+01	1.96E+00	7.01E+00
-1.24E-01	1.24E-01	0.00E+00	2.91E+01	1.96E+00	7.01E+00
-1.15E-01	7.07E-18	6.71E+00	2.45E+00	1.65E-01	7.01E+00
-1.15E-01	4.78E-02	6.70E+00	2.50E+00	1.69E-01	7.01E+00
-1.15E-01	-4.78E-02	1.01E-01	2.91E+01	1.96E+00	7.01E+00
-1.06E-01	-1.06E-01	0.00E+00	2.91E+01	1.96E+00	7.01E+00
-1.06E-01	1.06E-01	0.00E+00	2.91E+01	1.96E+00	7.01E+00
-9.24E-02	5.66E-18	6.30E+00	5.56E+00	3.76E-01	7.01E+00
-9.24E-02	3.83E-02	5.13E+00	1.35E+01	9.12E-01	7.01E+00
-9.24E-02	-3.83E-02	5.86E+00	8.77E+00	5.92E-01	7.01E+00
-8.84E-02	-8.84E-02	3.88E-02	2.91E+01	1.96E+00	7.01E+00
-8.84E-02	8.84E-02	6.05E+00	7.41E+00	5.00E-01	7.01E+00
-7.07E-02	-7.07E-02	7.06E+00	-4.58E-01	-3.09E-02	7.01E+00
-7.07E-02	7.07E-02	6.74E+00	2.18E+00	1.47E-01	7.01E+00
-6.93E-02	2.87E-02	4.39E+00	1.77E+01	1.19E+00	7.01E+00
-6.93E-02	-2.87E-02	5.04E+00	1.41E+01	9.49E-01	7.01E+00
-6.93E-02	4.24E-18	5.50E+00	1.11E+01	7.52E-01	7.01E+00
-6.70E-02	-1.62E-01	0.00E+00	2.91E+01	1.96E+00	7.01E+00
-6.70E-02	1.62E-01	0.00E+00	2.91E+01	1.96E+00	7.01E+00
-5.74E-02	-1.39E-01	0.00E+00	2.91E+01	1.96E+00	7.01E+00
-5.74E-02	1.39E-01	0.00E+00	2.91E+01	1.96E+00	7.01E+00
-5.30E-02	-5.30E-02	6.59E+00	3.36E+00	2.27E-01	7.01E+00

x [m]	y [m]	u [m/s]	$p-p_0$ [Pa]	C_p	V_E
-5.30E-02	5.30E-02	6.08E+00	7.17E+00	4.84E-01	7.01E+00
-4.78E-02	-1.15E-01	4.75E-02	2.91E+01	1.96E+00	7.01E+00
-4.78E-02	1.15E-01	1.77E-01	2.91E+01	1.96E+00	7.01E+00
-4.62E-02	1.91E-02	4.83E+00	1.53E+01	1.03E+00	7.01E+00
-4.62E-02	-1.91E-02	5.27E+00	1.27E+01	8.55E-01	7.01E+00
-4.62E-02	2.83E-18	4.75E+00	1.57E+01	1.06E+00	7.01E+00
-3.83E-02	-9.24E-02	5.59E+00	1.06E+01	7.14E-01	7.01E+00
-3.83E-02	9.24E-02	4.65E+00	1.63E+01	1.10E+00	7.01E+00
-3.54E-02	-3.54E-02	5.68E+00	9.96E+00	6.72E-01	7.01E+00
-3.54E-02	3.54E-02	5.37E+00	1.20E+01	8.10E-01	7.01E+00
-2.87E-02	-6.93E-02	4.81E+00	1.54E+01	1.04E+00	7.01E+00
-2.87E-02	6.93E-02	4.41E+00	1.76E+01	1.19E+00	7.01E+00
-2.31E-02	9.57E-03	3.55E+00	2.16E+01	1.46E+00	7.01E+00
-2.31E-02	-9.57E-03	6.56E-02	2.91E+01	1.96E+00	7.01E+00
-1.91E-02	-4.62E-02	5.43E+00	1.16E+01	7.85E-01	7.01E+00
-1.91E-02	4.62E-02	4.36E+00	1.78E+01	1.20E+00	7.01E+00
-1.77E-02	-1.77E-02	0.00E+00	2.91E+01	1.96E+00	7.01E+00
-1.77E-02	1.77E-02	0.00E+00	2.91E+01	1.96E+00	7.01E+00
-9.57E-03	-2.31E-02	4.70E+00	1.60E+01	1.08E+00	7.01E+00
-9.57E-03	2.31E-02	2.94E+00	2.40E+01	1.62E+00	7.01E+00
-2.14E-17	-1.75E-01	0.00E+00	2.91E+01	1.96E+00	7.01E+00
-1.84E-17	-1.50E-01	0.00E+00	2.91E+01	1.96E+00	7.01E+00
-1.53E-17	-1.25E-01	5.66E-02	2.91E+01	1.96E+00	7.01E+00
-1.23E-17	-1.00E-01	7.23E+00	-1.90E+00	-1.28E-01	7.01E+00
-9.19E-18	-7.50E-02	7.26E+00	-2.13E+00	-1.44E-01	7.01E+00
-6.13E-18	-5.00E-02	6.96E+00	4.12E-01	2.78E-02	7.01E+00
-3.06E-18	-2.50E-02	3.68E+00	2.11E+01	1.42E+00	7.01E+00
0.00E+00	0.00E+00	0.00E+00	2.91E+01	1.96E+00	7.01E+00
0.00E+00	2.50E-02	3.31E+00	2.26E+01	1.52E+00	7.01E+00
0.00E+00	5.00E-02	5.74E+00	9.57E+00	6.46E-01	7.01E+00
0.00E+00	7.50E-02	6.29E+00	5.67E+00	3.83E-01	7.01E+00
0.00E+00	1.00E-01	6.63E+00	3.01E+00	2.03E-01	7.01E+00
0.00E+00	1.25E-01	6.77E+00	1.94E+00	1.31E-01	7.01E+00
0.00E+00	1.50E-01	0.00E+00	2.91E+01	1.96E+00	7.01E+00
0.00E+00	1.75E-01	0.00E+00	2.91E+01	1.96E+00	7.01E+00
9.57E-03	-2.31E-02	5.39E+00	1.19E+01	8.03E-01	7.01E+00
9.57E-03	2.31E-02	4.80E+00	1.54E+01	1.04E+00	7.01E+00
1.77E-02	-1.77E-02	5.22E+00	1.30E+01	8.76E-01	7.01E+00
1.77E-02	1.77E-02	3.50E+00	2.18E+01	1.47E+00	7.01E+00
1.91E-02	-4.62E-02	5.11E+00	1.36E+01	9.19E-01	7.01E+00
1.91E-02	4.62E-02	4.38E+00	1.77E+01	1.20E+00	7.01E+00
2.31E-02	-9.57E-03	0.00E+00	2.91E+01	1.96E+00	7.01E+00

x [m]	y [m]	u [m/s]	$p-p_0$ [Pa]	C_p	V_E
2.31E-02	9.57E-03	3.83E+00	2.04E+01	1.38E+00	7.01E+00
2.31E-02	-4.24E-18	4.97E+00	1.45E+01	9.77E-01	7.01E+00
2.87E-02	-6.93E-02	5.28E+00	1.26E+01	8.50E-01	7.01E+00
2.87E-02	6.93E-02	4.45E+00	1.74E+01	1.17E+00	7.01E+00
3.54E-02	-3.54E-02	6.34E+00	5.28E+00	3.56E-01	7.01E+00
3.54E-02	3.54E-02	5.79E+00	9.22E+00	6.23E-01	7.01E+00
3.83E-02	-9.24E-02	6.38E+00	4.97E+00	3.36E-01	7.01E+00
3.83E-02	9.24E-02	4.67E+00	1.62E+01	1.09E+00	7.01E+00
4.62E-02	-8.49E-18	6.08E+00	7.17E+00	4.84E-01	7.01E+00
4.62E-02	-1.91E-02	5.09E+00	1.37E+01	9.26E-01	7.01E+00
4.62E-02	1.91E-02	4.42E+00	1.75E+01	1.18E+00	7.01E+00
4.78E-02	-1.15E-01	7.00E-02	2.91E+01	1.96E+00	7.01E+00
4.78E-02	1.15E-01	1.61E+00	2.76E+01	1.86E+00	7.01E+00
5.30E-02	-5.30E-02	6.75E+00	2.11E+00	1.43E-01	7.01E+00
5.30E-02	5.30E-02	6.26E+00	5.90E+00	3.98E-01	7.01E+00
5.74E-02	-1.39E-01	0.00E+00	2.91E+01	1.96E+00	7.01E+00
5.74E-02	1.39E-01	0.00E+00	2.91E+01	1.96E+00	7.01E+00
6.70E-02	-1.62E-01	0.00E+00	2.91E+01	1.96E+00	7.01E+00
6.70E-02	1.62E-01	0.00E+00	2.91E+01	1.96E+00	7.01E+00
6.93E-02	-1.27E-17	6.49E+00	4.16E+00	2.81E-01	7.01E+00
6.93E-02	-2.87E-02	4.79E+00	1.55E+01	1.05E+00	7.01E+00
6.93E-02	2.87E-02	4.61E+00	1.65E+01	1.11E+00	7.01E+00
7.07E-02	-7.07E-02	7.59E+00	-5.02E+00	-3.39E-01	7.01E+00
7.07E-02	7.07E-02	6.59E+00	3.38E+00	2.28E-01	7.01E+00
8.84E-02	-8.84E-02	5.39E-02	2.91E+01	1.96E+00	7.01E+00
8.84E-02	8.84E-02	6.98E-02	2.91E+01	1.96E+00	7.01E+00
9.24E-02	-3.83E-02	6.51E+00	3.98E+00	2.69E-01	7.01E+00
9.24E-02	3.83E-02	5.52E+00	1.10E+01	7.46E-01	7.01E+00
9.24E-02	-1.70E-17	7.08E+00	-6.33E-01	-4.27E-02	7.01E+00
1.06E-01	-1.06E-01	0.00E+00	2.91E+01	1.96E+00	7.01E+00
1.06E-01	1.06E-01	0.00E+00	2.91E+01	1.96E+00	7.01E+00
1.15E-01	-4.78E-02	1.62E-02	2.91E+01	1.96E+00	7.01E+00
1.15E-01	4.78E-02	4.96E-02	2.91E+01	1.96E+00	7.01E+00
1.15E-01	-2.12E-17	6.20E+00	6.29E+00	4.24E-01	7.01E+00
1.24E-01	-1.24E-01	0.00E+00	2.91E+01	1.96E+00	7.01E+00
1.24E-01	1.24E-01	0.00E+00	2.91E+01	1.96E+00	7.01E+00
1.25E-01	-2.30E-17	4.34E-02	2.91E+01	1.96E+00	7.01E+00
1.39E-01	-5.74E-02	0.00E+00	2.91E+01	1.96E+00	7.01E+00
1.39E-01	5.74E-02	0.00E+00	2.91E+01	1.96E+00	7.01E+00
1.62E-01	-6.70E-02	0.00E+00	2.91E+01	1.96E+00	7.01E+00
1.62E-01	6.70E-02	0.00E+00	2.91E+01	1.96E+00	7.01E+00
1.75E-01	-3.22E-17	0.00E+00	2.91E+01	1.96E+00	7.01E+00

Station 7 Flux Calculations
Experimental Data

Density of air	1.19E+00	kg/m^3
Ship speed	5.00E+00	m/s
h_{L0-1}	2.32E-01	m
h_{L1-2}	3.70E-01	m
h_{L2-3}	4.92E-02	m
$h_{3-5\ (rise)}$	1.98E+00	m
h_{5-6}	9.58E-02	m
h_{6-7}	1.10E+00	m

Gravity	9.81E+00	m/s^2
Head loss	-1.31E-01	m
V_E	5.58E+00	m/s
Q_7	2.50E-01	m^3/s
E_7	4.62E+00	W
M_7	1.65E+00	N

x [m]	y [m]	u [m/s]	p-p_0 [Pa]	C_p	V_E
-1.15E-01	-4.78E-02	2.34E+00	1.31E+01	8.84E-01	5.25E+00
-1.06E-01	6.50E-18	3.29E+00	9.91E+00	6.69E-01	5.25E+00
-1.06E-01	-1.06E-01	2.86E-01	1.63E+01	1.10E+00	5.25E+00
-1.06E-01	1.06E-01	2.96E-01	1.63E+01	1.10E+00	5.25E+00
-9.24E-02	3.83E-02	4.75E+00	2.97E+00	2.00E-01	5.25E+00
-9.24E-02	-3.83E-02	4.83E+00	2.54E+00	1.71E-01	5.25E+00
-8.84E-02	5.41E-18	5.37E+00	-7.62E-01	-5.14E-02	5.25E+00
-8.84E-02	-8.84E-02	1.61E+00	1.48E+01	9.99E-01	5.25E+00
-8.84E-02	8.84E-02	1.69E+00	1.46E+01	9.88E-01	5.25E+00
-7.07E-02	-7.07E-02	3.41E+00	9.45E+00	6.38E-01	5.25E+00
-7.07E-02	7.07E-02	4.12E+00	6.28E+00	4.24E-01	5.25E+00
-7.07E-02	4.33E-18	6.55E+00	-9.08E+00	-6.13E-01	5.25E+00
-6.93E-02	2.87E-02	6.38E+00	-7.79E+00	-5.26E-01	5.25E+00
-6.93E-02	-2.87E-02	6.70E+00	-1.03E+01	-6.95E-01	5.25E+00
-6.70E-02	-1.62E-01	4.78E-02	1.63E+01	1.10E+00	5.25E+00
-6.70E-02	1.62E-01	1.67E-01	1.63E+01	1.10E+00	5.25E+00
-5.74E-02	-1.39E-01	2.21E-01	1.63E+01	1.10E+00	5.25E+00
-5.74E-02	1.39E-01	1.59E+00	1.48E+01	1.00E+00	5.25E+00
-5.50E-02	3.37E-18	7.17E+00	-1.41E+01	-9.52E-01	5.25E+00
-5.30E-02	-5.30E-02	5.83E+00	-3.77E+00	-2.55E-01	5.25E+00
-5.30E-02	5.30E-02	6.28E+00	-7.05E+00	-4.76E-01	5.25E+00
-4.78E-02	-1.15E-01	1.75E+00	1.45E+01	9.80E-01	5.25E+00
-4.78E-02	1.15E-01	2.98E+00	1.11E+01	7.48E-01	5.25E+00
-4.62E-02	1.91E-02	6.61E+00	-9.52E+00	-6.43E-01	5.25E+00
-4.62E-02	-1.91E-02	6.94E+00	-1.22E+01	-8.24E-01	5.25E+00
-3.83E-02	-9.24E-02	4.14E+00	6.19E+00	4.18E-01	5.25E+00
-3.83E-02	9.24E-02	5.39E+00	-8.88E-01	-6.00E-02	5.25E+00
-3.54E-02	2.17E-18	7.22E+00	-1.45E+01	-9.80E-01	5.25E+00
-3.54E-02	-3.54E-02	7.01E+00	-1.28E+01	-8.61E-01	5.25E+00

x [m]	y [m]	u [m/s]	$p-p_0$ [Pa]	C_p	V_E
-3.54E-02	3.54E-02	7.04E+00	-1.31E+01	-8.82E-01	5.25E+00
-2.87E-02	-6.93E-02	6.73E+00	-1.05E+01	-7.10E-01	5.25E+00
-2.87E-02	6.93E-02	6.12E+00	-5.82E+00	-3.93E-01	5.25E+00
-2.31E-02	9.57E-03	7.08E+00	-1.34E+01	-9.03E-01	5.25E+00
-2.31E-02	-9.57E-03	7.07E+00	-1.33E+01	-8.99E-01	5.25E+00
-1.91E-02	-4.62E-02	6.86E+00	-1.15E+01	-7.78E-01	5.25E+00
-1.91E-02	4.62E-02	6.63E+00	-9.73E+00	-6.57E-01	5.25E+00
-1.77E-02	1.08E-18	7.13E+00	-1.38E+01	-9.33E-01	5.25E+00
-1.77E-02	-1.77E-02	7.09E+00	-1.35E+01	-9.08E-01	5.25E+00
-1.77E-02	1.77E-02	7.20E+00	-1.44E+01	-9.69E-01	5.25E+00
-9.57E-03	-2.31E-02	6.80E+00	-1.11E+01	-7.47E-01	5.25E+00
-9.57E-03	2.31E-02	6.81E+00	-1.12E+01	-7.54E-01	5.25E+00
-2.14E-17	-1.75E-01	1.16E-01	1.63E+01	1.10E+00	5.25E+00
-1.84E-17	-1.50E-01	6.42E-01	1.61E+01	1.09E+00	5.25E+00
-1.53E-17	-1.25E-01	1.98E+00	1.40E+01	9.45E-01	5.25E+00
-1.23E-17	-1.00E-01	4.21E+00	5.82E+00	3.93E-01	5.25E+00
-9.19E-18	-7.50E-02	5.78E+00	-3.44E+00	-2.32E-01	5.25E+00
-6.13E-18	-5.00E-02	6.72E+00	-1.04E+01	-7.02E-01	5.25E+00
-3.06E-18	-2.50E-02	6.99E+00	-1.26E+01	-8.50E-01	5.25E+00
0.00E+00	0.00E+00	6.38E+00	-7.80E+00	-5.27E-01	5.25E+00
0.00E+00	2.50E-02	6.77E+00	-1.08E+01	-7.31E-01	5.25E+00
0.00E+00	5.00E-02	6.69E+00	-1.02E+01	-6.90E-01	5.25E+00
0.00E+00	7.50E-02	6.18E+00	-6.30E+00	-4.25E-01	5.25E+00
0.00E+00	1.00E-01	3.92E+00	7.22E+00	4.87E-01	5.25E+00
0.00E+00	1.25E-01	1.87E+00	1.43E+01	9.62E-01	5.25E+00
0.00E+00	1.50E-01	3.92E-01	1.62E+01	1.10E+00	5.25E+00
0.00E+00	1.75E-01	8.78E-02	1.63E+01	1.10E+00	5.25E+00
9.57E-03	-2.31E-02	6.81E+00	-1.12E+01	-7.53E-01	5.25E+00
9.57E-03	2.31E-02	6.40E+00	-7.93E+00	-5.36E-01	5.25E+00
1.77E-02	-1.77E-02	6.65E+00	-9.88E+00	-6.67E-01	5.25E+00
1.77E-02	1.77E-02	6.29E+00	-7.08E+00	-4.78E-01	5.25E+00
1.91E-02	-4.62E-02	6.73E+00	-1.05E+01	-7.07E-01	5.25E+00
1.91E-02	4.62E-02	6.57E+00	-9.25E+00	-6.25E-01	5.25E+00
2.31E-02	-9.57E-03	6.52E+00	-8.84E+00	-5.97E-01	5.25E+00
2.31E-02	9.57E-03	6.68E+00	-1.01E+01	-6.83E-01	5.25E+00
2.31E-02	-4.24E-18	6.33E+00	-7.39E+00	-4.99E-01	5.25E+00
2.87E-02	-6.93E-02	6.78E+00	-1.09E+01	-7.34E-01	5.25E+00
2.87E-02	6.93E-02	6.16E+00	-6.15E+00	-4.15E-01	5.25E+00
3.54E-02	-3.54E-02	6.95E+00	-1.23E+01	-8.28E-01	5.25E+00
3.54E-02	3.54E-02	6.57E+00	-9.24E+00	-6.24E-01	5.25E+00
3.83E-02	-9.24E-02	4.89E+00	2.14E+00	1.45E-01	5.25E+00
3.83E-02	9.24E-02	5.74E+00	-3.16E+00	-2.13E-01	5.25E+00

x [m]	y [m]	u [m/s]	$p-p_0$ [Pa]	C_p	V_E
4.62E-02	-8.49E-18	6.91E+00	-1.20E+01	-8.07E-01	5.25E+00
4.62E-02	-1.91E-02	7.00E+00	-1.27E+01	-8.60E-01	5.25E+00
4.62E-02	1.91E-02	6.86E+00	-1.16E+01	-7.82E-01	5.25E+00
4.78E-02	-1.15E-01	2.24E+00	1.34E+01	9.02E-01	5.25E+00
4.78E-02	1.15E-01	3.78E+00	7.86E+00	5.31E-01	5.25E+00
5.30E-02	-5.30E-02	6.11E+00	-5.81E+00	-3.92E-01	5.25E+00
5.30E-02	5.30E-02	6.45E+00	-8.32E+00	-5.62E-01	5.25E+00
5.74E-02	-1.39E-01	6.27E-01	1.61E+01	1.09E+00	5.25E+00
5.74E-02	1.39E-01	1.48E+00	1.50E+01	1.01E+00	5.25E+00
6.70E-02	-1.62E-01	8.00E-02	1.63E+01	1.10E+00	5.25E+00
6.70E-02	1.62E-01	3.54E-01	1.63E+01	1.10E+00	5.25E+00
6.93E-02	-1.27E-17	6.86E+00	-1.15E+01	-7.80E-01	5.25E+00
6.93E-02	-2.87E-02	6.96E+00	-1.24E+01	-8.35E-01	5.25E+00
6.93E-02	2.87E-02	6.58E+00	-9.31E+00	-6.28E-01	5.25E+00
7.07E-02	-7.07E-02	4.18E+00	5.97E+00	4.03E-01	5.25E+00
7.07E-02	7.07E-02	5.11E+00	8.46E-01	5.71E-02	5.25E+00
8.84E-02	-8.84E-02	2.23E+00	1.34E+01	9.05E-01	5.25E+00
8.84E-02	8.84E-02	2.80E+00	1.17E+01	7.89E-01	5.25E+00
9.24E-02	-3.83E-02	5.57E+00	-2.02E+00	-1.36E-01	5.25E+00
9.24E-02	3.83E-02	6.40E+00	-7.93E+00	-5.35E-01	5.25E+00
9.24E-02	-1.70E-17	5.92E+00	-4.43E+00	-2.99E-01	5.25E+00
1.06E-01	-1.06E-01	6.37E-01	1.61E+01	1.09E+00	5.25E+00
1.06E-01	1.06E-01	8.85E-01	1.59E+01	1.07E+00	5.25E+00
1.15E-01	-4.78E-02	3.15E+00	1.05E+01	7.06E-01	5.25E+00
1.15E-01	4.78E-02	4.47E+00	4.51E+00	3.05E-01	5.25E+00